High resolution schemes for bluff – body aerodynamics

Cranfield UNIVERSITY

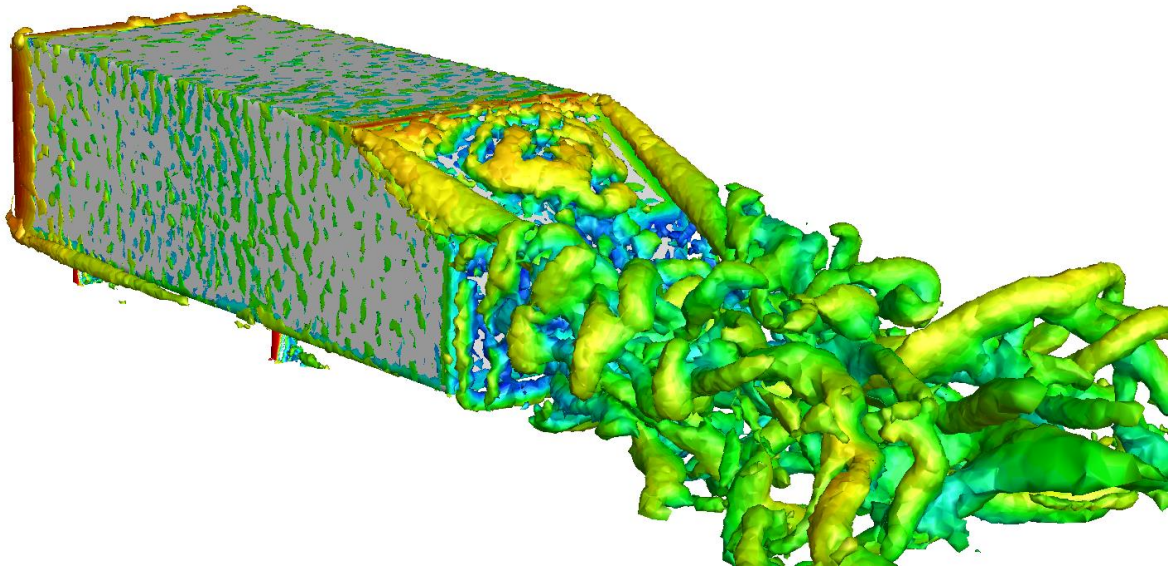

Dimitrios Nakos (s186587)

School of Engineering

Department of Engineering Physics

Date : 01 / 10 / 2013

This page is intentionally left blank

ACKNOWLEDGEMENTS

I would like to thank my supervisor Professor Dimitris Drikakis for all the motivation he offered to me in order to venture into this MSc degree and for sparking my interest for the science of Computational Fluid Dynamics in the first place.

I would also like to thank and express my gratitude to Dr. Panagiotis Tsoutsanis for all the valuable knowledge, enlightenment and help he offered to me throughout this MSc, which are most appreciated.

Furthermore, it is my wish to wholeheartedly thank Dr. Laszlo Konozsy for providing me with very valuable CFD and personal knowledge and help, whenever I needed it, without taking time or effort into account, in order to do so.

It is my wish to thank Dr. Antonios Antoniadis for all the help and valuable advice during the grids construction, as well as Dr. Irene Moulitsas for her support from the time I started, to my viva examination.

I am very grateful towards my parents for all their financial and personal support as without it, none of this would have become reality, as well as my brother and best friend George Nakos, along with my close friends Panagiotis Krontiras and Marios Fotopoulos.

Table of contents

Abstract

This MSc by Research study has been conducted with the application of a variety of grid configurations for extensive grid analysis along with various numerical schemes on the Ahmed body benchmark test case, in both 2D and 3D analysis.

A number of different numerical schemes were used in conjunction with the Reynolds Averaged Navier – Stokes (RANS) equations for steady state simulations, by implementing the Spalart – Allmaras turbulence model as a closure to the equations.

The efficiency of the aforementioned grid – numerical schemes compilation in terms of achieving physically meaningful results is assessed in both commercial, widely – used solvers (FLUENT) and the Cranfield University in – house developed UCNS3D code, ultimately aiming to capture and exhibit the differences in the implementation of similar configurations in different solvers for high resolution methods.

The simulation results are analysed further and an extensive conclusion analysis takes place for all the cases examined, with the combination of numerical methods and grid configurations used.

It should be pointed here that the purpose of this study is to capture and study the main aspects of the flow in 2D and 3D dimension simulations, as well as the assessment of a compilation of numerical schemes never applied and studied before in the Ahmed body case, in an effort for further insight and physically meaningful results in the case. The aim of this study is not to provide results for effective implementation of the turbulence modelling in the Ahmed body test case.

Chapter 1 : Introduction

1.1 The Existence and Importance of CFD in Engineering Applications

Flow around bluff bodies is of great importance today not only in automotive industry, but in every industrial department or product that is associated with any kind of flow around an object, posing one of the greatest factors to take into consideration in terms of designing a new car, aeroplane, ship, etc. A strong background and knowledge in aerodynamics and the physical mechanisms governing their basic principles and phenomena is essential in order to achieve improvement of the flow through various means. More specifically, in the case of automotive engineering an analysis and results were presented mostly by gaining experimental data on various automotive shapes. However, setting up an experimental process is rigorous and time – consuming, especially when the setup has to be altered to achieve the desirable results. Computational Fluid Dynamics (or commonly abbreviated as "CFD") are used to model flow around an object through computer simulations and are considered to be a significant tool in flow structure studies as means to complement experimental findings. It is obvious, that due to the ease of use of commercial or various inhouse solvers to perform CFD analysis and in addition to the ever – growing powerful computer resources existing nowadays, CFD can be applied successfully to almost every industrial application, saving the developers time from repetitive and time – consuming experiments to validate their methods and improve their test objects.

Despite the aforementioned, there is a great level of complexity in automotive design, and detailed solution and validation tasks are almost impossible and non – affordable (both in terms of money and computational cost), mostly due to this sort of complexity, that derives from a vast combination of accessories in an automobile geometry. As a result of the aforementioned restrictions and due to the implementation of the averaged Navier – Stokes equations (RANS), this study will produce solutions based on particular assumptions made for the physical quantities and phenomena involved, bearing the restrictions of a steady – state simulation and ultimately, this will possibly result in producing unrealistic results. Taking this into account, validation methods for various aerodynamic flow features (such as drag, lift, turbulence, wake, etc.) are using simpler geometries of the object in question, that resemble the real ones in terms of these features, as benchmark tests for measurements and validation of CFD methods. A widely known benchmark test for automotive flows and experimentally valid to resemble flow properties that resemble those of automobiles, is the Ahmed body test case.

1.2 Aim

The aim of this thesis is to provide more insight into the complicated flow patterns and explain the physical properties associated with the flow around the Ahmed body configuration. The behaviour the flow structures exhibit around this benchmark test, alongside various parameters that affect the physical phenomena governing the flow around the Ahmed body in different flow conditions, will be examined, as well.

1.3 Objectives

The objectives of this Research Thesis are the following

- Presentation of the physical phenomena affecting flow and challenges in terms of simulating the flow around the Ahmed body and how these phenomena are connected to real life automobile applications.
- The generation of unstructured 3D and 2D grids for the Ahmed body configuration.
- Simulation of different flow conditions around the Ahmed body for the 2D and 3D grids.
- Validation of the simulation results in comparison to the experimental results presented so far.
- Comparison of different numerical schemes in terms of computational efficiency, accuracy and robustness.
- Presentation of the issues and remaining open challenges for resolving the flow patterns associated with the correct Ahmed body configuration.

Chapter 2 : The Ahmed Body

2.1 The Ahmed Body

In order to examine flow separation and wake structure around typical geometries of automobiles, Ahmed et al [2], [3] conducted studies in wind tunnels in quarter scale automobile models and focused in the visualization of flow in the wake region on time averaged structure. He also introduced what is now known as the "Ahmed body" geometry. A "generic" geometry consisting of three parts; a rounded-up front part, followed by a rectangular box shape and a slant plane in the downstream, where the rear end of the body is.

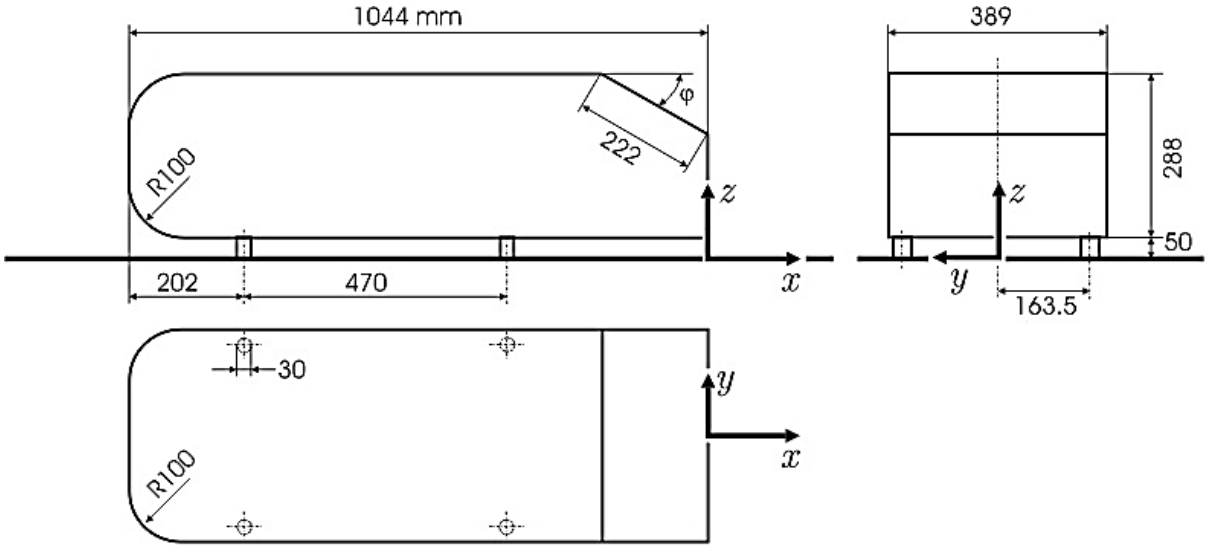

Fig. 1: The original Ahmed body. Side view and upper view for the standard 30^o slant angle as presented by Ahmed S.R. and Ramm G. [2]

The original dimensions of the geometry introduced by Ahmed S.R. and Ramm G. [2], are the ones seen in Fig. 1. The basic characteristics of the geometry which may affect the flow around it, are clear in first sight, however, an extensive analysis to their virtues and phenomena exhibited, follows.

The rear slant plane is moveable in order to move in different slant angles for studying flow separation in different angles. The front and the rear part are connected to each other with the rectangular shaped box. The shape of the Ahmed body offers comparatively easy flow simulation environment, but also maintains the great advantage of being a very good scaled replica for exhibiting the aerodynamic features of basic automobile bodies, by having almost the same flow structures.

A very good example of pattern of the flow structures taking place in the slant angle of the bluff body, as presented in the study of Vino et al. [52], is presented in Fig. 2. This study was conducted on the basic rear slant angle of the Ahmed body (30^o), for a Reynolds number of Re = $4.4x10^5$. The pattern is similar for angles between 15^o – 30^o. Longitudinal vortices, recirculation bubble and recirculation torus are apparent:

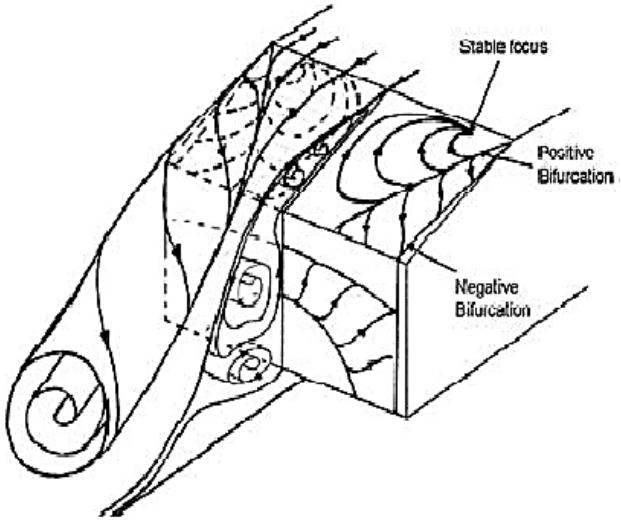

Fig. 2 : Rear view sketch of the Ahmed body with the flow structures expected for an angle of $15^o \leq \vartheta \leq 30^o$ (Vino et al. [52])

Studies and experiments on this geometry as in [52] for measurements of pressure, force and wake effect surveys on a combination of different slant angles, it was evident that pressure drag was responsible for a percentage of about 85% of the total aerodynamic resistance, with most of this drag manifestating itself in the rear end of the body. Drag force mostly owes its existence to wake flow behind the Ahmed body, so precision in modeling and predicting the flow separation and wake flow is essential in any sort of simulation for this case.

An example of the streamlines exhibited in the near wake region of the slant angle, for a Reynolds number of Re = 768.000, as observed by the rear view and as presented by Minguez et al. [51] is Fig. 4. A flow separation at the edges between the lateral and the slant edges of the body, is apparent.

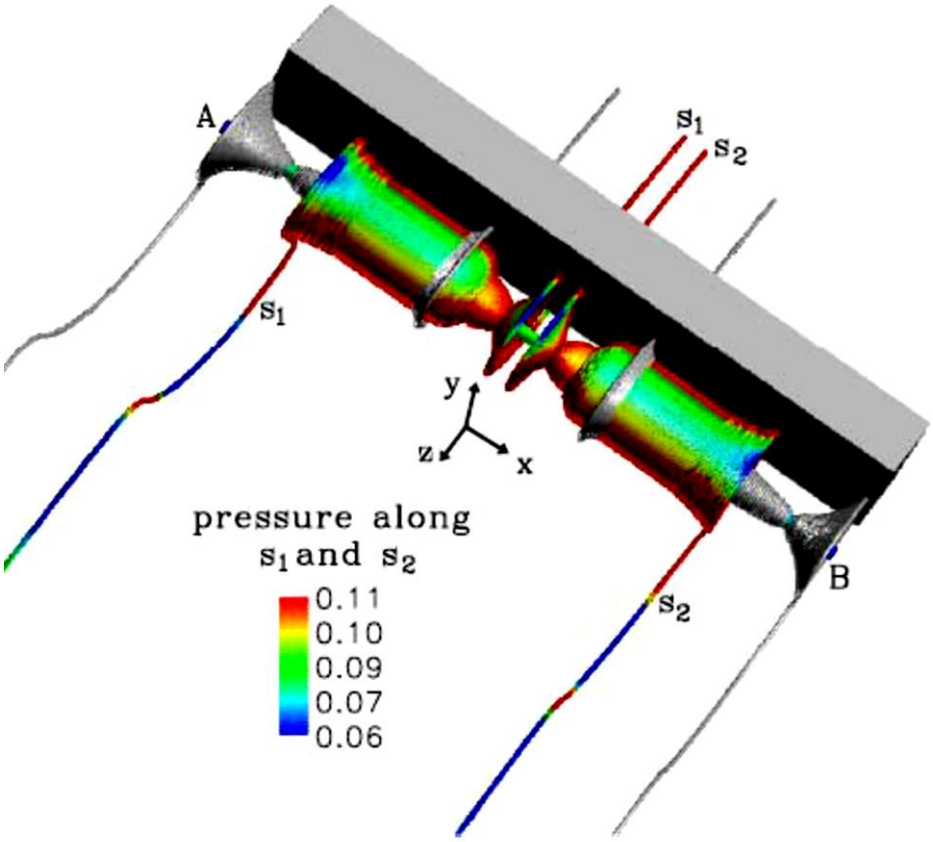

Fig. 3: Typical illustration of bifurcation in the wake of a bluff body according to the work of Sau and Hwang [91]

An interesting feature exhibited in the wake of various bluff bodies is the phenomenon called bifurcation, which is responsible for the vortices exhibited in the near – wake and wake regions. Bifurcation mostly occurs with changes in the parameter values of a system, resulting to instant topological or qualitative changes in the system's behavior. According to the work of Sau and Hwang [91], bifurcation in the wake of bluff bodies is triggered by spanwise pressure oscillations, a rise in the maximum (local) values of pressure over the extended vortex corelines, combined with a gradually decreasing pressure on the length of their two sides [91]. Drag is affected by the vortices in the wake region by the creation of an induced downwash. This is the source of the induced drag. The induced drag effect becomes greater as the strength and size of the vortices raise, consequently resulting in a greater downwash component on the airflow over the slant angle, which is the reason why the drag of the bluff body is affected by the vortices in the wake. Another very good example of a case study for bluff body aerodynamics, is the renowned Cooper model [92], [93], however further analysis this will not be conducted in this study as the Ahmed body will be examined, which offers an easy simulation environment and resembles in a more realistic way the physical phenomena occurring in modern automobile shapes.

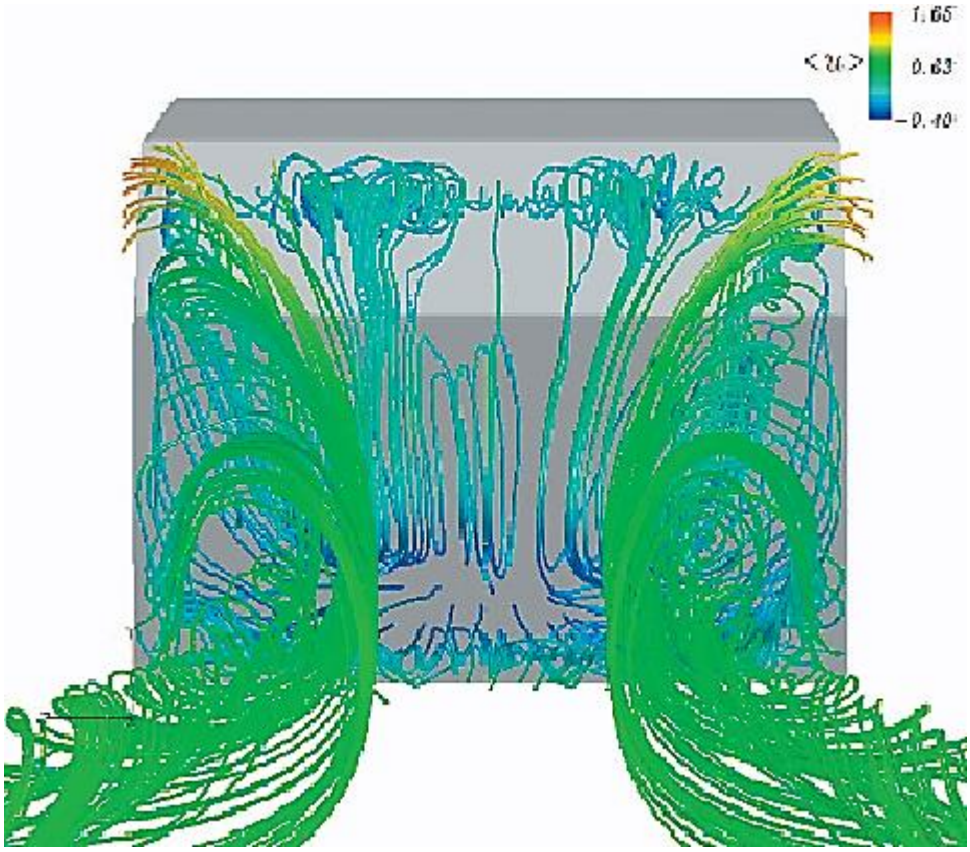

Fig. 4 : Mean three dimensional streamlines pictured in the wake as presented in the work of Minguez et al. [51]. The streamlines are colored by <u> (mean streamwise velocity).

However, there is an apparent trend for the recirculation bubble to increase its size in the rear slant region, should the drag and lift forces be reduced rapidly [4]. It is though, extremely important in order for the drag force to be calculated accurately, to understand the separation of the flow, simulate the flow separation, the wake flow and the dimension of the separation zone [5].

Various features define the flow around the Ahmed body and the complex flow observed is a product of these features, which are: vortical structures (on each side) longitudinal to the shape of the body, the appearance of a separation bubble on the rear window (3D) and a rear-base located 3D wake.

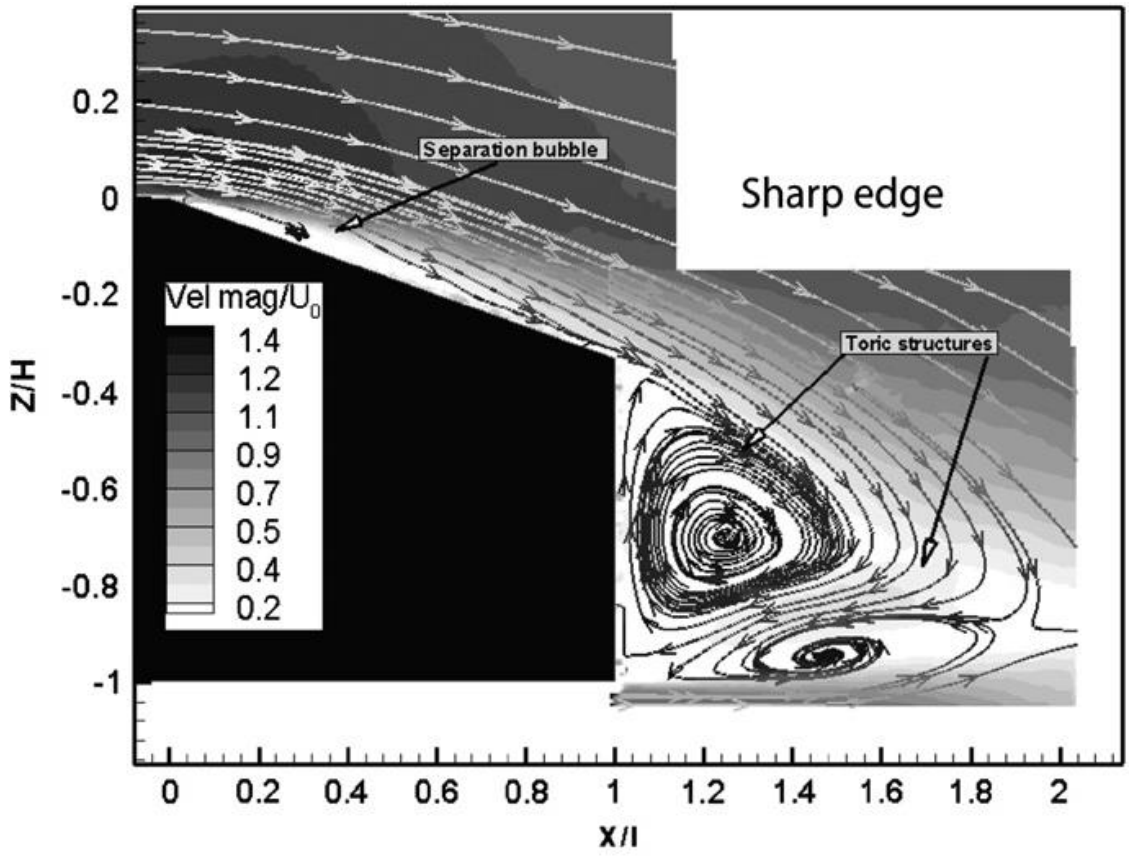

Fig. 5 : Mean velocity magnitude fields in the vertical plane at the rear base and the rear window of the Ahmed body for a sharp edged subcritical rear slant edge configuration of 25^o (Thacker et al. [6]).

The work of Thacker et al. [6], in Fig. 5, for a Reynolds number of Re = 2.2×10^6 is exhibiting this separation bubble, as well as the vorticity structures in the wake.

These features are the most important ones to be examined in a flow study around the Ahmed body. For a slant angle of 25^o, the Ahmed body resembles the aerodynamical properties of a hatchback shaped automobile, one of the hardest to model flow in, because there is a combination of all the three aforementioned features.

Their quantitative contribution to the drag balance, is 12% for the first feature (longitudinal vortical structures), 34% for the second (3D separation bubble) with the biggest percentage of 44% belonging to the rear base 3D wake. The rest 10% is divided among other features, such as forebody contribution, viscous drag [7]. In the case one of these percentages is altered (reduced or suppressed) the rest of them will be altered as well and the drag under flow control will be based in different quantities of each of the remaining features [8].

According to Joslin [9] there is a big difference between understanding and controlling of the flow in an airplane or an airfoil and a road vehicle, as there are some factors such as complex geometries and wheels that affect the flow separation, which ultimately tend to provide a highly unstable 3D flow [10]. The dynamic behavior of the vortex wake released from the Ahmed body in conjuction with these unstable interactions created through flow separation, are mostly what the aerodynamic forces

on road vehicles are comprised of [11]. The resemblance to the effects appearing in vehicles, also applies to the total pressure drag and the main drag values obtained in conjunction with the alteration of the slant angle. Figure 6, exhibits the latter properties, for a slant angle of 12.5^{o} and a Reynolds number of Re = 4.25x10^{6}, according to Franck and D'Elia, in comparison to the experimental data:

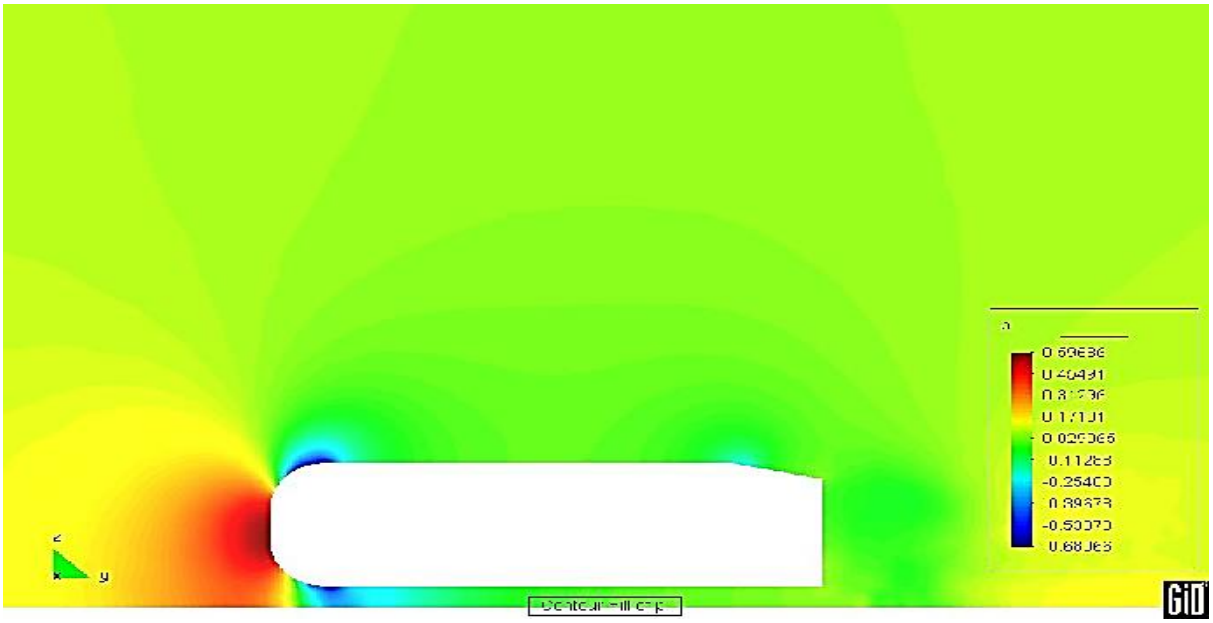

Fig. 6 : Contour fill field pressure on the Ahmed body for a slant angle of *12.5^{o}* Franck & D'Elia [11]

The pattern of the vortices created in the side edge of rear slant angle, as observed in the isosurfaces of Fig. 7 [51], showing the velocity field on the slant and its wake:

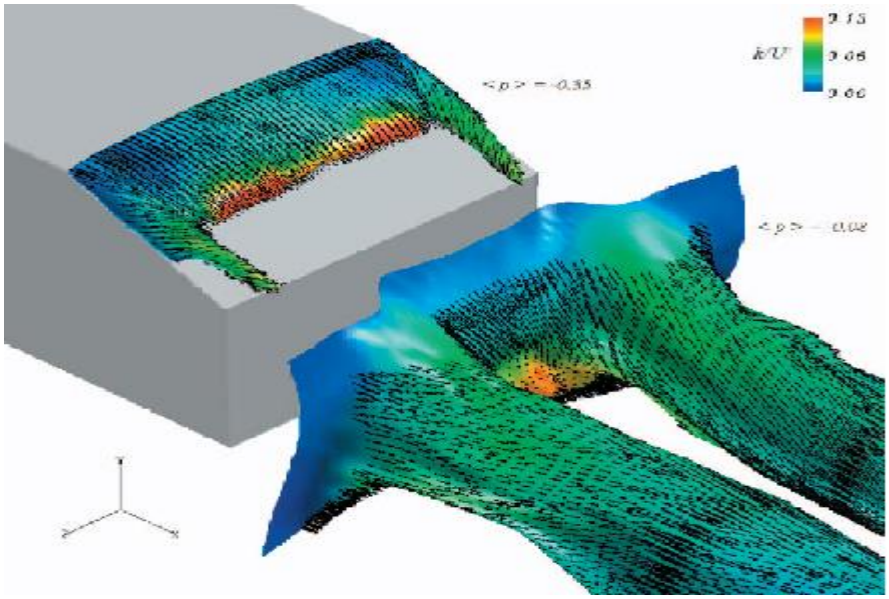

Fig. 7 : Isosurfaces of the mean pressure field, colored by the dimensionless kinetic energy (*k*). Exhibition of velocity field on slant angle and wake, according to Minguez et al. [51]

There has been a considerable amount of techniques which might be applied in order to control flow separation, but they all depend on how the test subject is configured and what the desirable outcome is. For example, in the Ahmed body, such as in the case of backward facing step, defining exactly where the location of the flow separation part is [12] controlling the shear layer on the separation [13], [14], [15] is a mean of controlling flow separation. In the case of a non-geometrically imposed flow separation, such as in a smoothly contoured ramp [16], techniques involve control of the boundary layer upstream of the separation [17], something that will ultimately alter both the properties of the shear layer and the location of the separation.

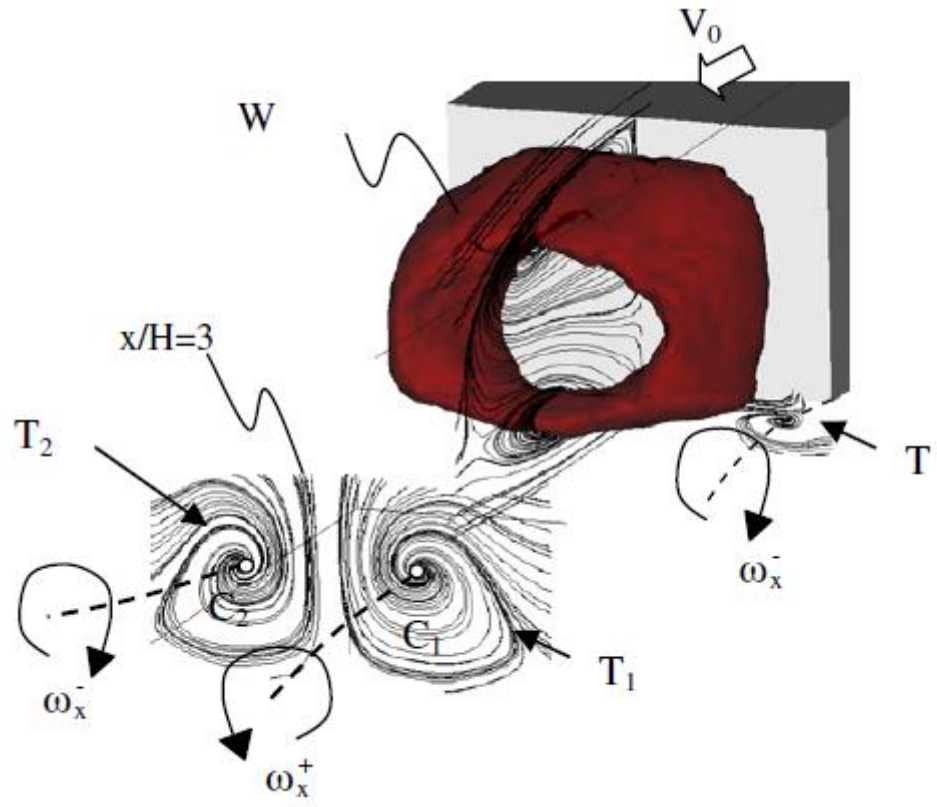

Fig. 8 : Topology of the flow in the near – wake for a simplified bluff body (Roumeas et al. [18])

In order to control flow, Roumeas et al. [18] proposed the use of actuation along the wall downstream the separation, in a simplified body, in order to achieve control of flow. The movement would be provided by blowing or suction, or both in the same time, however there might be a better energy balance in its upstream counterpart. The topology of the flow near the wake, was the one depicted in Fig. 8.

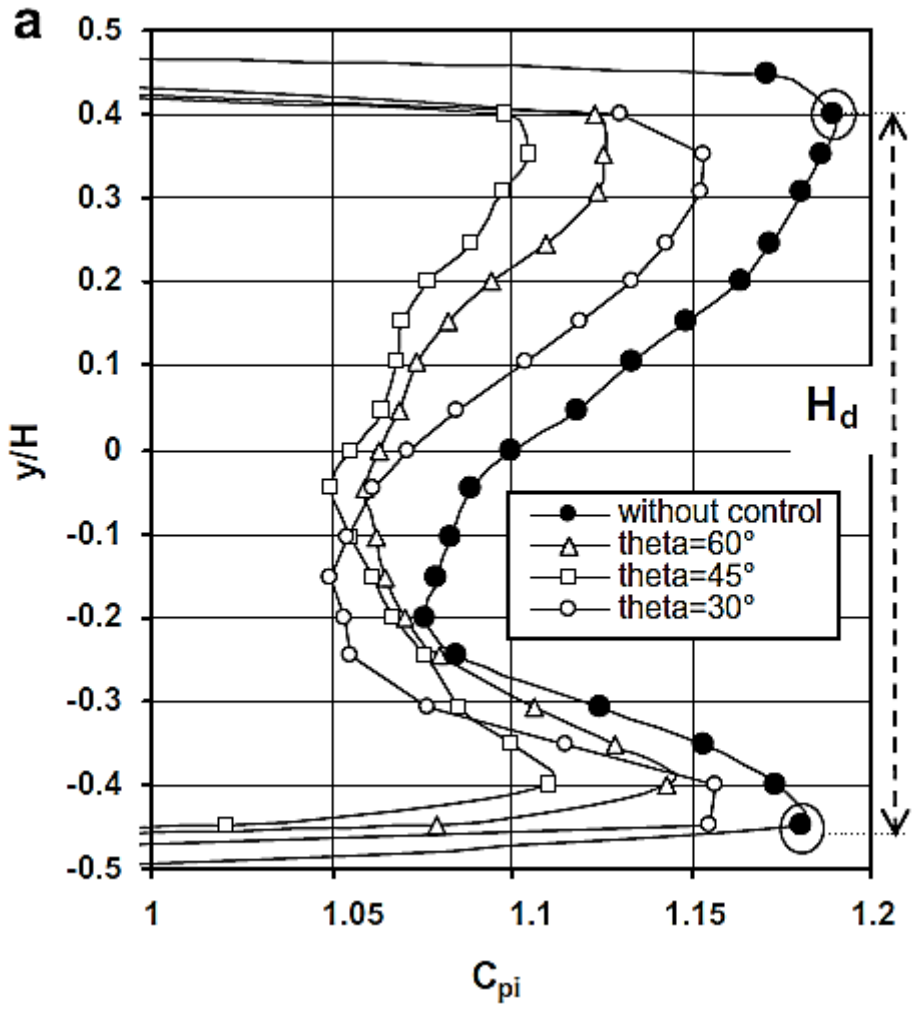

Fig 9 : Total pressure loss coefficient profile for a vertical profile measured in the longitudinal media plan (for *x/H = 0.5*) according to Roumeas et al. [18]

The topology of the flow, however, exhibited two peaks in the total pressure loss coefficient, both without any sort of control and in different blowing angles (30^o, 45^o, 60^o) and the streamlines deviation near the separation line is associated with the transversal wake section reduction, as seen in Fig. 9.

Experiments [19], [20] have shown that it is possible to modify the near wake of a d diameter cylinder by decreasing its size (approximately at d/10) by virtue of flow control in the volume downstream the flow separation using actuation. A theoretical approach [21], also proves the possibility of the venture.

Ahmed conducted some experiments [22] in an effort to prove, that the shape of an automobile is inextricably linked with the amount of drag and the wake structures presented behind it, using a basic quarter scale car model with three different rear – ends, which resembled the flow properties of three of the most common automobile shapes. The configuration used can be seen in Fig. 10:

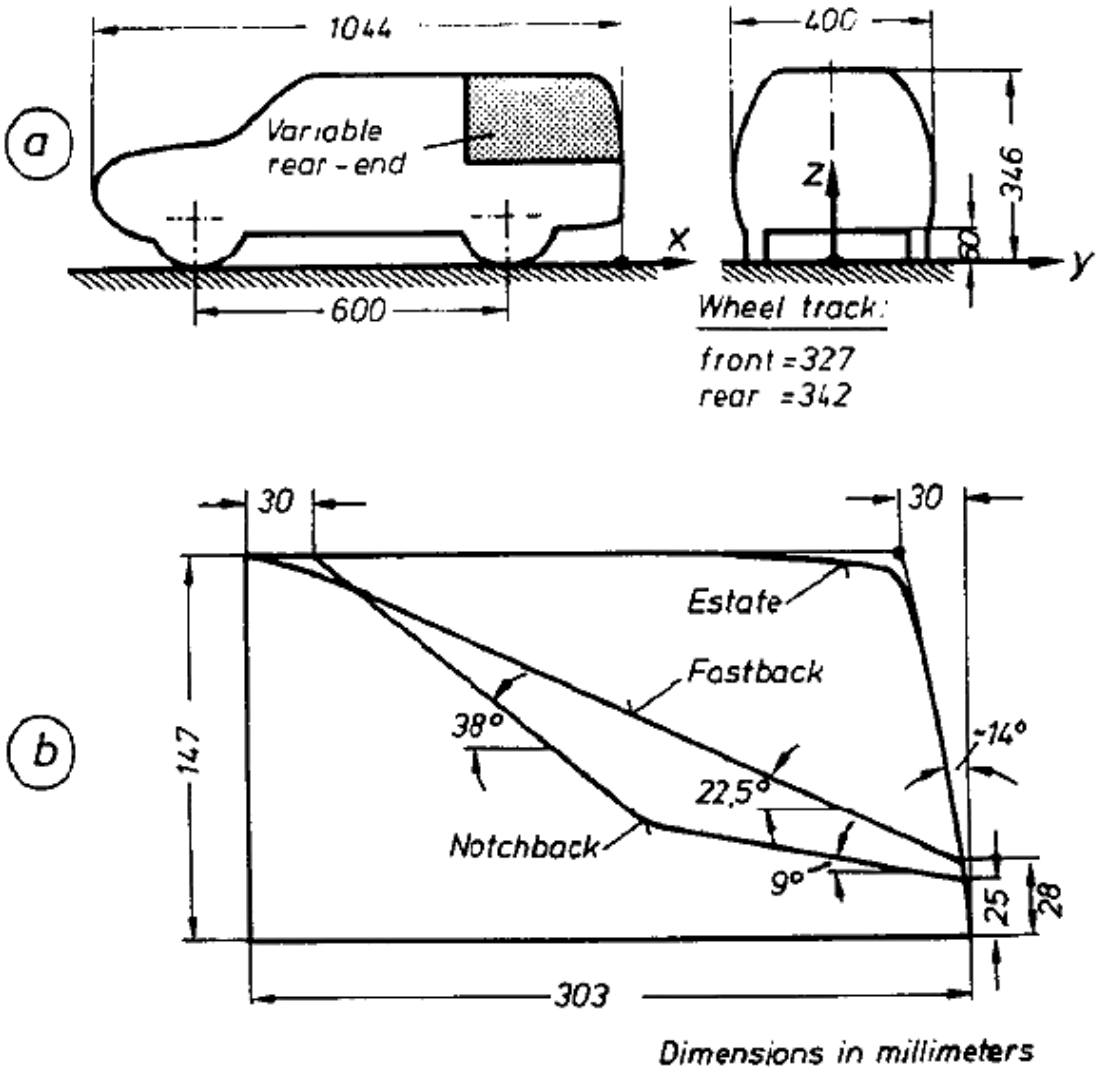

Fig 10 : (a) Basic model used by Ahmed [22] to resemble flow proeprties in automobiles and (b) The interchangeable ends he used for the different automobile shapes

Among other conclusions, was the forming of two recirculation areas at the back of the bodies. He observed that recirculation in the upper region has a motion in the sense of down to the ground and up along the vehicle base, while the lower region presents the opposite behavior. The behavior and size of these flow features is mostly associated with the type of the car body the model resembles (fastback, notchback and estate) as they all present different properties in the upper and lower recirculation region of the separation bubble plane manifestating. Contra-rotating longitudinal vortices are formed for each tip of the slant plane and are again exhibiting differences in the wake according to the type of the model. Differences were observed in the vertical flow, as well as the high-energy inner regions, for every car geometry.

More specifically, he observed:

- Notchback model (Fig. 12): The upper and lower recirculating regions of the flow in the separation bubble plane were of equal size. After the flow reattached (separation bubble closed) the longitudinal vortices caused the wake of the model to present a downwash. The model's wake contains a high energy inner region.

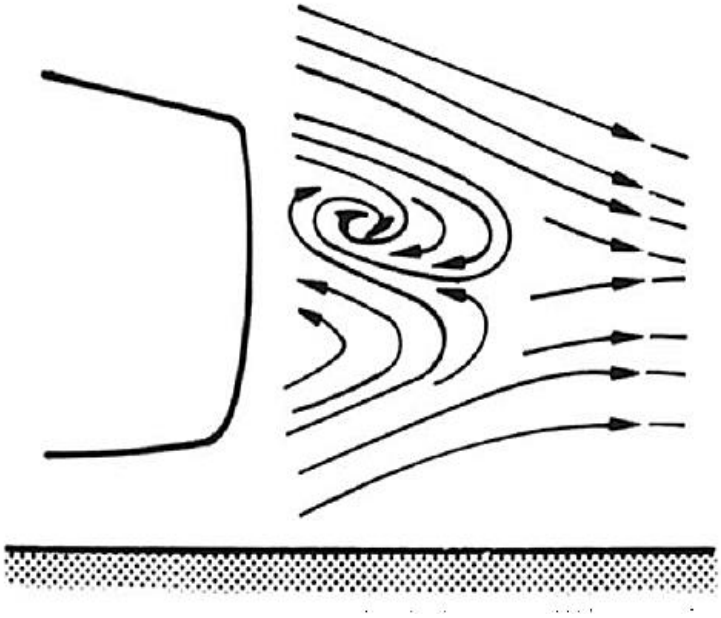

Fig. 12 : Streamline pattern in the near – wake of the notchback model (Ahmed, S.R. [22])

- Fastback model: Contrary to the notchback model, the lower recirculating region of the flow in the separation bubble, prevails, but in the flow reattachment, a downwash is presented as well. The longitudinal vortices in the wake, appear to be very strong and slowly dissipating downstream. In accordance to the notchback model properties, its wake contains a high energy region, as well. The streamline pattern of the Fastback model can be seen in Fig. 13 (left). Differences in the streamlines between fastback and notchback models are significant.

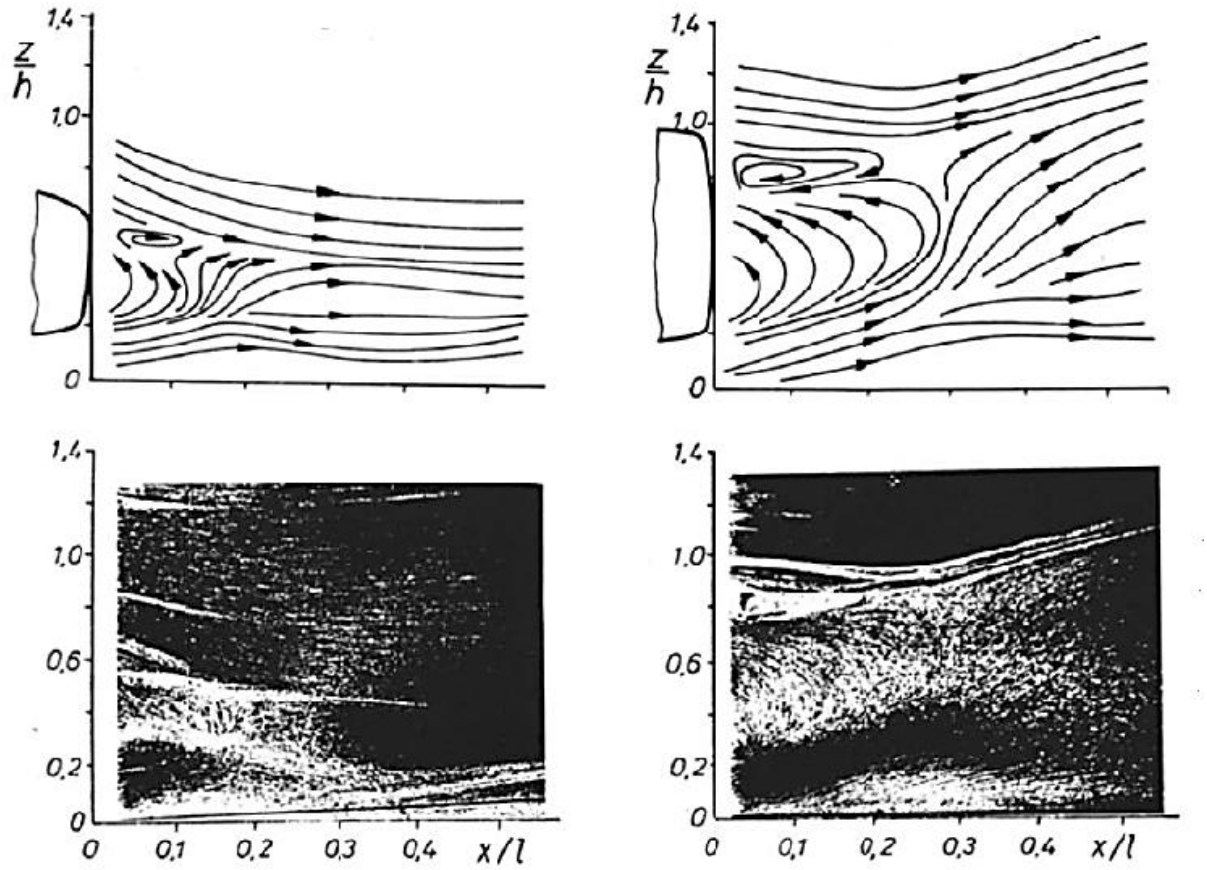

Figure 13 : Streamline patterns in the near – wake of the fastback model (left) and the estate model (right) as observed by Ahmed [22]

- Estate model: In line with the fastback model, there is a prevailing lower recirculating region of the flow in the separation bubble but despite that, an upwash can be observed in the closure of the separation bubble. Due to the nature of the motion induced in the lateral vortices, they present a tendency to reach the free flow region and decay faster. Again, the three models are exhibiting a great difference to how their streamlines are formed. In comparison to their total aerodynamic drag, the measured values for vortex drag were ~28% and ~8% for the fastback and estate models, respectively.

Simulations have been performed to measure the corresponding figures for drag coefficients in the near wake region of the Ahmed reference model for two different flow configurations of the same slant angle (25^{o}), one model consisting of the typical Ahmed reference model sharp edge connection between the roof and the rear slant studying flow separation and the other having a rounded edge in an effort to suppress flow separation and consequently drag, studying flow without separation, as seen in Fig. 15 [23].

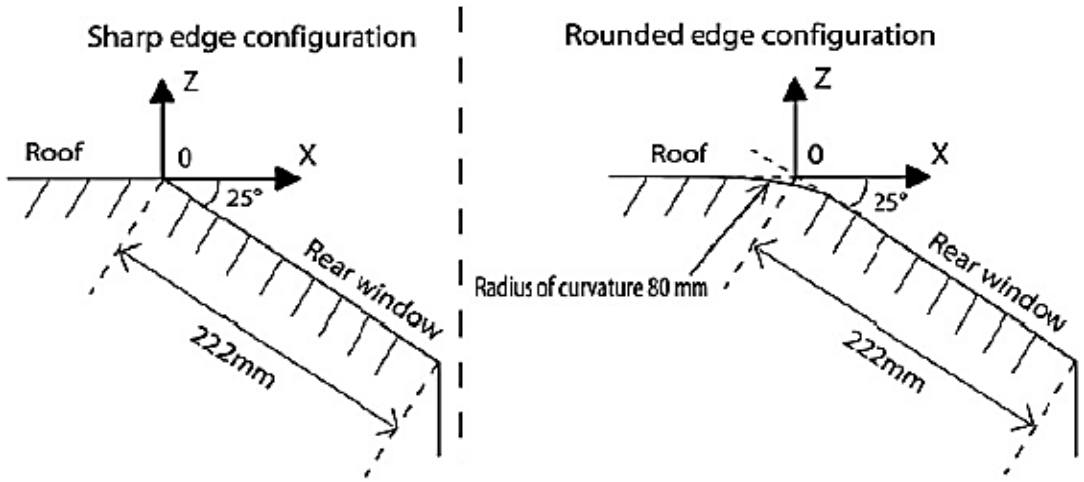

Fig. 15 : The two configurations of the 25^o slant angle used by Thacker et al. [23] to between the roof and the rear window in the Ahmed body

Results showed, that for an increasing Reynolds number of in the rounded rear edge model, without changing the lift components of the aerodynamic loads, the drag coefficient decreases, reaching a value of around 10% less than the original 25^o Ahmed body model and there was an overestimation of the drag coefficient by 30% when compared with the literature values, as seen in Fig. 16.

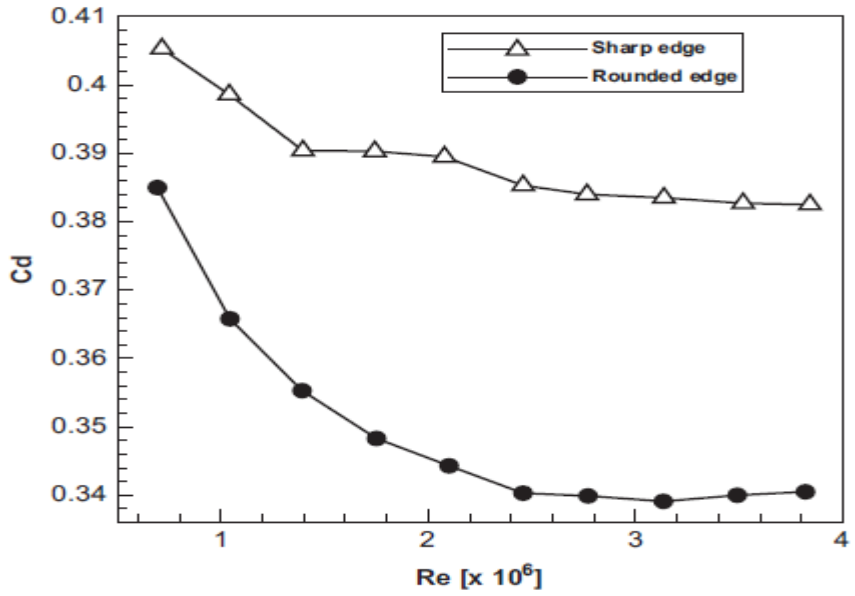

Fig. 16 : Sharp and rounded edge configurations of the 25^o slant angle Ahmed body. Drag coefficient – Reynolds number increase chart (Thacker et al. [23])

Higher static pressure was observed in the central part of the rear window without flow separation, but was relatively insignificant comparatively to global lift and the pressure drag contribution in the window. The smaller drag levels observed in

the rounded edge model, are mostly due to developed interactions between the rear window and the rear wake flow, having as a result the relocation of the vertical center of the wake toric vortices, connected with a core consisting of low pressure. However, despite the reduced vortical center intensity, not many changes were observed in connection to global vorticity distribution and longitudinal vortices do not seem to be immensely affected by the lack of flow separation on the rear window and in addition to that, the value of lift forces did not exhibit any significant change, as for Reynolds numbers above Re = $1x10^6$, the highest increase value observed was only 1.5%. In terms of fuel economy, drag forces are one of the main factors that should be taken into account, upon characterization of aerodynamic features in vehicles [24].

Inter – vehicle connections in trailing vehicles is of extreme importance to aerodynamical measurements and sizes, especially in the body of the trailing vehicle. Schlichting proved that flow separation may be radically affected even with the slightest change in the shape of a body, especially if this change affects pressure distribution, as well [25]. The usual drag coefficient of a typical car body ranges somewhere in the region of 0.3 – 0.4 and form drag is responsible for almost the whole of aerodynamic drag [26]. The use of a leading upstream body in order to reduce the drag of a trailing one, has often been proposed, as there is a significant connection between an upstream body that will experience higher forebody drag and matching its wake size in order to act as a deflector for the downstream bluff body and ultimately, reduce the trailing body's drag and therefore affect the trailing body's velocity, depending on the distance between them, as seen in Fig. 17, 18, 19 [27], [38].

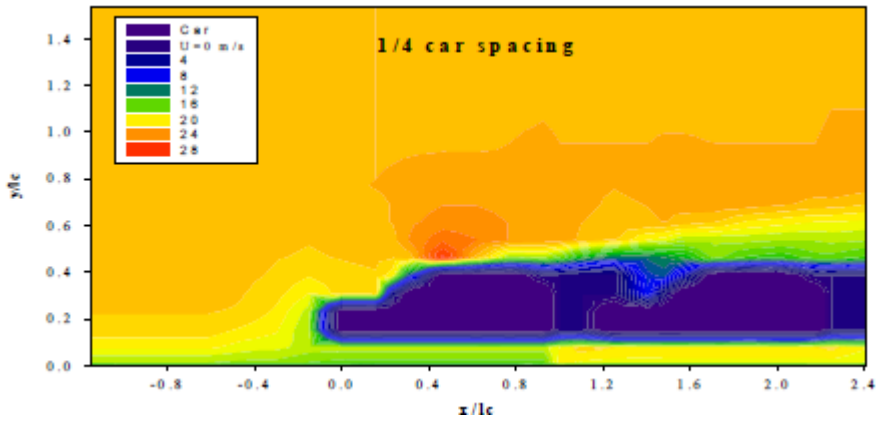

Fig. 17 : Contour plots of velocity for two consequent automobile shaped bluff bodies and ¼ car spacing between them as simulated by Roshko & Koenig [27]

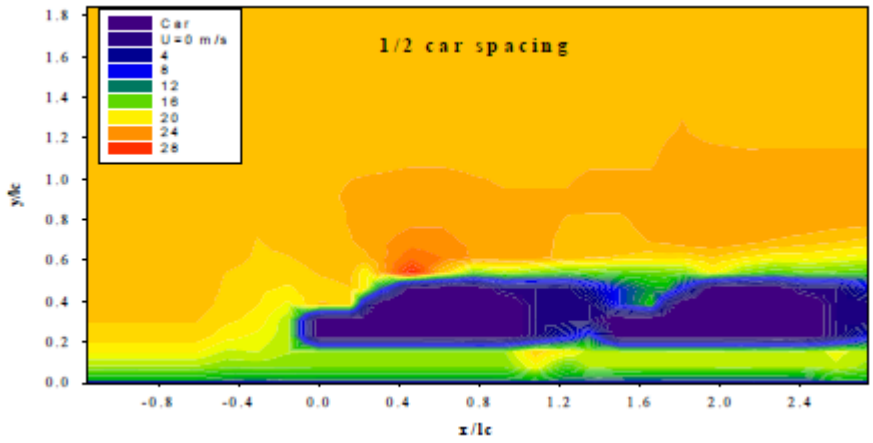

Fig. 18 : Contour plots of velocity for two consequent automobile shaped bluff bodies and 1/2 car spacing between them (Roshko & Koenig [27])

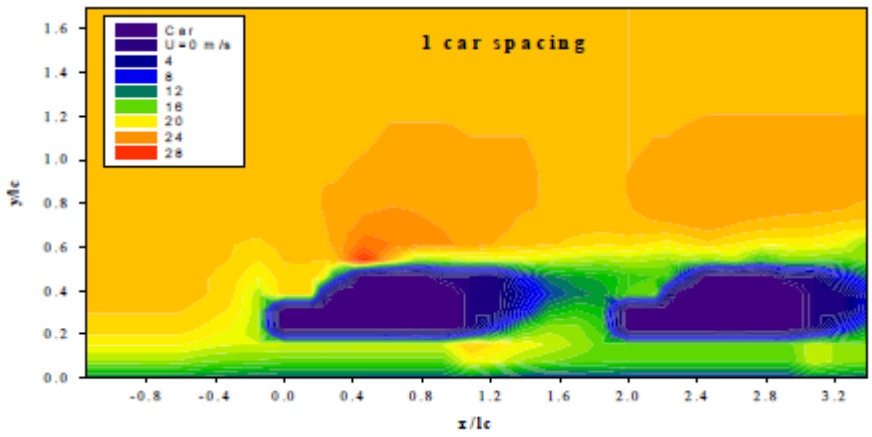

Fig. 19 : Contour plots of velocity for two consequent automobile shaped bluff bodies and 1 car spacing between them (Roshko & Koenig [27])

The same principle applies in other commercial applications as well, such as trains, where except for the rear end of the train, base pressure is raised with the leading carriage (upstream) shielding the downstream ones [28]. In every inter – vehicle spacing study, simulation or experiment, it is of great importance to define a number of variables that have an immediate effect in the perspective under which the examination of the problem will be performed. Some of these are the geometry of the body (cars – with all the aforementioned geometries such as fastback etc , bus, train, truck), the in between the bodies positioning (lateral, longitudinal), the relative to each other spacing which defines many of the properties of the flow and in the case a more realistic approach is attempted, it is definite that atmospheric wind will have to be taken into consideration (relative direction and nature).

A very good way to reduce air drag and minimize fuel consumption when it comes to vehicle platoons, is by reduced mean velocities, something that is achieved by drafting (following closely a vehicle inside its wake region). The basic idea behind drafting, is for the trailing body to take advantage of the leading body slipstream by maintaining a close spacing behind it for reducing its drag, however, there is a highly unsteady turbulent flow observed in the wake region of such slipstreams. In connection with the variables connected with drafting and ultimately affect drag, the ideal spacing between two bodies might vary when it comes to different geometries and effect raise drag on the trailing body if their spacing is not optimal. For example, when the upstream body is a bus followed by a geometry that resembles that of a hatchback passenger car (drafting), the ideal distance between them in terms of fuel efficiency and drag reduction is about 4 meters. Any other distance will either increase the drag coefficient or will not be safe for the passengers of the vehicles, as Fig. 20 and Fig. 21 exhibit [29].

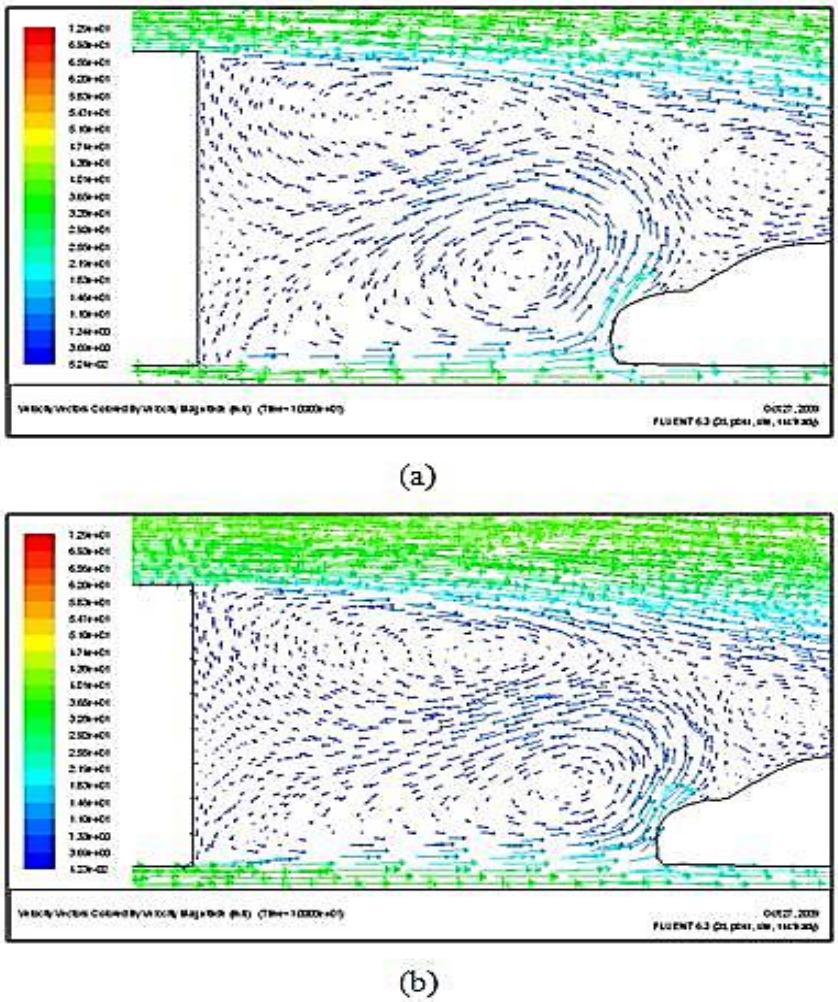

Fig. 20 : Velocity vectors of the wake for a drafting position of an intervehicle spacing between a car and a bus of (a) *4.0 m* and (b) *5.0 m* (Amirnodir et al. [29])

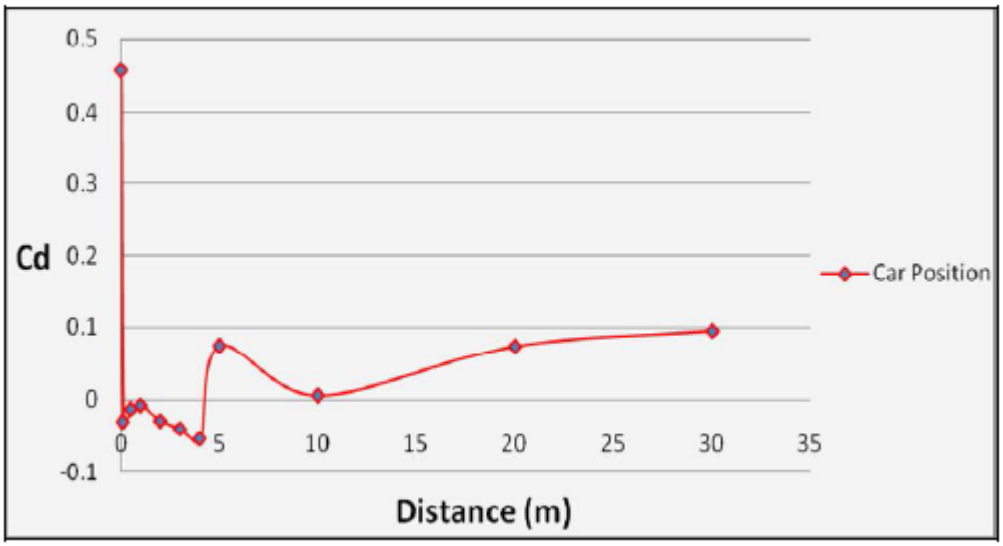

Fig. 21 : Drag Coefficient (Cd) value for an intervehicle spacing of *0 – 30 m* according to Amirnodir et al. [29]

Following the previous example, due to their close coupling, trains have a low drag per unit volume, so it can be observed that close couplings (or spacings) result in low drag coefficients. In the case of trucks (closely located parallelepipeds which resemble their basic aerodynamical properties) and close spacings, studies have shown that a drag reduce ranging from 10 – 40% has been achieved, thus suggesting that travelling in convoys might lead to reduced drag coefficients and ultimately, reduce of fuel consumption [30]. There is a wide variety of simple geometries easy to change shape while in the same time resemble various vehicle geometries and their critical flow features and as is the parallelepipeds with the trucks example, so is the Ahmed body for automobile applications [31]. The slant angle of 30^{o} provides similar flow properties with the ones of a typical modern passenger car which are a vortex shaped like a “horseshoe” due to the growth of the separated bubble region from roof and the drag coefficient is lower than the lift coefficient, owing to the nature of the longitudinal vortices.

As in the bus example though, the work of Watkins, Vino [32] has also proved that drag reduction through the drafting technique for two similar geometries (two consecutive Ahmed body geometries), combined with close spacing, might raise the value of drag in the trailing vehicle, as a result of influence imposed by the rear vortices, as well as exhibiting changes in lift. In their experimental arrangement inside a wind tunnel with a freestream velocity of 35 m/s which corresponded to a Reynolds number of $2.3x10^{6}$, having a freestream turbulence intensity of 1.8%, found the lift and drag coefficients to be in accordance with the experimental data.

This work proved that lift and drag coefficients might be reduced or raised, depending on the spacing in trailing vehicles of similar geometries. As observed in Fig. 22 for certain distances, a raise on the values of the aforementioned parameters was

noticed, with the value of drag coefficient even reaching a 30% class raise, for a spacing distance smaller than 1m, whereas this value was decreased, as spacing distance was raising.

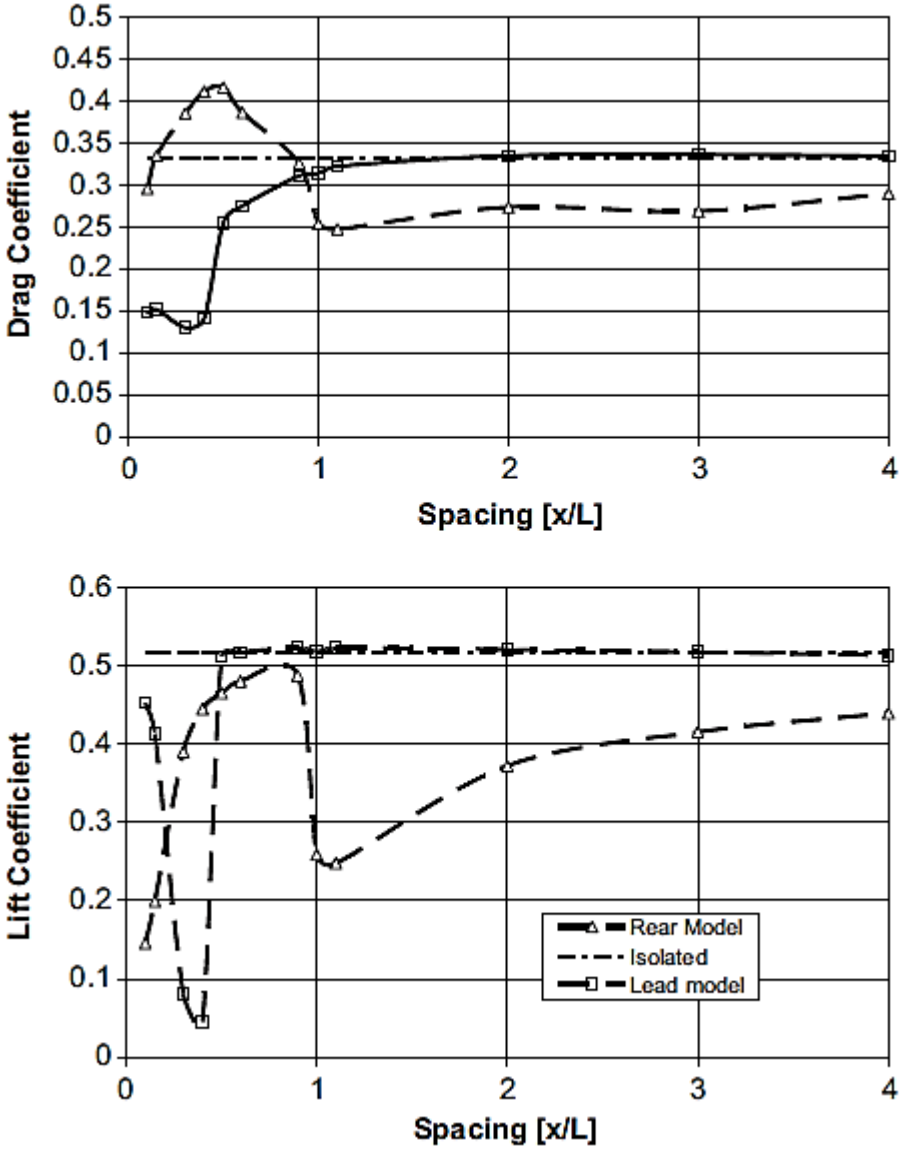

Fig. 22 : Lift and drag coefficients for different spacing dimensions in two consecutive Ahmed body geometries (Watkins & Vino [32])

Significant reductions to the drag of the lead vehicle were observed, when in close spacing with the trailing one. A large variation was exhibited in the values of the lift coefficient, for a 1m. spacing (between 0.1 – 1 m.).

The above experimental process, forced the authors to ultimately conclude with raising questions about drafting in consecutive bodies with different slant angles and different spacings, explaining that the interaction effects taking place, should be further researched.

2.2 Previous Studies

There have been various previous studies on the Ahmed body model, exhibiting quite a variation in terms of flow conditions around this benchmark model. There is an extensive record of either experimental or computational data enabling a wide variety of parameters in need of examination, as their overall existence and altering, tend to affect flow topology and flow patterns exhibited in the Ahmed body model. These previous studies will be presented in the forthcoming chapters and sub – chapters through analysis of some physical properties and how their physical meaning and alteration affects flow around the Ahmed body.

2.3 Reynolds Number

Reynolds number is one of the main factors that should be taken into consideration, for every sort of flow and varies, depending on the case and the conclusions one would like to reach in every case and they are connected to the simulation model being used. One of the main factors by which the corresponding Reynolds number is defined in various occasions, is according to the model length. There are many cases examined in different Re numbers such as the effects of air flow in the wake of a large vehicle on trailing a passenger car in a two – dimensional car model, with a Re = 3.65×10^6 [29], wake structure in typical automobile shapes in experimental 3D model with a Re = 4.29×10^6 [3]. Another case, is lower order Reynolds number for three – dimension studies of lateral vortex dynamics behind Ahmed body. For a Re = 54000, which was two orders lower than the one in the original Ahmed body case, Uruba [33] studied the vortex dynamics of the lateral vortex pair created in the wake and the flow field behind the Ahmed body for subcritical (25^o) and supercritical (35^o) slant angles. In that lower – order Reynolds number, Uruva observed a completely different behaviour in terms of topology and intensity of the flow.

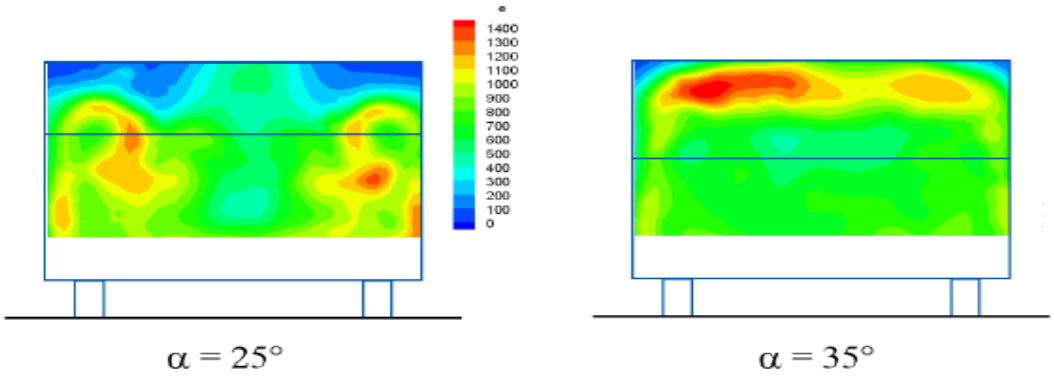

Fig. 23 : Fluctuation velocity variance distribution for two different slant angles of the Ahmed body model (*25^o* and *35^o*) according to Uruba [33]. The change in topology of the flow, is apparent

More specifically, as seen in Fig. 23, Uruva observed that in the 35^o angle, the maximum dynamical properties of the flow tend to move close to the roof, in contrast to the 25^o slant angle in which they are mostly limited inside the lateral vortices.

Numerical studies have also been performed for different numerical methods with Re = $7.68x10^5$ [34], or even in higher – order methods, such as the work of Ichinose and Ito [53], in an effort to achieve an accurate prediction of the drag coefficient in bluff bodies using CFD, with a Reynolds number of Re = $1.93x10^6$, based on inlet velocity and bluff body length.

2.4 Freestream Velocity

As with Reynolds number, different conclusions can be reached about the flow and its other parameters, such as drag or lift coefficients, flow separation, freestream turbulence intensity, or wake flow by changing the flow velocity around the bluff body either through experimental sessions or while running a simulation. Theoretically, there are no restrictions to the flow velocity that will be applied to the model, whether it's experimental or computational, however the most common flow velocities encountered are between 20 – 60 m/s and this is mostly due to an effort of keeping up with values encountered in real scale automobile bodies. The freestream velocity is inextricably connected to the Reynolds number. Ahmed performed a series of experiments [3] in order to examine the wake flow behind typical automobile shapes, with maximum continuous windspeed of 60 m/s, with a turbulence intensity in the empty section of less than 0.05%.

In an effort to supress separation on the rear slant angle in a 3D model by comparing the original Ahmed body model with one bearing a rounded edge with 80mm radius curvature instead of a slant angle of 25^o, Thacker et al [6], applied a freestream velocity of 60 m/s. Having a freestream turbulence intensity below 0.3% and a value of 0.5% for mean flow homogeneity, managed to prove, that drag coefficient Cd in comparison to literature values for the sharp-edge configuration is overestimated by 30%.

Hinterberger et al [35], performed a LES around the Ahmed body model for a bulk velocity of 40 m/s, in a Re number of $2.8x10^6$ with a ¾ open test section (no side walls or ceiling) and a slant angle of 25^o, comparing the results with the experiments. A well captured flow structure was observed along with a good agreement of the time – averaged quantities. However, some discrepancies were noticed, mostly in the lower back of the slant back and the case was called as very good for further research and development.

There are cases, though, in which the freestream velocity might be even smaller than 30 m/s. For a slant angle $\alpha = 25^o$ and a flow velocity of 0.1 m/s, corresponding to Re $3x10^4$, Spohn and Gillieron [36] experimentally examined flow separations on the front and rear part of the Ahmed body model, by visualizing the flow, in order to indicate how vortical structures arise from flow separations, inside

the near wake zone. Open front separation zones were observed, with periodic shedding, with a tendency of these regions to decrease with increasing Reynolds number. However, detrimental effects were exhibited, such as sound generation and unsteady interaction with the vortical structures arising from the hatch panel. The experiment also pointed at a more complex rear part separation zone than the one found by Ahmed et al [2] and an additional region of attachment which came to agreement with previous numerical simulations performed [37]. In addition to the above, an open central detached flow region was observed, with the fluid above the panel being evacuated slowly in the wake, by two separation foci.

Freestream flow is of great importance as well, when the case involves two trailing bodies, as there is a direct connection between freestream flow, the wake created by the leading body and how it affects the trailing one. For a velocity of 21.5 m/s, Motin et al [38] observed that in the leading vehicle, both the magnitude and variation of displacement thickness, remain the same as that of a single vehicle, though in the trailing one and in connection with the distance between the vehicles, the variation pattern remains the same but with an almost doubled magnitude. Despite that though, the vehicle spacing does not improve friction coefficient and friction drag coefficient values.

2.5 Domain Size – Grid

The size/domain of the grid used to run a simulation and the domain size when it comes to experimental features is extremely important. Again, depending on the goals of the studies performed, there is a wide variation in the experimental or computational domain sizes present. However, they have all as a common target to be as realistic as possible and approach velocity, pressure, drag and lift values among others, in the most realistic possible way. The number of elements used in the grid domain is crucial, as well as the grid quality, in order to achieve convergence in a computational model but the number of elements is inextricably connected with the computational space available.
There are two sorts of grids:

I.) Unstructured grid: Very good for reproducing complex geometries as the element may have any shape and it's the most flexible type of grid. Because of the inability to write the data of the cells in an orderly way, it has the disadvantage of that requires higher computational cost for the calculation than the structured grid.

II.) Structured grid: The three directions of the adopted reference system are referred to by three parameters that identify the position of the cells that compose the grid. It is very efficient for calculation but it is less flexible since it

exhibits complications in complex geometries, therefore it is not particularly suitable.

The Ahmed body exhibits various sorts of complexities in grid construction around it, and various approaches have been applied for the computational domain. Due to these complexities in the structure and for flexibility reasons connected to the element shape, an unstructured grid will be used in this thesis.

Yunlong et al [34], splited the computational domain into 46 blocks, for a computational power of 16 processors for parallel computation, so that each processor is responsible for the computation of several blocks. A non-uniform grid was constructed with the near wall region using smaller grid size to control the first y+ at around 20 to 50, in order to achieve reduction of the total elements. The total element number was 460,000.

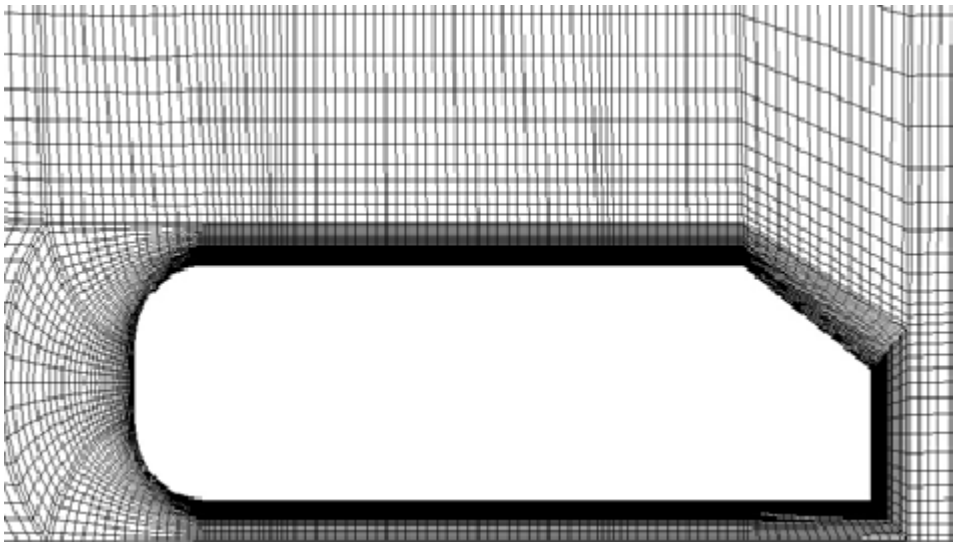

Fig. 24 : Grid distribution near the Ahmed body according to Yunlong et al. [34], consisting of 460,000 elements.

In LES simulations around the Ahmed body [35], the subcritical 25^{o} angle in the downstream of the Ahmed body, was examined in two grids, first having 93 blocks and $8.8x10^{6}$ cells and an orthogonal outer block structure. The second grid consisted of 214 blocks and $18.5x10^{6}$ cells, but both grids featured an O-grid structure around the body. The O-Grid structured allowed for grid refinement in the wall – normal direction near the body boundaries. An outer O-Grid structure was selected in the second grid, having as a target to concentrate the grid points close to the body in spanwise and streamwise direction. As observed in Fig. 25 and Fig. 26, different mean streamwise and root mean streamwise velocity profiles were exhibited for a coarse and a finer grid.

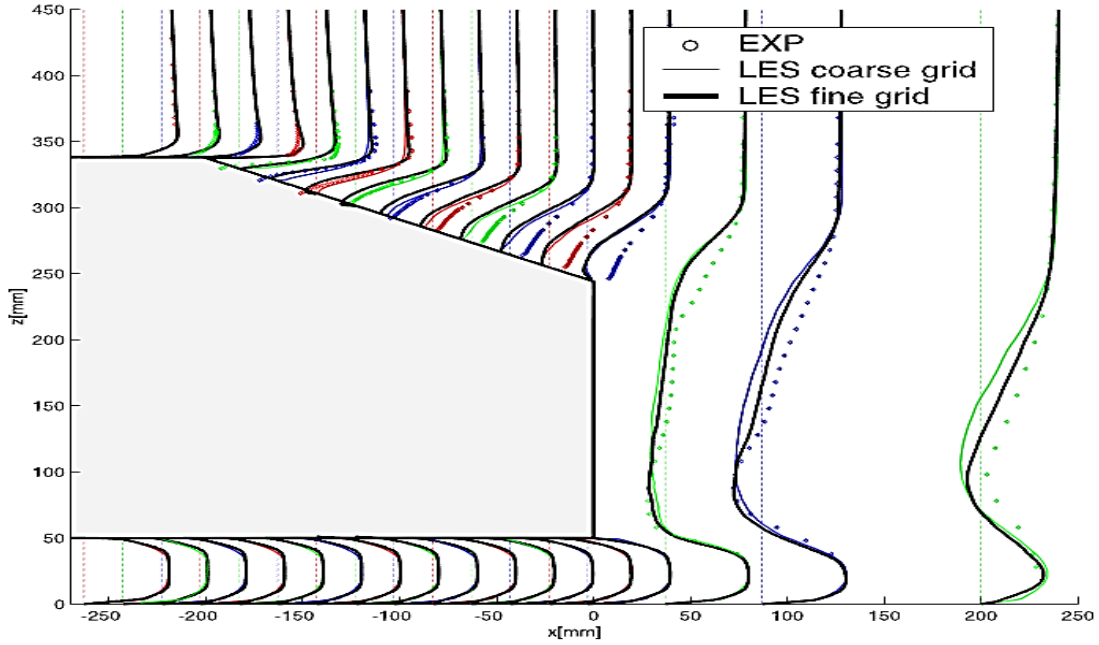

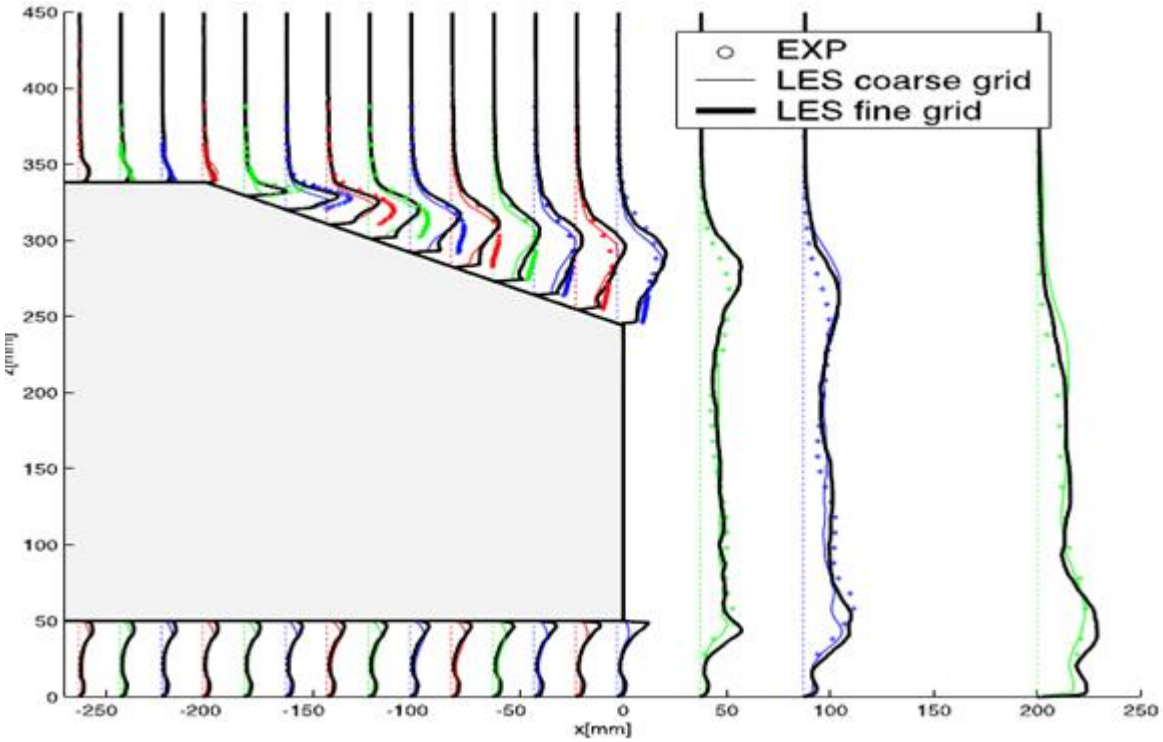

Fig. 25 (above) and Fig. 26 (below) : Differences in rear body and near wake mean streamwise (above) and root mean streamwise (below) profiles for LES coarse and fine grids over the symmetry plane, as observed by Hinterberger et al. [35].

The number of elements used in a grid is of crucial importance to the simulation running on this particular grid. Finer grids tend to interpret physical phenomena in a much better and more detailed way, but the computational cost has to be taken into account, as well as the time a simulation will consume on the chosen method to complete. In Fig. 27 and Fig. 28, the difference between a 500,000 and a 1,900,000 cells grid is exhibited, for a slant angle of 25^{o} [54].

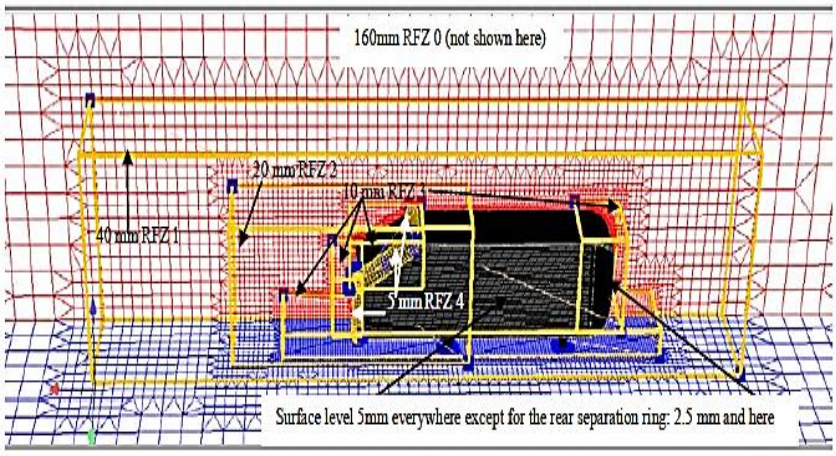

Fig. 27 : Coarse grid of the *25°* slant angle Ahmed body with 500,000 elements (Bordei & Popescu [54])

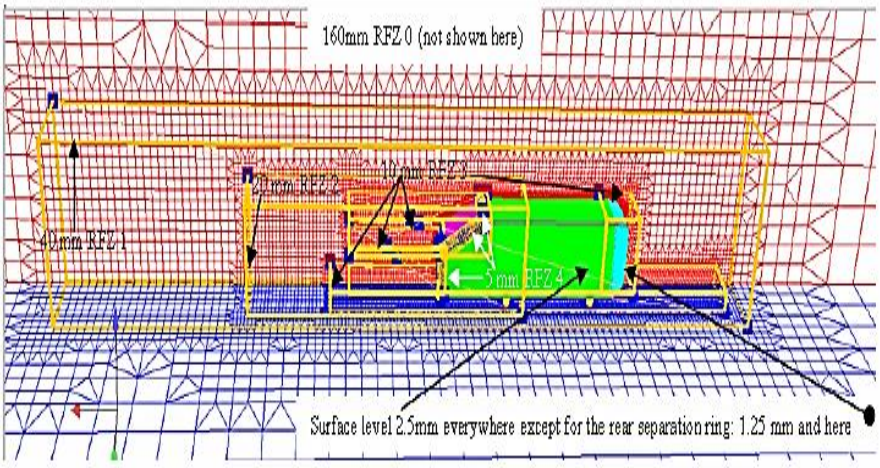

Fig. 28 : Finer grid of the *25°* slant angle Ahmed body with 1,900,000 elements (Bordei & Popescu [54])

In terms of experimental domains, in a study for more insight into wake effects, Ahmed [3] performed tests in a subsonic open test – section, closed – return wind tunnel with a square nozzle of $9m^2$ cross – section and a test – section length of 5.86m. His basic automobile model was a quarter scale (1.044 m long) of an actual one. It had a length : width : height ratio of 3.02 : 1.16 : 1 and a ground clearance of

0.05 m. at its lowest point. There was a total frontal area of 0.1122 m^2 (1.25% of the wind – tunnel nozzle area).

Unstructured tetrahedral grid, which presents wedge elements of boundary layers, the accuracy of which lays in the very thin boundary layer portion of the mesh, by the ability of the elements to capture and develop a flow field around the Ahmed body, has been presented in the work of Franck and D'Elia [11]. The wedge element was defined as an element of six nodes and special consideration was needed for the parallel implementation, since both tetrahedral and wedge elements were used, for a final mesh of 162,000 nodes and 930,000 tetrahedral elements. Fig. 29 shows the mesh used in this study, while Fig. 30 shows some details of the structured layer.

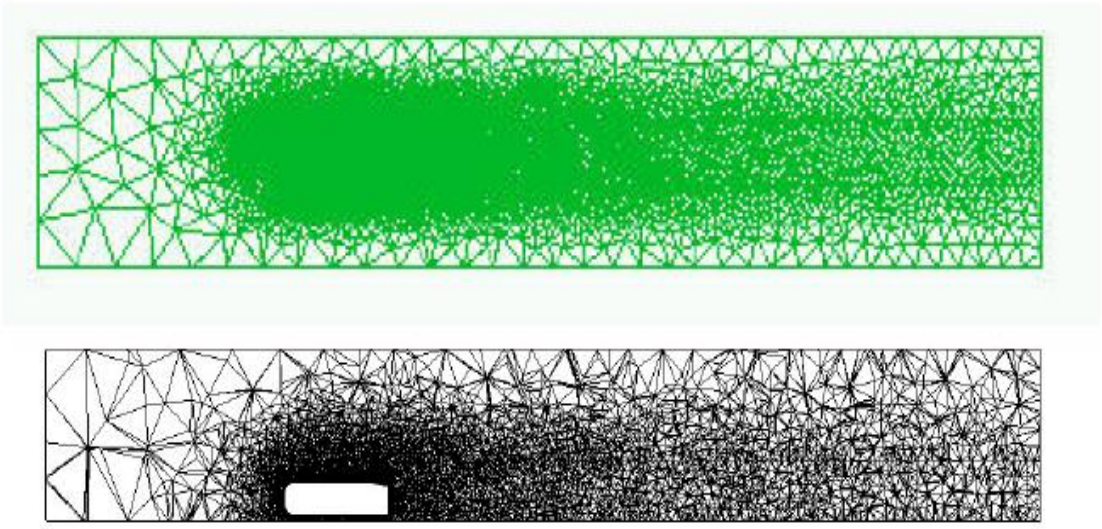

Fig. 29 : Above: Meshing on the floor surface. Below : Refined mesh zones along a longitudinal cut (Franck & D'Elia [11]).

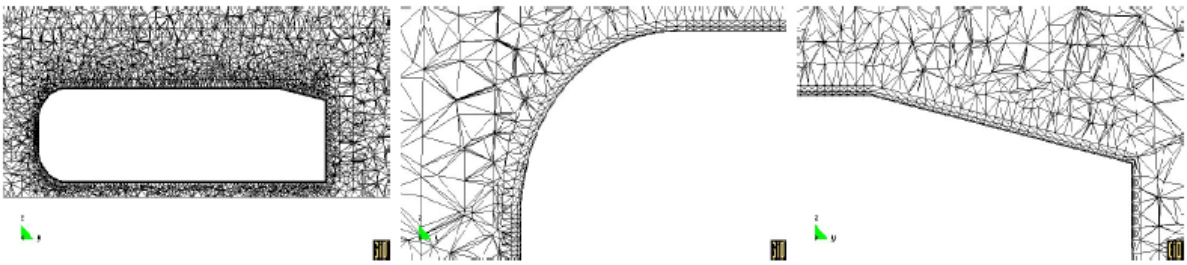

Fig. 30 : Details of the structured layer in the grids created by Franck & D'Elia [11]. From left to right: a.) Longitudinal cut on the whole body, b.) Cut in the body Front, c.) Cut on the rear part of the body

In his work for a study of lateral vortex dynamics behind the Ahmed body, Uruba [33], placed a 3:20 scaled geometrically similar to Ahmed body model in the open test section in the tunnel exit sized 250x250 mm, with a length of 156.6 mm, for two different slant angles: subcritical, of 25^{o} and supercritical of 35^{o}.

However, there were experimental studies, such as the one by Aider et al [4] that were conducted for different Ahmed body dimensions, in order to try and resemble more the quarter scaled dimensions of a modern small vehicle, with the dimensions being 0.29 m. height, 0.34 m. width, 0.9 m. length. Curvature radius of the rear slant was 0.45 m., with the study's model differentiating as well in the height of the underbody, which was 0.04 m. instead of 0.05 m. in the model of the original [2] Ahmed study.

2.6 Turbulence Models Used

In accordance to the Reynolds number, the flow of a fluid can be discriminated as laminar or turbulent. A laminar flow in engineering applications is a rather rare occasion, due to the speed of the applications in conjuction with the sizes and shapes of the bodies involved. Usually, Reynolds numbers are high, at least in the order of 10^{5}. Turbulent flow is subject to a few characteristics [40], [41]:

I.) Variations in the mean values of velocity, pressure and temperature
II.) Interactions between vortices created and the entire range of motion
III.) The flow is irregular, exhibiting randomness and chaotic behavior in the properties of the fluid, with own energy spectrum, according to wavelength. There is a characteristic energy spectrum pattern for each size and it's not uniformly distributed over all frequencies (white noise).
IV.) Turbulent flow occurs at high Reynolds numbers
V.) Turbulence exhibits a continuity, as upon beginning it maintains a self - sustenance of movement with creation of new eddies and vortices, of different sizes, which will later dissipate, due to viscous forces.
VI.) It involves a large spectrum of temporal and spatial scales
VII.) Dissipative at the Kolmogorov scales (small scales)
VIII.) It's always three – dimensional and mixing the flow and high diffusion of mass, momentum and energy.
IX.) Due to the fact that small scales are much longer than molecular ones, the flow is treated as a continuum.

The smoke coming out of a cigarette, is a very good example of turbulence phenomena, with a laminar flow (flow in a straight streamline) when leaving the cigarette, which after a while and under the effect of surrounding air exhibits chaotic characteristics. This is an indication of turbulence in the flow of the smoke.

The production term P_k is where most of the the largest eddies receive their turbulent kinetic energy from and the cascade process describes how this turbulent energy is divided among other, smaller eddies until it reaches Kolmogorov scales, which are the smallest. After that and due to viscous stresses, they start transforming into thermal energy, via the dissipation term ε. The sum of Reynolds normal stresses in every direction, divided by two could be defined as Turbulent kinetic energy. For the trace Reynolds stress tensor divided by two:

$k = \frac{1}{2} \cdot \overline{u_i}' \cdot \overline{u_i}'$ =>

$k = \frac{1}{2} \cdot (\overline{u'_1}^2 + \overline{u'_2}^2 + \overline{u'_3}^2)$

therefore, the total kinetic energy of the flow can be defined as

$$k = \int_0^\infty E(k)\, dk \qquad \textbf{EQ. A}$$

where $k = \frac{1}{D}$, D and E(k) are the wavenumber, Diameter of the Eddy and Energy, respectively.

2.7 DNS (Direct Numerical Simulation)

The exact equation of Navier – Stokes is solved without any sort of filtering on turbulence. This simulation method requires a great amount of calculation time and in addition to that, an excessive computational cost is implemented, as well. Due to the aforementioned reasons, it has almost never been used in industrial applications. However, apart from the numerical error, the DNS method produces a solution which describes the problem as closely as possible.

2.8 RANS Method

In the RANS method, turbulence models for the whole range of turbulence scales are used and only the equations of the averaged flow quantities are implemented. RANS method results are less strict in terms of approximation, but the more logical calculation time in comparison to other methods and the reduced computational cost of the method makes it suitable for a variety of applications related to engineering.

According to Lorenz [42], the randomness exhibited in turbulent motion, which in order to be studied, statistical methods are used, is only apparent as some types of system of non – linear equations, are inextricably connected to the to the initial conditions of the system, and major changes to the evolution of the flow field can take place following minor differences in the initial conditions. The following phenomena might exhibit randomness, which, by using the Reynolds decomposition can isolate contribution of turbulence on the average flow field.

Reynolds decomposition, considers the flow physics quantities as the sum of a value averaged over time and a fluctuating value. For a quantity ϕ, one can define the time average of a generic physics quantity as:

$$\bar{\varphi} = \frac{1}{\Delta t} \cdot \int_{t_0}^{t_0+\Delta t} \varphi \, dt \qquad \textbf{EQ. B}$$

Reynolds decomposition, defines that part of the fluctuating quantity is indicated by a prime. The flow parameters (velocity and pressure) can be written, by applying it, as following:

$$u_i = \overline{u_i} + u_i' \qquad \textbf{EQ. C}$$

and

$$p = \bar{p} + p' \qquad \textbf{EQ. D}$$

Separation of the average components and the fluctuating values inside the equations is possible by applying the the properties of the time average, thus by applying the Reynolds decomposition in the mass conservation and Navier – Stokes equations. By doing a time – average, the continuity equation becomes

$$\nabla \cdot \bar{v} = 0 \qquad \textbf{EQ. E}$$

Subtracting this to the Navier – Stokes equation, it will be

$$\nabla \cdot v' = 0 \qquad \textbf{EQ. F}$$

2.9 LES (Large Eddy Simulation)

In this method, only the large scale of turbulence is calculated. Turbulence is filtered to achieve that and the evaluation of the effects taking place to the flow field, owing to smaller scales, is done by the use of turbulence models. These turbulence models, close the problem and allow resolution of the flow.

2.10 Spalart – Allmaras Turbulence Modelling

This type of turbulence modeling is provided by FLUENT. It is a model of only one equation describing turbulent viscosity. Solves a transport equation for a viscosity like variable $\tilde{v}$. In their work on Ahmed body, Rajsinh et al. [46], studied the effectiveness of the Spalart – Allmaras turbulence model for modeling the flow over the Ahmed body, in order to show the behavior of the Spalart – Allmaras turbulence model, as well as how the grid layout affects numerical results. For a 3D Ahmed body model with a slant angle of 25^{o}, discretized with tetrahedral mesh elements, consisting of 2.85 Million nodes and 15.55 Million elements, two upstream velocities of 40 m/sec and 60 m/sec were applied. Reynolds number was $2.78x10^{6}$. In the first case for upstream velocity of 40 m/sec, the basic difference was the flow reattachment which was different between the results of the study and those of the experimental data, though separation was according to the experimental data.

Fig. 31 is exhibiting the grid distribution around the Ahmed body in the Rajsinh et al. study

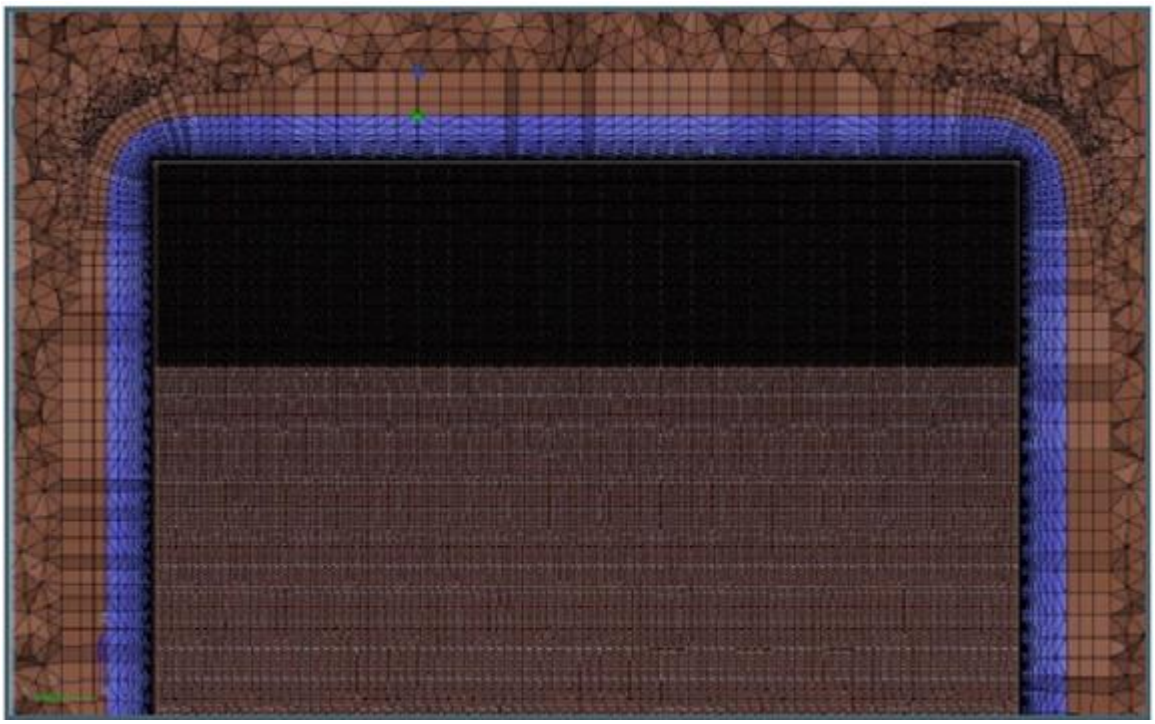

Fig. 31 : Grid distribution along the Ahmed body according to Rajsinh et al. [46]

Fig. 32 shows a cut – plane along the X – axis, based on the same study. The grids were created for 2.85 Million nodes, 15.55 Million elements and 16 layers around the Ahmed body with 16 layers around the Ahmed body, with a first layer thickness of 0.2 mm and a 1.2 boundary layer growth.

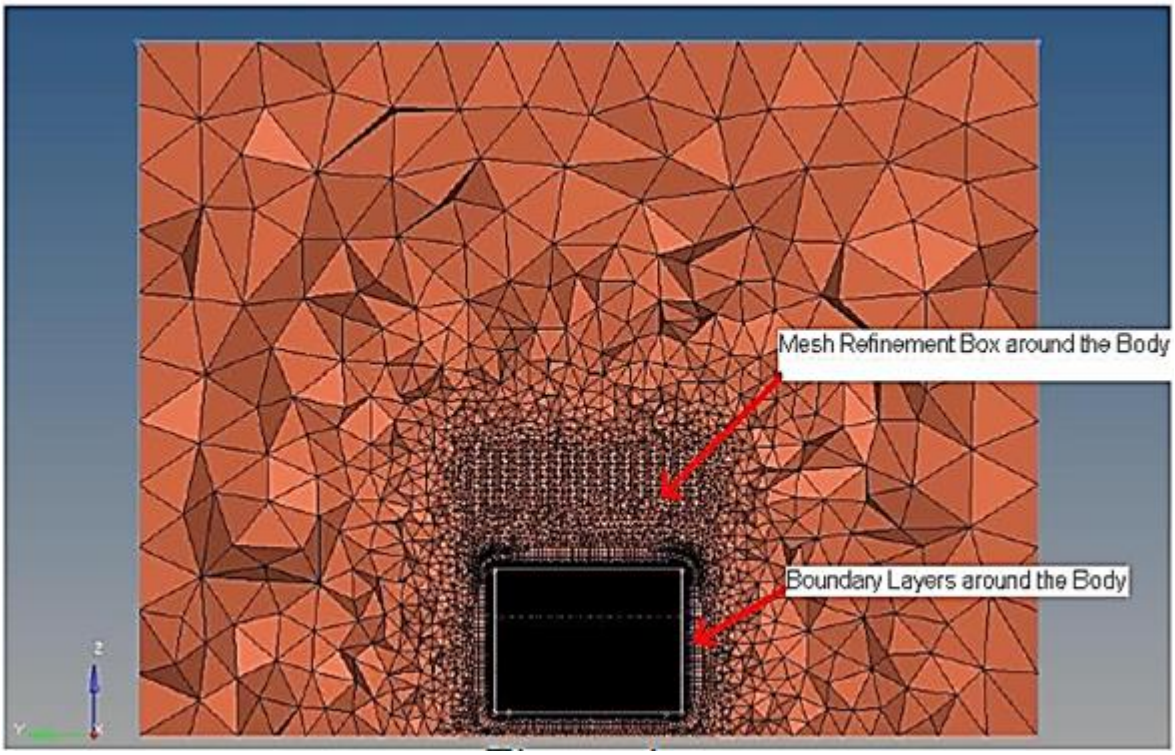

Fig 32 : Cut plane on the Ahmed body along X – Axis according to Rajsinh et al. [46]

Limitations to the S – A model were present, mostly concerning the wake behind the body and the reattachment on the slant, that was not presented clearly. The same virtues were exhibited for higher velocity (60 m/sec) as well, with almost identical results, except for changes in the recirculation size and its location in the wake, as well as a slant end recirculation bubble which became more clear as velocity was rising. However, the flow over the rear slant cannot be predicted well as it comes in contrast with experimental data.

Concerning the drag coefficient comparison between the computational and experimental data, despite that the fact that the drag on the slant is over – estimate the S – A model gives the same tendency as the experiments, but in general the flow on the slant cannot be predicted correctly on the slant by this model.

The latter, was pointed by Kapadia et al [47] for the 25^{o} angle case, by performing a Spalart – Allmaras based DES simulation over the Ahmed body. The conclusion was that flows close to separation and differences in their prediction, may lead to various changes, as in this particular 25^{o} case. These sorts of flows continue being a challenge to predictive methods.

Chapter 3 : Methodology

3.1 Governing Equations

There are three conservation laws upon which the dynamical behavior of a fluid is determined. These conservation laws are

I.) The conservation of mass
II.) The conservation of momentum
III.) The conservation of energy

The derivation of the principal equations of fluid dynamics is based upon how these laws define the dynamical behavior of a fluid. In order to gain a better overview of all the terms involved in a flow, the aforementioned equations can be gathered in one equations system. In the new system of equations used, two new terms will be entered.

3.1.1 Continuity Equation

The basic principle of the law of mass conservation is that mass cannot be created or disappear from a fluid system – in single phase fluids. The continuity equation is also characterized by the lack of diffusive flux, as in the case of a displacement takes place in fluid particles, should any variation of mass occur, in a fluid at rest. In Fig. 33, a fixed in space finite control volume can be observed [55]:

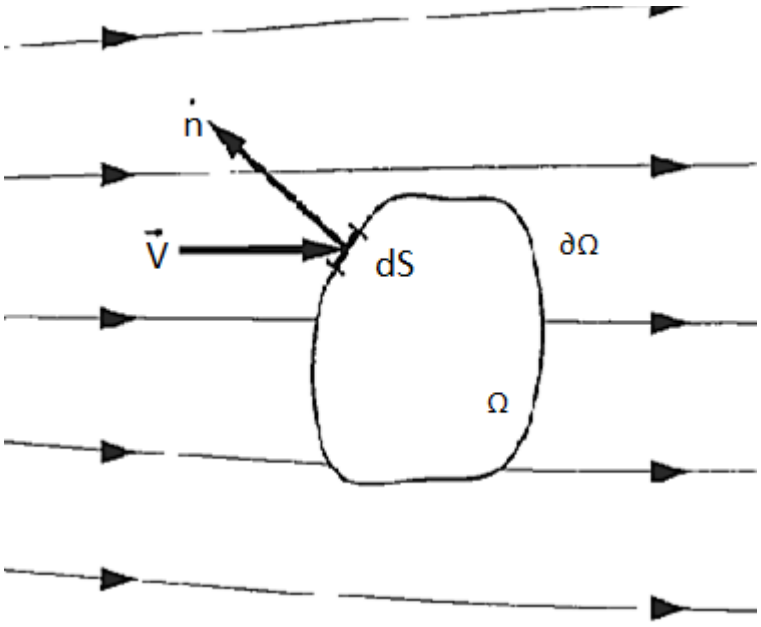

Fig. 33 : The definition of a fixed in space finite control volume (Blazek [55])

Where:

∂Ω -> Closed surface bounding the arbitrary finite region of the flow

Ω -> Control volume

dS -> surface element

$\vec{n}$ -> unit normal vector

For a density ρ and inside the finite volume Ω, the time rate of change of the total mass will be

$$\frac{\partial}{\partial t} \int_{\Omega} \rho \, d\Omega \qquad \textbf{EQ. 1}$$

Due to the convective flux amount of quantity U, it is equal to the sum of the contributions. It enters the control volume with velocity $\bar{v}$, through the boundary. Hence U $\bar{v}$

$$- \oint_{\partial\Omega} U \, (\vec{v} \cdot \vec{n}) \, dS \qquad \textbf{EQ. 2}$$

According to the generalised Flick's gradient law which expresses the diffusive flux

$$\oint_{\partial\Omega} k \rho \, [\nabla \, (\frac{U}{\rho}) \, \vec{n} \,] \, dS \qquad \textbf{EQ. 3}$$

where

k -> thermal diffusivity coefficient

due to surface forces Q_V, $\overrightarrow{Q_S}$ and volume, respectively, it's

$$\int_{\Omega} Q_V \, d\Omega + \oint_{\partial\Omega} (\overrightarrow{Q_s} \cdot \vec{n}) \, dS \qquad \textbf{EQ. 4}$$

The general law for the scalar quantity U, after summing the aforementioned contributions, will be

$$\frac{\partial}{\partial t}\int_{\Omega} \mathrm{U}\, d\Omega + \oint_{\partial\Omega} [\mathrm{U}\,(\vec{v}\cdot\vec{n})\, dS - k\rho\,(\nabla U^{*}\cdot\vec{n})]\, dS =$$

$$= \int_{\Omega} Q_V\, d\Omega + \oint_{\partial\Omega}(\overrightarrow{Q_s}\cdot\vec{n})\, dS \qquad \textbf{EQ. 5}$$

where

U* -> quantity U per unit mass ($\frac{U}{\rho}$)

It should be noted that EQ. 5 is still valid, despite the nature of the conserved quantity (vector instead of scalar). The main difference, however, lies with the convective and diffusive fluxes as instead of vectors, they will be presented as tensors with $\overline{\overline{F_C}}$ being the convective flux tensor and $\overline{\overline{F_D}}$ the diffusive flux vector. Differences are exhibited as well in the volume and surface sources, changing into vector $\overrightarrow{Q_v}$ and tensor $\overline{\overline{Q_S}}$, respectively. Taking these changes into account, EQ. 15 is the new form of the conservation law for a general vector quantity $\vec{U}$:

$$\frac{\partial}{\partial t}\int_{\Omega} \vec{U}\, d\Omega + \oint_{\partial\Omega} [\,(\overline{\overline{F_C}} - \overline{\overline{F_D}})\cdot\vec{n}\,]\, dS =$$

$$= \int_{\Omega} \overrightarrow{Q_V}\, d\Omega + \oint_{\partial\Omega}(\overline{\overline{Q_S}}\cdot\vec{n})\, dS \qquad \textbf{EQ. 6}$$

EQ. 5 and EQ. 6, which are the integral formulations of the conservation law possess two valuable properties

I.) The variation of U wholly depends on the flux across the across the boundary ∂Ω and not on any flux inside the control volume Ω, if there are no volume sources present

II.) Upon presence of discontinuities in the flow field (shocks, etc) these forms remain valid.

In order to find the contribution across each surface element from the convective flux for every surface element dS, the mass of fluid through some surface fixed in space should be taken into consideration. EQ. 7 will be the product of (density) x (surface area) x (velocity component perpendicular to the surface).

$$\rho\,(\vec{v}\cdot\vec{n})\, Ds \qquad \textbf{EQ. 7}$$

The ($\vec{v} \cdot \vec{n}$) product of EQ. 7 defines whether there is inflow or outflow, since the unit normal vector $\vec{n}$ always points out of the control volume. The decisive factor is $\vec{v}$. More specifically if the product is negative, there is inflow and in the opposite case of a positive product, there is outflow. The integral form of the continuity equation is

$$\frac{\partial}{\partial t}\int_{\Omega} \rho \, d\Omega + \oint_{\partial\Omega} \rho \, (\vec{v} \cdot \vec{n}) dS = 0 \qquad \textbf{EQ. 8}$$

EQ. 8, is the conservation law of mass.

3.1.2 Momentum Equation

For the momentum of an infinitesimally small area of the control volume Ω and taking into account Newton's second law, which states that "the variation of momentum is caused by the net force acting on a mass element", it is

$$\rho \cdot \vec{v} \cdot d\,\Omega \qquad \textbf{EQ. 9}$$

and for the variation in time of the momentum within the control volume

$$\frac{\partial}{\partial t}\int_{\Omega} \rho \, \vec{v} \, d\Omega \qquad \textbf{EQ. 10}$$

The product of density times the velocity ($\rho \cdot \vec{v}$) will ultimately give us

$$(\rho \cdot \vec{v}) = [\, \rho u, \ \rho v, \ \rho w \,]^{T} \qquad \textbf{EQ.11}$$

The three components ρu $\vec{v}$, ρv $\vec{v}$ and ρw $\vec{v}$ for the x,y and z component respectively, in the Cartesian coordinate system comprise the convective flux tensor, which describes the transfer of momentum across the boundary of the control volume. The association between the convective flux tensor and the conservation of momentum is given by EQ. 12:

$$-\oint_{\partial\Omega} \rho \, . \vec{v} \, (\vec{v} \cdot \vec{n}) dS \qquad \textbf{EQ. 12}$$

Two forces act in the control volume he forces in which the fluid element is exposed to, since there is a zero value of the diffusion flux, meaning momentum is not possible to exist, since the fluid is in rest. In detail:

I.) Surface forces

Result from

a.) The fluid surrounding the volume and the pressure distribution it might impose

b.) The friction between surface of the volume and the fluid, as this causes shear and normal stresses to be exhibited

Surface forces act directly on the surface of the control volume.

II.) External body or volume forces

Coriolis, gravitational, buoyancy, centrifugal, etc. Electromagnetic forces may be applied and these forces act directly on the mass of the volume.

The contribution to the momentum conservation by the (external) body force will be

$$\int_{\Omega} \rho \, \overrightarrow{f_e} \, d\Omega \qquad \textbf{EQ. 13}$$

An isotropic pressure component and a viscous stress tensor are what the surface sources consist from

$$\overline{\overline{Q_S}} = -p \, \overline{\overline{I}} + \overline{\overline{T}} \qquad \textbf{EQ. 14}$$

Where

$\overline{\overline{T}}$ -> viscous stress tensor

$\overline{\overline{I}}$ -> unit tensor

Fig. 34 [55] is exhibiting how surface forces act on the control volume and how they effect it:

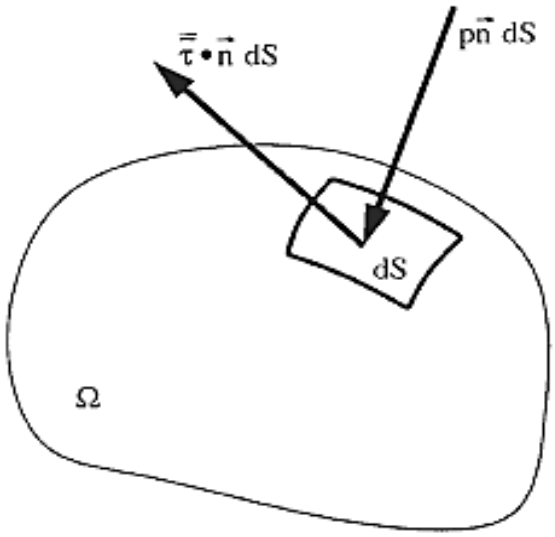

Fig. 34 : A surface element of the control volume and how surface forces act on it (Blazek [55])

In accordance with the conservation law, if the above contributions are summed up, EQ. 15 will produce the momentum conservation equation inside an arbitrary, fixed in space, control volume Ω:

$$\frac{\partial}{\partial t}\int_\Omega \rho\,\vec{v}\,d\Omega + \oint_{\partial\Omega} \rho\,.\vec{v}\,(\vec{v}\cdot\vec{n})\,dS =$$

$$= \int_\Omega \rho\,\overrightarrow{f_e}\,d\Omega - \int_\Omega \rho\,\vec{n}\,dS + \oint_{\partial\Omega}(\bar{\bar{T}}\cdot\vec{n})\,dS \qquad \textbf{EQ. 15}$$

EQ. 15 is the conservation law of momentum.

3.1.3 Energy Equation

Application of the first law of Thermodynamics in the control volumes of Fig. 40 (in Chapter 3.6.3) leads to the conclusion that all changes in the time of total energy inside the volume are the outcome of the heat flux and the rate of work of forces acting on the volume.

In order to reach a conclusion for the total energy per mass unit of a fluid, its kinetic energy per unit mass will have to be added to its internal energy per unit mass, as in EQ. 16:

$$E = e + \frac{|\vec{v}|^2}{2} \Rightarrow$$

$$E = e + \frac{u^2 + v^2 + w^2}{2} \quad \textbf{EQ. 16}$$

where

E -> total energy per unit mass

e -> internal energy per unit mass

$\frac{|\vec{v}|^2}{2}$ -> kinetic energy per unit mass

In this case, ρE which is the total energy per unit volume is the conserved quantity and within the volume Ω, its variation in time will be as in EQ. 17

$$\frac{\partial}{\partial t} \int_{\Omega} \rho \, E \, d\Omega \quad \textbf{EQ. 17}$$

The contribution of the convective flux (according to the steps followed to reach EQ. 5) wil be

$$- \oint_{\partial\Omega} \rho \, . E \, (\vec{v} \cdot \vec{n}) dS \quad \textbf{EQ. 18}$$

The diffusive flux ($\vec{F}_D$) appearing now, according to Flick's law (EQ. 3) is proportionate to the conserved quantity per unit mass. Only the internal energy becomes effective since it is not defined for fluids at rest. Therefore

$$\vec{F}_D = -\gamma \, \rho \, k \, \nabla_e \quad \textbf{EQ. 19}$$

where

$\gamma = C_p / C_v$ -> ratio of specific heat coefficients

k -> thermal diffusivity coefficient

The diffusion of heat due to molecular thermal condition, which is one part of the heat flux into the control volume and is represented in the diffusion flux. The heat transfer occurs due to temperature gradients. Making use of Fourier's law of heat conduction, EQ. 19 can be written as

$$\vec{F}_D = -k \, \nabla \, T \quad \textbf{EQ. 20}$$

where

T -> absolute static temperature

Volumetric heating due to absorption or emission of radiation or chemical reactions, is what the other part of the net heat flux consists of. Taking into account the momentum equation and the rate of work by body forces ($\overrightarrow{f_e}$), the volume forces will be

$$Q_V = \rho \overrightarrow{f_c} \cdot \vec{v} + \dot{q}_h \qquad \textbf{EQ. 21}$$

where

$\dot{q}_h$ -> Rate of heat transfer per unit mass (heat sources)

The surface sources (Q_S) correspond to the time rate of work done by the pressure. They also correspond to the shear and normal stresses on the fluid element. A good example of which is Fig. 34. The surface forces contribution to the conservation of energy is defined as follows

$$\vec{Q}_S = -p \vec{v} + \bar{\bar{T}} \cdot \vec{v} \qquad \textbf{EQ. 22}$$

By assorting EQ. 16 – EQ. 22, we have for the energy conservation equation

$$\frac{\partial}{\partial t} \int_\Omega \rho E \, d\Omega + \oint_{\partial\Omega} \rho . E \, (\vec{v} \cdot \vec{n}) dS = \oint_{\partial\Omega} k (\nabla T \cdot \vec{n}) dS +$$

$$\int_\Omega (\rho \overrightarrow{f_c} . \vec{v} + \dot{q}_h) \, d\Omega - \oint_{\partial\Omega} \rho \, (\vec{v} \cdot \vec{n}) dS + \oint_{\partial\Omega} (\bar{\bar{T}} \cdot \vec{v}) \, \vec{n} \, dS \qquad \textbf{EQ. 23}$$

In EQ. 24 a general (utilized) relation between total enthalpy, total energy and pressure is exhibited

$$H = h + \frac{|\vec{v}|^2}{2} \quad \Rightarrow$$

$$E = \frac{p}{\rho} \qquad \textbf{EQ. 24}$$

The final energy equation is EQ. 25, in which the pressure term ($p \vec{v}$) , the convective term ($\rho E \vec{v}$) are gathered, along with application of the EQ. 24:

$$\frac{\partial}{\partial t} \int_\Omega \rho E \, d\Omega + \oint_{\partial\Omega} \rho . H \, (\vec{v} \cdot \vec{n}) dS =$$

$$= \oint_{\partial\Omega} k (\nabla T \cdot \vec{n}) dS + \int_\Omega (\rho \overrightarrow{f_c} . \vec{v} + \dot{q}_h) \, d\Omega + \oint_{\partial\Omega} (\bar{\bar{T}} \cdot \vec{v}) \, \vec{n} \, dS \quad \textbf{EQ.25}$$

EQ. 25 is the conservation law of energy.

3.2 Navier – Stokes Equation

From Chapters 3.1.1 – 3.1.3, the equations of mass, momentum and energy were obtained. In order to thoroughly explain some terms encountered, along with reaching the Navier – Stokes equation, two flux vectors will be introduced. These flux vectors are $\overrightarrow{F_c}$ and $\overrightarrow{F_v}$.

The first flux vector $\overrightarrow{F_c}$ in EQ. 1, is the vector of convective fluxes which, for the momentum equation includes the ρ $\vec{n}$ and for the energy equation the ρ ($\vec{v} \cdot \vec{n}$) pressure terms. This term relates with the convective transport of quantities in the fluid. The second term $\overrightarrow{F_v}$, is the connected to the viscous stresses and heat diffusion. This flux vector is the vector of viscous fluxes.

Conducting their scalar product with the unit normal vector $\vec{n}$ and through EQ. 6, 8, 15, 25 (the equations of mass, momentum and energy), the final result will be EQ. 26

$$\frac{\partial}{\partial t}\int_{\Omega}\overrightarrow{W}\,\mathrm{d}\Omega + \oint_{\partial\Omega}\left(\overrightarrow{F_C}\cdot\overrightarrow{F_V}\right)\mathrm{dS} = 0 \qquad \textbf{EQ. 26}$$

Three dimensions of the following five components include the vector $\overrightarrow{W}$ (vector of conservative variables).

$$\overrightarrow{W} = \begin{bmatrix} \rho \\ \rho u \\ \rho v \\ \rho w \\ \rho\ \mathrm{E} \end{bmatrix} \qquad \textbf{EQ. 27}$$

The vector convective flux will be

$$\overrightarrow{F_c} = \begin{bmatrix} \rho\ \mathrm{V} \\ \rho u V + n_x p \\ \rho v V + n_y p \\ \rho w V + n_z p \\ \rho\ \mathrm{H}\ \mathrm{V} \end{bmatrix} \qquad \textbf{EQ. 28}$$

With V being the contravariant velocity. Contravariant velocity is the velocity normal to the surface element dS. If this is defined as the scalar product of the unit normal vector $\vec{n}$ and the velocity vector $\vec{v}$, EQ. 29 is reached

$$\mathrm{V} = \vec{v} \cdot \vec{n} \quad =>$$

$$\mathrm{V} = n_x \cdot u + n_y \cdot u + n_z \cdot u \qquad \textbf{EQ. 29}$$

Total enthalpy is given by EQ. 30:

$$H = h + \frac{\overrightarrow{|v|}^2}{2} \quad =>$$

$$H = E + \frac{P}{\rho} \qquad \textbf{EQ. 30}$$

And for the vector of viscous fluxes

$$\overrightarrow{F_v} = \begin{bmatrix} 0 \\ n_x T_{xx} + & n_y T_{xy} + & n_z T_{xz} \\ n_x T_{yx} + & n_y T_{yy} + & n_z T_{yz} \\ n_x T_{zx} + & n_y T_{zy} + & n_z T_{zz} \\ n_x \Theta_x + & n_y \Theta_y + & n_z \Theta_z \end{bmatrix} \qquad \textbf{EQ. 31}$$

The Θ terms, describe heat conduction and the viscous stresses in the fluid. For the Θ_x, Θ_y and Θ_z terms, respectively:

$$\Theta_x = uT_{xx} + vT_{xy} + wT_{xz} + k\frac{\partial T}{\partial x} \qquad \textbf{EQ. 32}$$

$$\Theta_y = uT_{yx} + vT_{yy} + wT_{yz} + k\frac{\partial T}{\partial y} \qquad \textbf{EQ. 33}$$

$$\Theta_z = uT_{zx} + vT_{zy} + wT_{zz} + k\frac{\partial T}{\partial z} \qquad \textbf{EQ. 34}$$

Viscous stresses are described by a stress tensor $\overline{\overline{T}}$ and are the property that originates from the friction between the surface of an element and a fluid. EQ. 35 is the general form of the stress tensor in Cartesian coordinates.

$$\overline{\overline{T}} = \begin{bmatrix} \tau_{xx} & \tau_{xy} & \tau_{xz} \\ \tau_{yx} & \tau_{yy} & \tau_{yz} \\ \tau_{zx} & \tau_{zy} & \tau_{zz} \end{bmatrix} \qquad \textbf{EQ. 35}$$

Where τ_{xx}, τ_{yy}, τ_{zz} are the normal stresses. The rest of the stresses are considered shear stresses.

The dynamical properties of the medium is the basic sample for evaluation of viscous stresses. Fluids, in which shear stress is proportional to velocity gradient, such as air or water are called Newtonian fluids, taking their name after Isaac Newton. Fluids such as blood or paint, etc exhibiting a non – linear relation between velocity

gradient and shear stress, are characterized as non – Newtonian fluids. The components of the viscous stress tensors can be exhibited in EQ. 36 – 41.

$$T_{xx} = \lambda \left(\frac{\partial u}{\partial x} + \frac{\partial v}{\partial y} + \frac{\partial w}{\partial z} \right) + 2\mu \frac{\partial u}{\partial x} \quad \textbf{EQ. 36}$$

$$T_{yy} = \lambda \left(\frac{\partial u}{\partial x} + \frac{\partial v}{\partial y} + \frac{\partial w}{\partial z} \right) + 2\mu \frac{\partial u}{\partial y} \quad \textbf{EQ. 37}$$

$$T_{zz} = \lambda \left(\frac{\partial u}{\partial x} + \frac{\partial v}{\partial y} + \frac{\partial w}{\partial z} \right) + 2\mu \frac{\partial w}{\partial z} \quad \textbf{EQ. 38}$$

$$T_{xy} = \mu \left(\frac{\partial u}{\partial y} + \frac{\partial v}{\partial x} \right) = T_{yx} \quad \textbf{EQ. 39}$$

$$T_{xz} = \mu \left(\frac{\partial u}{\partial z} + \frac{\partial w}{\partial x} \right) = T_{zx} \quad \textbf{EQ. 40}$$

$$T_{yz} = \mu \left(\frac{\partial u}{\partial z} + \frac{\partial w}{\partial y} \right) = T_{zy} \quad \textbf{EQ. 41}$$

Where

λ -> second viscosity coefficient

μ -> dynamic (kinematic) viscosity coefficient

If the EQ. 36 – 41 are satisfied, the equations system between EQ. 26 – 34 is called the Navier – Stokes equations. As previously seen, mass, momentum and energy are described through the $\vartheta\Omega$ which is boundary for a fixed in space control volume Ω. Often, in literature, upon application of Gauss's theorem, there can be a differential interpretation of EQ. 26. The control volume needs not to be necessarily steady in order for the Navier – Stokes equations to be applied. The aforementioned equations can be applied as a rotating frame of reference, should the control volume is rotating. In some cases in turbomachinery there might be a steady rotation of the control volume.

According to Pulliam and Steger [57] the Navier – Stokes equation might be extended by a term, in the case a deformation might is presented to the control volume, or a translation, something common in cases investigating fluid – structure interaction. The term that needs to be added is one that with respect to the fixed coordinate system, describes the relative motion of the surface element dS. However, the Geometric Conservation Law (GCL) [58, 59] will have to be satisfied [60].

A system of five equations for the five conservative variables (EQ. 27) ρ, ρu, ρv, ρw and ρE is presented through a tree dimensions system in the Navier – Stokes equations, however, unknown field variables occur. These variables are: ρ, u, v, w, E, p and T. By virtue of thermodynamic relations between the state variables, we have to provide two additional equations. Good examples are density as a function of temperature, pressure as a function of density, internal energy as a function of pressure and enthalpy as a function of temperature. The system of equations will be closed, after providing as a function of a state in the fluid, the kinematic viscosity coefficient μ and the conductivity coefficient k.

3.3 Perfect Gas

In this sub – chapter, some methods to close the system of the Navier – Stokes equations, will be presented. These methods can be applied in common situations, such as aerodynamics, in which case it is comparatively safe to make the hypothesis that the working fluid behaves like perfect gas [61]. According to this, EQ. 42 is the new form of the equation of state and EQ. 43, the equation for enthalpy.

$$p = \rho \cdot R \cdot T \qquad \textbf{EQ. 42}$$

where

R -> Specific gas constant

$$h = C_p \cdot T \qquad \textbf{EQ. 43}$$

A relation between total energy to total enthalpy from EQ. 30 along with the equation of state in EQ. 42 will have to be made in order to express the pressure in terms of conservative variables. Substituting EQ. 43 for the enthalpy, will result in EQ. 44 and EQ. 45:

$$R = C_p - C_v \qquad \textbf{EQ. 44}$$

$$\gamma = \frac{C_p}{C_v} \qquad \textbf{EQ. 45}$$

finally, the pressure will be

$$p = (\gamma - 1)\, \rho \left[E - \frac{u^2 + v^2 + w^2}{2} \right] \qquad \textbf{EQ. 46}$$

and along with EQ. 42, the temperature can be calculated. There is a strong dependence on the temperature for the coefficient of dynamic viscosity (μ), however it is weakly affected by pressure. The Sutherland formula is frequently used and in SI units, is

$$\mu = \frac{1.45\, T^{\frac{3}{2}}}{T+110} \cdot 10^{-6} \qquad \textbf{EQ. 47}$$

e.g. for air at T = 288K the result will be $\mu = 1.78 \cdot 10^{-5}$ kg/ms.

A resemblance with the kinetic viscosity coefficient μ, as in how it is affected by temperature is apparent for the thermal conductivity coefficient k, which is virtually constant in the case of liquids and EQ. 48 is used for air and for a Prandtl (Pr) number constant in the entire flow field.

$$k = C_p \frac{\mu}{Pr} \qquad \textbf{EQ. 48}$$

The Prandtl number value for air is Pr = 0.72.

3.4 The Navier – Stokes Equation Applied in a Discretised Grid

In order for the integrals of the viscous and convective fluxes to be evaluated, appropriate control volumes based on the grid should be defined and it is assumed for convenience reasons that the particular control volume that will be examined, does not exhibit a change over time. In this sort of case, we could cast the time derivative of the conservative variable $\overrightarrow{W}$, as following:

$$\frac{\partial}{\partial t}\int_{\Omega} \vec{w}\, d\Omega = \Omega \frac{\partial \overrightarrow{W}}{\partial t} \qquad \textbf{EQ. 49}$$

Hence, EQ. 26 will become

$$\frac{\partial \overrightarrow{W}}{\partial t} = -\frac{1}{\Omega}\left[\oint_{\partial\Omega} \left(\overrightarrow{F_c} - \overrightarrow{F_v}\right) dS - \int_{\Omega} \vec{Q}\, d\Omega \right] \qquad \textbf{EQ. 50}$$

Supposing that flux is constant along the individual face and evaluated at the face's midpoint, spatial discretisation in EQ. 24, is called the approximation of the surface integral on the right side of the equation, by a sum of the fluxes crossing the face of the control volume. A good second order accuracy is offered with this sort of process.

Concerning the source term ($\vec{Q}$), it is considered to be constant inside the control volume, though there might be cases it becomes dominant. In such case, a good course of action, according to Mohanraj et al. [62], would be to evaluate it as the the weighted sum of values from the neighbouring control volumes.

EQ. 49 for a particular volume Ω_I becomes ("I" index refers to the control volume as it may not coincide with the grid) :

$$\frac{d\overrightarrow{W_1}}{dt} = -\frac{1}{\Omega}\left[\sum_{m=1}^{N_F}(\overrightarrow{F_c} - \overrightarrow{F_v})_m \, \Delta S_m - (Q\Omega)_I\right] \qquad \textbf{EQ. 51}$$

where:

N_F -> number of the faces of the control volume Ω_I. It is dependent both on the cell type and the type of the control volume.

ΔS_m -> area of the face m

It should be denoted here that one of the main differences between structured and unstructured grid is the fact that in the latter case, the number of faces change between the control volumes.

The residual, is the term located in the right hand side of EQ. 50, inside the brackets. As a result, EQ. 50 might be shortened down to EQ. 51, which gives us a system of first order ordinary differential equations, when written for all control volumes Ω_I. These equations are hyperbolic in time, in other words a known initial solution must be known in order to proceed:

$$\frac{d\overrightarrow{W_1}}{dt} = -\frac{1}{\Omega}\overrightarrow{R_1} \qquad \textbf{EQ. 52}$$

3.5 Numerical Approximation of Various Finite Volume Schemes

In terms of solving discretised governing equations such as EQ. 26, while using a finite volume scheme there are some basic methods and techniques that have an essential role in the definition of the control volumes and locating the flow variables with respect to grid points.

I.) Cell – centered scheme

Similar control volumes. The centroids of the grid cells are inextricably connected with the flow variables as in [63], [64], [65]

II.) Cell – vertex scheme with overlapping control volumes

The control volumes are defined as the union of all grid cells with a common respective node. This results in overlapping control volumes between neighboring vertices. The grid vertex is assigned of the flow quantities. More detailed analysis can be found in the work of Mavriplis et al. [66], [67]. However, this particular scheme is no longer used.

III.) Cell – vertex scheme with median – dual control volumes

Creation of the control volumes comes through connection of the centroids of surrounding elements, edge – midpoints and face – centroids. Grid vertices store the flow variables. By this process, the control volumes encapsulate the corresponding grid points and a result, a non – overlapping dual grid is exhibited [68] – [71].

IV.) Co – located Grid scheme

The co - located grid scheme is an approach, according to which, all variables of the flow are associated with the cell centre or with the grid point, with the same location, that is. This is valid both for conservative variables (ρ, ρu, ρv, ρw, ρE) and dependent variables (p, T, c, etc), as well.

V.) Staggered – Grid scheme

A pressure – based method with different storage location for the pressure and velocity components. The purpose of this scheme is to omit the oscillations exhibited on the scheme, which are created by central differencing.

Convective fluxes and their evaluation offer a wide range of choices, however, the flow variables are not directly available in the N_F faces. These values have to be

known a priori. In order for this situation to be resolved, either the flow variables or the fluxes have to be interpolated to the faces of the control volume, a process known as reconstruction and the solution arises through the values inside the control volumes.

There are two ways for an interpolation to be conducted:

I.) As in the central discretization schemes, the use of arithmetic averaging

II.) Apply a biased interpolation, something commonly encountered in upwind discretization schemes, which are connected to the flow equations characteristics

Gradients in EQ. 8, EQ. 15 and EQ. 25 (conservation of mass, momentum and energy equations) for velocity and temperature, are connected with the evaluation of the viscous fluxes at a face of a control volume, which has its basis on arithmetic averaging of the flow quantities. This very common methodology, is mostly applied in mixed grid cases.

3.6 Discretisation

3.6.1 Finite Volume Scheme for Unstructured Grids

The method of lines is applied by the majority of the numerical schemes, when resolving Navier – Stokes or Euller equations. Their advantage, in comparison to other methods, mostly lies in the wide variety of accuracy for spatial and temporal derivatives and a selection of different numerical approximations for them. The method of lines also includes some advantages in coupling methods.

The application of finite volume schemes, is inextricably connected to the physical domain in which the problem takes place and type, as well as the dimension of the grid applied to solve it. The subdivisions in which the physical domain of the problem is divided, as a whole, consist of the elements, meaning the grid cells. The grid cells tend to present a variation of shapes, mostly according to whether the grid will be a structured or an unstructured one, the solving method applied and the dimension in which the problem is solved.

A grid construction may not be relying solely in one shape of elements. For convenience or more analytical solution analysis reasons, multiple shapes of elements may be used. The aforementioned cases, where unstructured grids comprise of different cell types, are called “mixed grids”. An example of an unstructured, mixed grid can be observed in Fig. 35 [55].

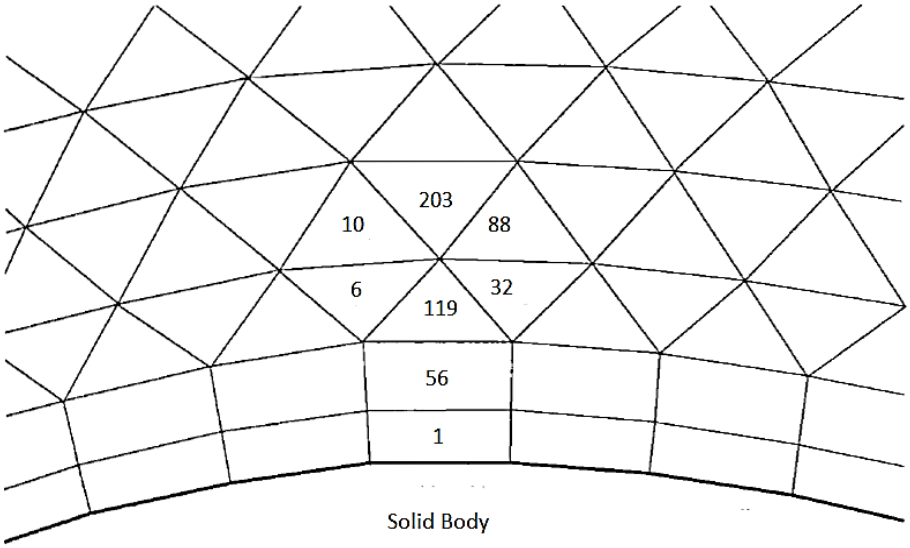

Fig. 35 : An unstructured, mixed grid. The numbers on the grid, depict the individual cells, according to Blazek [55]

A variety of rules apply, when constructing a grid, in order for the conservation properties of the equations to be maintained. Deriving from these guidelines, might ultimately cause the solution accuracy to be spoilt by numerical errors. The five basic rules that should be followed by virtue of that, are the following:

I.) Free space between the elements is not allowed.
II.) Deriving from the first rule, the whole domain must be covered entirely by grid.
III.) The elements of the grid should not overlap.
IV.) Smooth grid. Meaning, that the differences in volumes should not be large.
V.) The stretching ratio of adjacent grid elements and cells, should be as regular as possible.

The smaller volumes into which the entire domain is divided by the the computing grid construction (mesh) may be of various shapes. The most common of the geometric elements encountered (in three – dimensional cases), are the ones exhibited in Fig. 36.

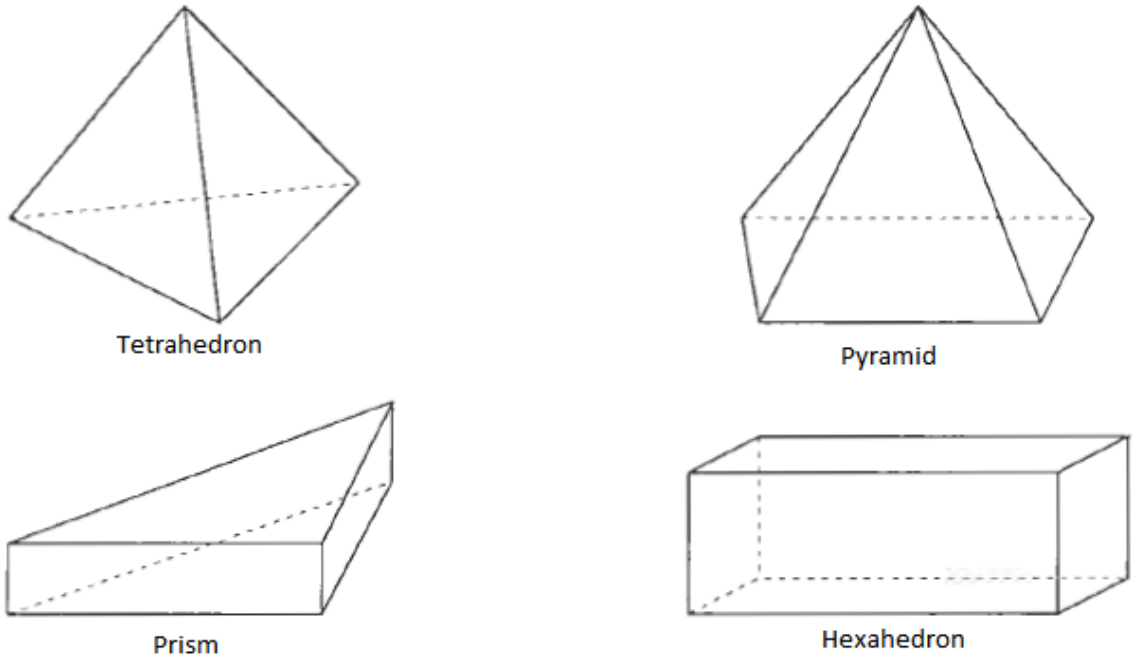

Fig. 36 : Elements a 3D computing grid might be composed of

Various definitions concerning control volume are used as well, when numerically solving governing equations that have been discretized. These definitions are connected to the location of the flow variables in a cell, with respect to the grid points. In respect to the flow variables and the grid cells, three strategies exist in the Finite volume scheme:

I.) Cell – Centered scheme

Flow variables are associated with the centroids of the grid cells and identical control volumes exist, in respect to the cells of the grid.

II.) Cell – vertex scheme with overlapping control volumes

Flow quantities and control volumes are assigned to the grid vertex. The definition of the control volumes, is the node all the neighbouring cells have in common. An overlap between the control volumes of two neighbouring vertices is observed.

It should be mentioned that this particular scheme is not used anymore.

III.) Cell – vertex scheme with median – dual control volumes

The grid vertices store the flow variables, but the connection of the control volumes takes place by connection of the centroids, edge midpoints and face elements of the surrounding cells. The control volumes comprise the grid points. As a result, a not overlapping dual grid is represented.

The shape of elements exhibited, depending on the dimension of the grid case, are the following:

2 – Dimension grids (2D): The shape of the elements is mostly triangles, however, quadrilaterals might be encountered in the grid elements.

3 – Dimension grids (3D): A wide variety of element shapes is exhibited in this case, ranging from tetrahedra to pyramids, prisms and occasionally hexadedra, depending on the value of the Reynolds number. The most encountered shape is tetrahedral.

3.6.2 Two – Dimensional Cases (2D)

(a) <u>Triangular elements</u>

In Fig. 37, a basic triangular and quadrilateral element for two – dimensional cases, can be observed, along with their numbering of nodes and face vectors.

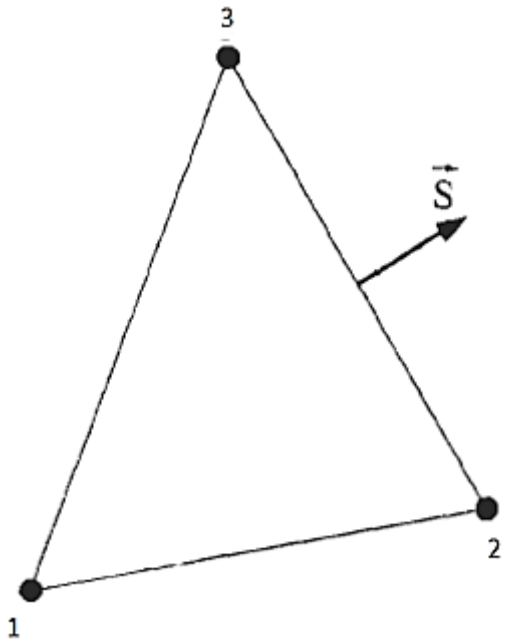

Fig. 37 : Triangular element used in a grid. The numbering of nodes and the scale vector ($\vec{S}$) can be observed.

In contrast to the 3D cases, where the solution for a flow in a plane is symmetric with respect to one coordinate direction (z – direction), in order for physical units to be obtained for pressure, volume, etc as well as because of the symmetry, there is a value describing the depth of all cells and control volumes. This specific value will be named as “b” and for reasons of convenience in 2D cases, this value is set to be equal to 1. The product of the area of a control volume with the depth (named as “b” in this case), equals its volume. Since the depth has a value of “1” for convenience, the area control volume, is the volume of a cell in 2D. In the following sections, an analysis of the elements exhibited in 2D unstructured grids, follows.

The formula of Gauss, is suitable for the calculation of the general area of a triangle and more specifically, if applied to the node numbering of the triangle in Fig. 35, the volume can be calculated. More specifically, the volume OMEGA will be:

$$\Omega = \frac{b}{2} [(x_1 - x_2) (y_1 - y_2) + (x_2 - x_3) (y_2 - y_3) + (x_3 - x_1) (y_3 - y_1)] \quad \textbf{EQ.53}$$

In order for a positive value to be obtained for the volume, the nodes must be numbered in a counter – clockwise order.

(b) <u>Quadrilateral elements</u>

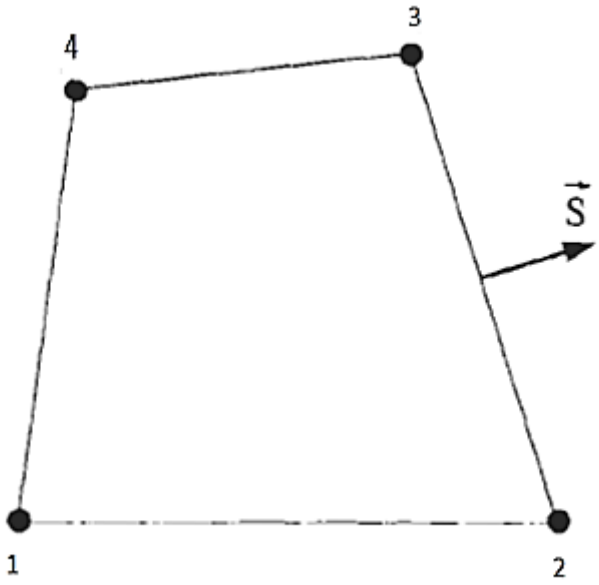

Fig. 38 : Quadrilateral element used in a grid. The numbering of nodes and the scale vector ($\vec{S}$) can be observed.

Again, after applying the Gauss formula into a general quadrilateral, with the nodes numbered according to Fig. 38, with a counter – clockwise manner, as well and performing some algebraic interventions, the final form for calculating the volume will be as in EQ.54. The presumption that the location of the control volume is in the x – y plane and that the symmetry axis is represented in the z – coordinate.

$$\Omega = \frac{b}{2} [(x_1 - x_3) (y_2 - y_4) + (x_4 - x_2) (y_1 - y_3)] \quad \textbf{EQ.54}$$

The unit normal vector along is constant along the straight lines in 2D. These straight lines provide the edges of the volume, as well. Upon integration of the fluxes, an evaluation must take place between ΔS (area of a face), the unit normal $\vec{n}$ and their product. The product of the aforementioned values, is the face vector $\vec{S}$.

The outward pointing face vector between points 2 – 3 for Fig. 36 can be calculated as:

$$\vec{S}_{23} = \vec{n}_{23} \cdot \Delta S_{23} = b \begin{bmatrix} y_3 - & y_2 \\ x_2 - & x_3 \end{bmatrix} \quad \textbf{EQ. 55}$$

with the unit normal vector obtained from EQ. 55 with

$$\Delta S = |\vec{S}| = \sqrt{S_x^2 + S_y^2} \quad \textbf{EQ. 56}$$

The z – component of the face vectors is omitted from EQ.55, because it is equal to zero, due to symmetry. For the same reason, the z- component of the unit normal vector is zero and omitted from EQ. 55, as well. S_x and S_y are the Cartesian components of the face vector.

3.6.3 Three – Dimensional Cases (3D)

One of the basic problems in Three – Dimensional (3D) geometries, is the greater lengths one will have to go to in order to calculate face vectors and volumes, especially in cases of elements or control volumes with quadrilateral faces. The four vertices of a quadrilateral face of a control volume may not be in the same plane, which causes the normal vector to be no longer constant and this is the main reason for the complexity of this specific geometry. A decomposition of each quadrilateral face into two or more triangles is a possible approach to resolve this difficulty.

It should be noted, though, that this method is mostly used for third – order and higher spatial discretisations, where its efficiency and robustness actually lie, rather than a second – order scheme on a smooth grid, as this would hardly make any difference in the accuracy and consequently, the total accuracy gain. A simplified process of the quadrilateral faces, based on the average normal vector, will be applied for triangular and quadrilateral faces.

(a) <u>Triangular faces</u>

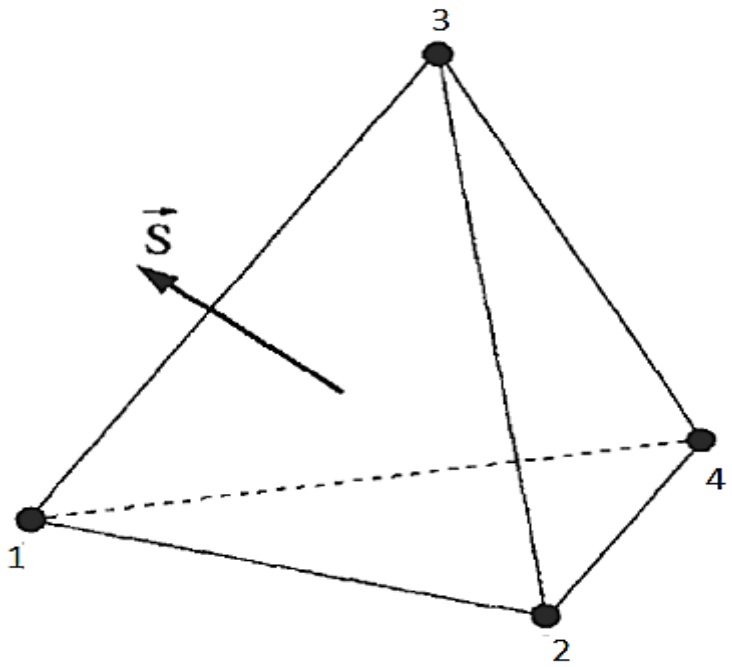

Fig. 39 : Face vector and numbering of nodes in a tetrahedral element

In the triangular face, the Gauss formula will be used to calculate the face vector $\vec{S}$. For the edge differences of the triangle 1 – 2 – 3 in Fig. 38 and according to how the nodes are defined, it is:

$\Delta xy_A = (x_1 - x_2)\,(y_1 + y_2)$

$\Delta xy_B = (x_2 - x_3)\,(y_2 + y_3)$

$\Delta xy_C = (x_3 - x_1)\,(y_3 + y_1)$

$\Delta yz_A = (y_1 - y_2)\,(z_1 + z_2)$

$\Delta yz_B = (y_2 - y_3)\,(z_2 + z_3)$

$\Delta yz_C = (y_3 - y_1)\,(z_3 + z_1)$

$\Delta zx_A = (z_1 - z_2)\,(x_1 + x_2)$

$\Delta zx_B = (z_2 - z_3)\,(x_2 + x_3)$

$\Delta zx_C = (z_3 - z_1)\,(x_3 + x_1)$

For the outward pointing face vector $\vec{S} = \vec{n} \cdot \Delta S$:

$$\vec{S} = \frac{1}{2}\begin{bmatrix} \Delta yz_A + & \Delta yz_B + & \Delta yz_C \\ \Delta zx_A + & \Delta zx_B + & \Delta zx_C \\ \Delta xy_A + & \Delta xy_B + & \Delta xy_C \end{bmatrix} \qquad \textbf{EQ. 57}$$

(a) <u>Quadrilateral faces</u>

In the case of a quadrilateral face and in order to calculate the average face vector $\vec{S}$, we will need to make use of the Gauss formula, much in a similar manner as in the quadrilateral two – dimension case. In Fig. 40, the face vector and the numbering of nodes in a hexahedral element, can be observed. The face that will be examined in this example, will be the upper – looking face from our point of view, which comprises of the nodes 5, 6, 7 and 8.

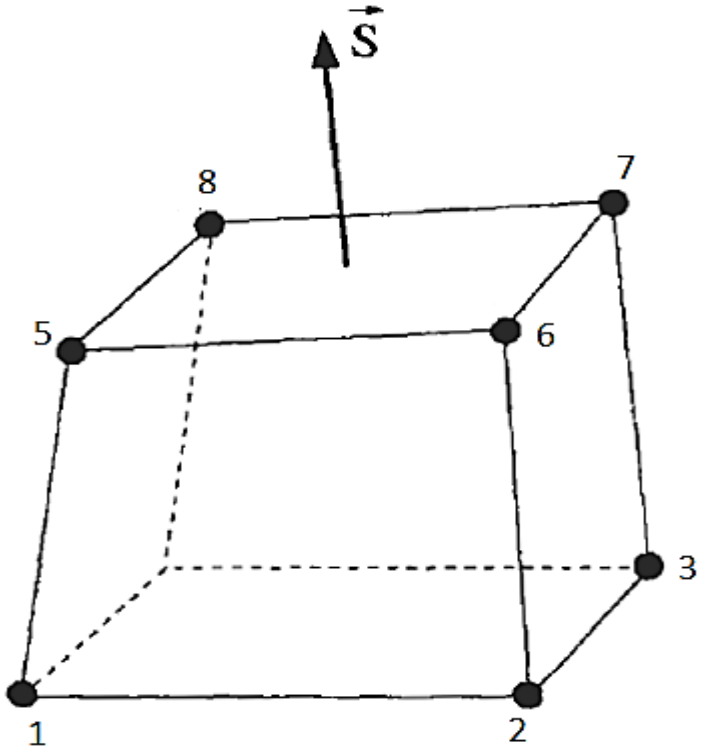

Fig. 40 : Face vector and numbering of nodes in a hexahedral element

The following differences will have to be defined:

$\Delta x_A = x_8 - x_6$

$\Delta x_B = x_7 - x_5$

$\Delta y_A = y_8 - y_6$

$\Delta y_B = y_7 - y_5$

$\Delta z_A = z_8 - z_6$

$\Delta z_B = z_7 - z_5$

The outward pointing face vector is defined as $\vec{S} = \vec{n} \cdot \Delta S$. From this relation :

$$\vec{S} = \frac{1}{2}\begin{bmatrix} \Delta y_A \Delta z_B - & \Delta z_A \Delta y_B \\ \Delta z_A \Delta x_B - & \Delta x_A \Delta z_B \\ \Delta x_A \Delta y_B - & \Delta y_A \Delta x_B \end{bmatrix} \quad \textbf{EQ. 58}$$

If the vertices of the face lie all in one plane and the shape approaches a parallelogram, there is an exact approximation. The unit normal vector can be obtained from

$$\vec{n} = \frac{\vec{S}}{\Delta S} \quad \textbf{EQ. 59}$$

with

$$\Delta S = \sqrt{S_x^2 + S_y^2 + S_z^2} \quad \textbf{EQ. 60}$$

Which is similar with the method used in the two – dimension case, with the addition of the extra dimension (z) Cartesian component of the face vector (S_Z).

3.6.4 Volume

According to Bruner [56] with a basis on the divergence theorem, there is an approach for the computation of volumes and Blazek [55] concluded with a formula directly applicable to unstructured grids. EQ. 61 is exact for a volume with triangular faces or a volume with planar quadrilateral faces.

$$\Omega = \frac{1}{3} \sum_{m=1}^{N_F} (\overrightarrow{r_{mid}} \cdot \vec{S})_m \quad \textbf{EQ. 61}$$

where

N_F -> The number of the faces of the control volume

$(\vec{r}_{mid})_m$ -> The midpoint of the control volume face m

$\vec{S}_m$ -> The outward directed face vector at face m

3.7 Turbulence Modelling

3.7.1 Overview of the Spalart – Allmaras Model

The Spalart – Allmaras turbulence model used in this study was initially designed for aerospace applications, specializing in wall – bounded flows. It is a one – equation model, solving a modeled transport equation for the kinematic viscosity (eddy viscosity), exhibiting good results for boundary layers subjected to adverse pressure gradients.

When applied in y+ ~ 1 grids and in its original form, the Spalart – Allmaras model is a low – Reynolds number model, requiring the proper resolvement of the viscosity – affected region of the boundary layer. A different sort of wall treatment has been applied to this model in the FLUENT simulations [73], as it is extended with a y+ - insensitive wall treatment, called "Enhanced Wall Treatment" (EWT). The aforementioned treatment allows the model to be applied, regardless of the near wall y+ resolution and a blending (based on y+) of the formulation from viscous sublayer formulation to a logarithmic formulation, takes place.

For the rest of the grid cases used in this study (y+5 and y+15 grids), the formulation remains intact, providing consistent wall shear stress and heat transfer coefficients. A minimum resolution of 10 – 15 cells for the boundary layer (prism layer) should be insured for the boundary layer, despite the removal of the y+ sensitivity. Table (a) exhibits the prism layer resolution in the grids applied for the 3D cases and how the grid construction satisfies the minimum boundary layer resolution condition. It is clear, that as the y+ number is smaller, the dS factor (1st cell distance from the boundary layer) decreases as well and under the constraints set for a finite total height for the boundary layer (~0.65 – 0.68), the number of layers is growing, in order to reach this aforementioned height.

	y+1 (dS =0.00095)	y+5 (dS =0.00475)	y+15 (dS =0.01427)
30^o Slant Angle	30	20	14
25^o Slant Angle	30	20	14
35^o Slant Angle	30	20	14

Table (a) : Boundary (prism) layer resolution in the 3D cases grids

The Spalart – Allmaras model is not calibrated for general industrial flows, as it was developed for aerodynamic flows. As a result of that, errors are produced for cases such as round jet and plane flows, involving free shear flows. The decay of homogeneous and isotropic turbulence is hard to be predicted as well with this model.

3.7.2 Transport Equation for the Spalart – Allmaras Model

With an exception in the near – wall viscosity affected region, the turbulent kinematic viscosity in the Spalart – Allmaras model is identical to the transported variable $\tilde{\nu}$. EQ. 62 exhibits the transport equation for $\tilde{\nu}$:

$$\frac{\partial}{\partial t}(\rho\,\tilde{\nu}) + \frac{\partial}{\partial x_i}(\rho\,\tilde{\nu}\,u_i) =$$

$$G_v + \frac{1}{\sigma_{\tilde{\nu}}}\left[\frac{\partial}{\partial x_i}\left\{(\mu + \rho\,\tilde{\nu})\,\frac{\partial \tilde{\nu}}{\partial x_j}\right\} + C_{b2}\rho\,(\frac{\partial \tilde{\nu}}{\partial x_j})^2\right] - Y_v + S_{\tilde{\nu}} \qquad \textbf{EQ.62}$$

where

G_v -> Production of turbulent viscosity

Y_v -> Destruction of turbulent viscosity (occurring in the near wall region due to wall blocking and damping)

v -> Molecular kinematic viscosity

$S_{\tilde{\nu}}$ -> Source term

$\sigma_{\tilde{\nu}}$, C_{b2} -> Constants

3.7.3 Modeling the Turbulent Viscosity & the Turbulent Production

EQ. 63 models the turbulent viscosity (μ_t):

$$\mu_t = \rho\,\tilde{\nu}\,f_{v1} \qquad \textbf{EQ. 63}$$

where

f_{v1} -> Viscous damping

Viscous damping is given by EQ. 64:

$$f_{v1} = \frac{\chi^3}{\chi^3 + C_{v1}^3} \qquad \textbf{EQ. 64}$$

where

χ -> $\frac{\tilde{\nu}}{\nu}$

The production term G_ν is defined as following

$$G_\nu = C_{b1}\,\rho\,\tilde{S}_{\tilde{\nu}} \qquad \textbf{EQ. 65}$$

where

$$\tilde{S} = S + \frac{\tilde{\nu}}{\kappa^2\,d^2}\,f_{\nu 2} \qquad \textbf{EQ. 66}$$

and consequently for $f_{\nu 2}$:

$$f_{\nu 2} = 1 - \frac{\chi}{1+\chi\,f_{\nu 1}} \qquad \textbf{EQ.67}$$

where (in EQ. 65 – 67)

C_{b1} , κ -> Constants

d -> Distance from the wall

S -> Scalar measure of the deformation tensor

In the ANSYS FLUENT version used for the simulations, the scalar measure of the deformation tensor is by default based on the magnitude of vorticity, as in the original model proposed by Spalart – Allmaras [73].

EQ. 68 exhibits the scalar measure of the deformation tensor used in the FLUENT simulations

$$S = \sqrt{2\,\Omega_{ij}\,\Omega_{ij}} \qquad \textbf{EQ.68}$$

where

Ω_{ij} -> Mean rate of rotation tensor

The mean rate of rotation tensor is defined from EQ. 69:

$$\Omega_{ij} = \frac{1}{2}\left(\frac{\partial u_i}{\partial x_j} - \frac{\partial u_j}{\partial x_i}\right) \qquad \textbf{EQ. 69}$$

Shear flows, vorticity and strain rate are identical and this is the main reason for the existing expression of S. In flow regions, such as stagnation lines, which are inviscid and turbulence production due to strain rate can be unphysical, vorticity has a zero value. The strain / vorticity based modification used in the FLUENT simulations, derives from an alternate formulation, which combines the measures of both vorticity and the strain tensors in the definition of the scalar measure of the deformation tensor (S). EQ. 70, exhibits the aforementioned modification:

$$S = |\Omega_{ij}| + C_{prod} \min(0, |S_{ij}| - |\Omega_{ij}|) \quad \textbf{EQ. 70}$$

where

$C_{prod} = 2.0$

$$|\Omega_{ij}| = \sqrt{2\,\Omega_{ij}\,\Omega_{ij}} \quad \textbf{EQ. 71}$$

$$|S_{ij}| = \sqrt{2\,S_{ij}\,S_{ij}} \quad \textbf{EQ. 72}$$

$$S_{ij} = \frac{1}{2}\left(\frac{\partial u_j}{\partial x_i} - \frac{\partial u_i}{\partial x_j}\right) \quad \textbf{EQ. 73}$$

In areas where the strain rate measure is exceeded by the rate of vorticity, the production of eddy viscosity and consequently eddy viscosity itself can be reduced by including the rotation and strain tensors, as well. A good example of this case is vortical flows, especially in a small distance from the core of the vortex where turbulence is suppressed and the flow is subjected to a pure rotation. By including both the rotation and strain tensors the effects of rotation on turbulence can be more accurately exhibited.

However, as stated in the FLUENT Theory Guide, by keeping the default options, the returning results from this software tend to overpredict the production of eddy viscosity. As a rconsequence to that, an overprediction of eddy viscosity inside vortices, takes place.

3.7.4 Modeling the Turbulent Destruction

EQ. 74, describes the destruction term:

$$Y_v = C_{w1}\,\rho\,f_w\,\left(\frac{\tilde{\nu}}{d}\right)^2 \quad \textbf{EQ. 74}$$

where

$$f_w = g\left[\frac{1+C_{w3}^6}{g^6+C_{w3}^6}\right]^{\frac{1}{6}} \quad \textbf{EQ. 75}$$

$$g = r + C_{w2}\,(r^6 - r) \quad \textbf{EQ. 76}$$

$$r \equiv \frac{\tilde{\nu}}{\tilde{S}\,\kappa^2\,d^2} \qquad \textbf{EQ. 77}$$

where

C_{w1} , C_{w2} , C_{w3} -> Constants

$\tilde{S}$ = S + $\frac{\tilde{\nu}}{\kappa^2\,d^2} f_{v2}$ (as in EQ. 66)

The model constants for FLUENT were the following (by default):

C_{b1} = 0.1355, C_{b2} = 0.622

$\sigma_{\tilde{\nu}}$ = $\frac{2}{3}$, C_{v1} = 7.1

C_{w1} = $\frac{C_{b1}}{\kappa^2} + \frac{(1+ C_{b2})}{\sigma_{\tilde{\nu}}}$

C_{w2} = 0.3

C_{w3} = 2.0

κ = 0.4187 (Von Karman constant)

3.7.5 Wall Boundary Conditions

The extension of the Spalart – Allmaras model with an insensitive wall treatment mentioned in Chapter 3.7.1 as EWT (Enhanced Wall Treatment), blends all solution variables from their viscous sublayer formulation (EQ. 78)

$$\frac{u}{u_t} = \frac{\rho\,u_t\,y}{\mu} \qquad \textbf{EQ. 78}$$

the solution variables are blended, depending on y+, to their corresponding logarithmic layer values, as in EQ. 79:

$$\frac{u}{u_t} = \frac{1}{\kappa} \ln E \left(\frac{\rho\,u_t\,y}{\mu}\right) \qquad \textbf{EQ. 79}$$

where

u -> Velocity parallel to the wall

u_t -> Shear velocity

y -> distance from the wall

κ -> Von Karmann constant (0.4187)

Through the aforementioned blending of solution variables, a 1 ≤ y+ ≤ 30 range of y+ values in the buffer layer, is covered as well.

3.7.6 Modeling of Convective Heat and Mass Transfer (Energy Equation)

In the simulations in which the Spalart – Allmaras model was applied, the Reynolds analogy to turbulent momentum transfer concept was applied to model turbulent heat transport. The Energy equation solved in these simulations was modeled as in EQ. 80:

$$\frac{\partial}{\partial t}(\rho E) + \frac{\partial}{\partial x_i}\left[u_i\,(\rho E + p)\right] =$$

$$\frac{\partial}{\partial x_j}\left[\left(k + \frac{C_p\,\mu_t}{P_{rt}}\right)\frac{\partial T}{\partial x_j} + u_i\,(\tau_{ij})_{eff}\right] + S_h \qquad \textbf{EQ. 80}$$

where

k -> Thermal conductivity

E -> Total Energy

$(\tau_{ij})_{eff}$ -> Deviatoric stress tensor

The deviatoric stress tensor is defined as in EQ. 81:

$$(\tau_{ij})_{eff} = \mu_{eff} + \left(\frac{\partial u_j}{\partial x_i} + \frac{\partial u_i}{\partial x_j}\right) - \frac{2}{3}\,\mu_{eff}\,\frac{\partial u_k}{\partial x_k}\,\delta_{ij} \qquad \textbf{EQ.81}$$

Chapter 4 : Results for 2D Simulations

The main purpose for examining the Ahmed body geometry in a 2D scheme, was to exhibit its basic flow phenomena and features and how these are developed in an environment in which resolving the problem and achievement of numerical convergence is easier, as well. In order to obtain data about the behavior of the flow around the Ahmed body, three different Riemann solvers were applied (the ROE – Riemann solver [78] in FLUENT and the Rusanov [78] and HLLC [78] in UCNS3D) with ranging numerical dissipation properties. The 2D simulations also put in good test the various grid formations used for different y+ values, exhibiting crucial differences in the results obtained between a fine, a medium and a coarse grid, in a compilation of cases, coupled with the aforementioned solvers. However, neglecting the 3D nature of the problem in the first place, automatically means compromising the results in these cases. These results might be misleading or other discrepancies might be exhibited, rendering the 2D simulations suitable only as a basic case study.

4.1 Initial Conditions

The initial conditions set for this study were decided and based upon the initial conditions encountered in the bibliography. The selection was made mostly in terms of the frequency these values were encountered, as this offers, both ample of previous experimental and/or computational data as well as providing the chance to improve the already extracted data, by virtue of using the inhouse developed code.

The freestream velocity of the air was defined at 40 m/s, with a Reynolds number of Re = 2.8 x 10^6. The initial conditions used by Ahmed et al. [2],[3] were 32 m/s for the freestream velocity and a Reynolds number of 4.3 x 10^6. The outflow gauge pressure was equal to Pa = 100000

4.2 Domain Size

The size of the external domain used for all three of the Ahmed body slant angles, was a rectangular of [700 , 200]cm^2 dimension. The boundary conditions of the domains were characterized as “Inflow” for the left – hand vertical, “Outflow” for the right – hand vertical side and as “Symmetry” for the upper and lower horizontal sides.

The full dimension of the external domains in comparison to the Ahmed body, can be seen in Fig. 41 for a 30^o slant angle and a $y^+ = 1$:

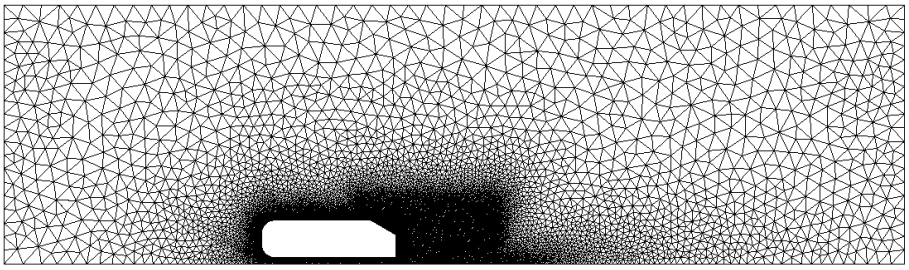

Fig. 41 : External *[700 , 200]*^{2} dimension domain for Ahmed body with a slant angle of *30*^{o} and a $y^+ = 1$

In Fig. 42, the external domain for y^+=1, in comparison with the Ahmed body for the 25^o (Subcritical) slant angle can be observed:

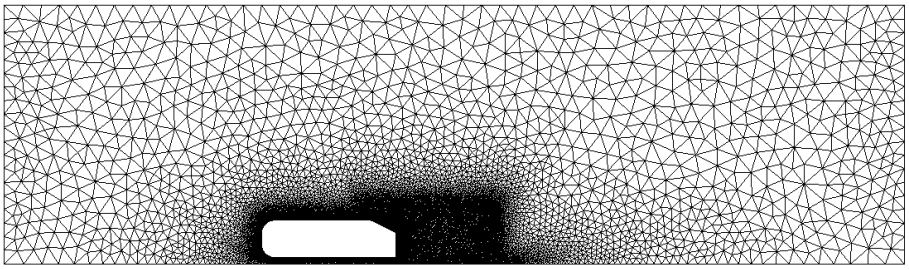

Fig. 42 : External *[700 , 200]*^{2} dimension domain for Ahmed body with a subcritical slant angle of *25*^{o} and a $y^+ = 1$

Finally, the outer domain for the Supercritical slant angle of 35^o and y^+=1 is exhibited in Fig. 43:

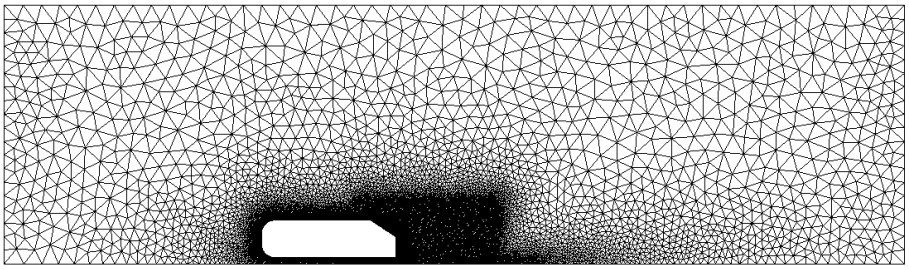

Fig. 43 : External *[700 , 200]*^{2} dimension domain for Ahmed body with a supercritical slant angle of *35*^{o} and a $y^+ = 1$

4.3 Grid Details

For each slant angle (30^o, 25^o, 35^o) three different types of grids with different y^+ factors ($y^+ = 1$, $y^+ = 5$ and $y^+ = 15$), were created. The aforementioned configuration, aimed mostly in exhibiting the fluctuations in the flow features around the Ahmed body for different approximation of the flow, in connection with the boundary layers. The optimum number of cells for the study can theoretically be stretched to infinite, however due to the grid creation and processing taking place in everyday computers, there were certain limitations concerning the amount of computational budget available (mostly involving the available amounts of RAM) leading to the particular choice of number of cells for optimum simulation environment within the computational budget available. In order to achieve maximum efficiency in capturing all of the flow features around the Ahmed body, extra – detailed domains were applied in the corresponding areas (between the bluff body and especially in the slant angle – wake section to capture the turbulence effects). In Tables 1 – 3, analytical information about the composites of every grid configuration used in this study, can be observed:

30^o Slant Angle	Total Nodes	Total Elements (Cells)	Rectangular Elements (Structured)	Triangular Elements (Unstructured)
y^+ 1 (Fine)	123742	168198	71160	97038
y^+ 5 (Medium)	36430	55136	14696	40440
y^+ 15 (Coarse)	14510	23590	3870	19720

Table 1: Statistics for 2D grid created for the 30^o slant angle

25^o Slant Angle	Total Nodes	Total Elements (Cells)	Rectangular Elements (Structured)	Triangular Elements (Unstructured)
y^+ 1 (Fine)	123764	164933	73290	91643
y^+ 5 (Medium)	36783	55410	14806	40604
y^+ 15 (Coarse)	16874	27929	3870	24059

Table 2: Statistics for 2D grid created for the 25^o (subcritical) slant angle

35^{o} Slant Angle	Total Nodes	Total Elements (Cells)	Rectangular Elements (Structured)	Triangular Elements (Unstructured)
y^{+} 1 (Fine)	125832	168699	73290	95904
y^{+} 5 (Medium)	30317	43824	13460	30364
y^{+} 15 (Coarse)	17508	29329	3870	25459

Table 3: Statistics for 2D grid created for the 35^{o} (supercritical) slant angle

Each y^{+} factor, represents a difference in the quality of the grid and as a consequence of the expecting results. y^{+} can be described as a dimensionless wall distance for a wall bounded flow, defined by EQ. 82:

$$y^{+} = \frac{u_{*} \cdot y}{v} \qquad \textbf{EQ. 82}$$

where

u_{*} -> friction velocity in the nearest wall

y -> distance to the nearest wall

v -> local kinematic viscosity

By EQ. 82, the following discrimination can be made in this particular study:

$y^{+} = 1$ -> Fine grid

$y^{+} = 5$ -> Medium grid

$y^{+} = 15$ -> Coarse grid

4.3.1 Ahmed Body 30^{o} Slant Angle

The close up screenshots of Fig. 44 – 46, exhibits the grid closer to the Ahmed body and the 30^{o} angle with detail, for different y^{+} factors. The hybrid mesh created through hyperbolic extension and used for smoother transition of the flow from the boundary conditions to the domain, can be observed. y^{+} factors, were respectively equal to y^{+} = 1 (Fig. 44), y^{+} = 5 (Fig 45) and y^{+} = 15 (Fig. 46).

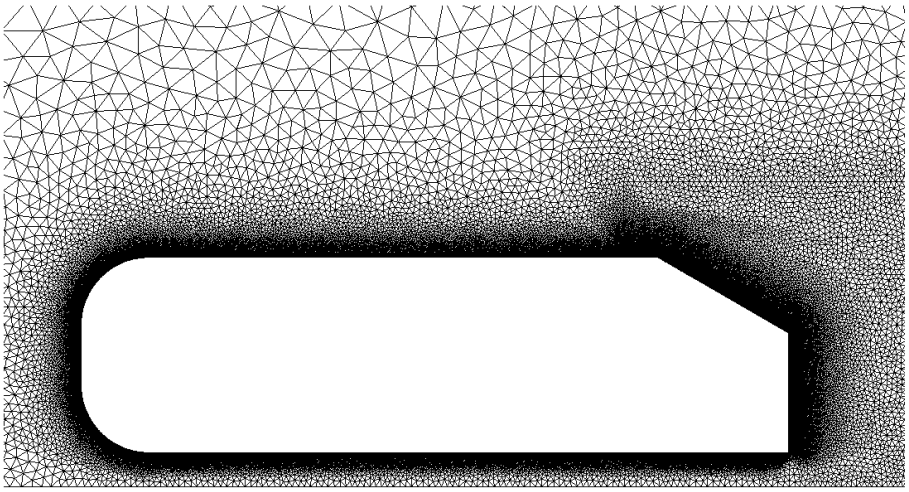

Fig. 44 : Close up screenshot of the Ahmed body for a *30^{o}* slant angle and a *y^{+} = 1*

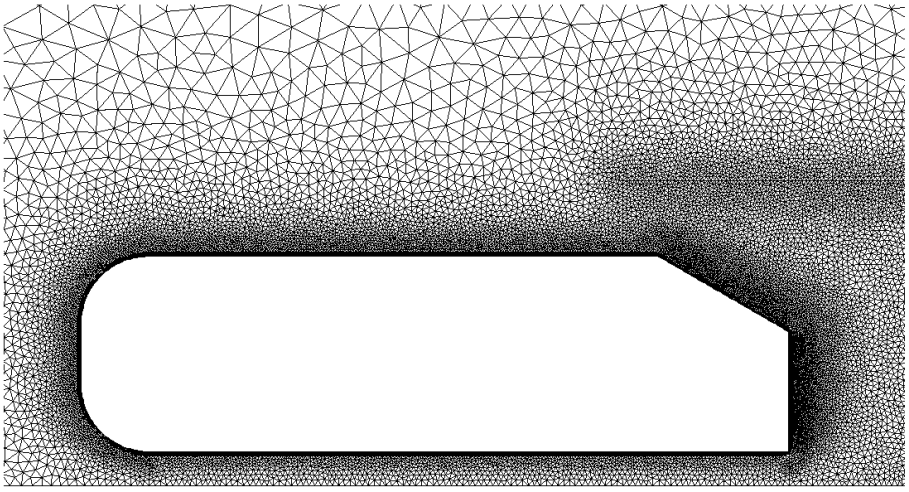

Fig. 45 : Close up screenshot of the Ahmed body for a *30^{o}* slant angle and a *y^{+} = 5*

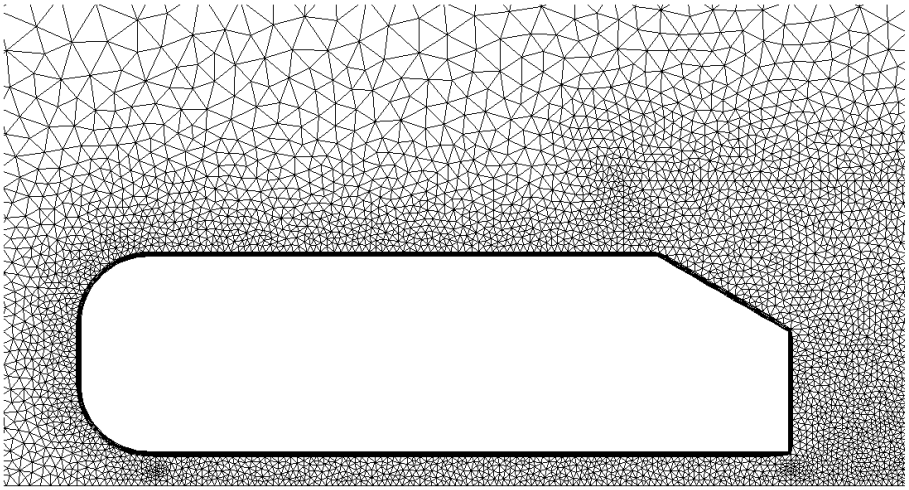

Fig. 46 : Close up screenshot of the Ahmed body for a 30^o slant angle and a $y^+ = 15$

The difference in the grid created, occurring for different y^+ factors, can be closely seen in Fig. 47 – 49, which focus on the slant angle and how the hybrid (structured and unstructured) meshing, forms around it:

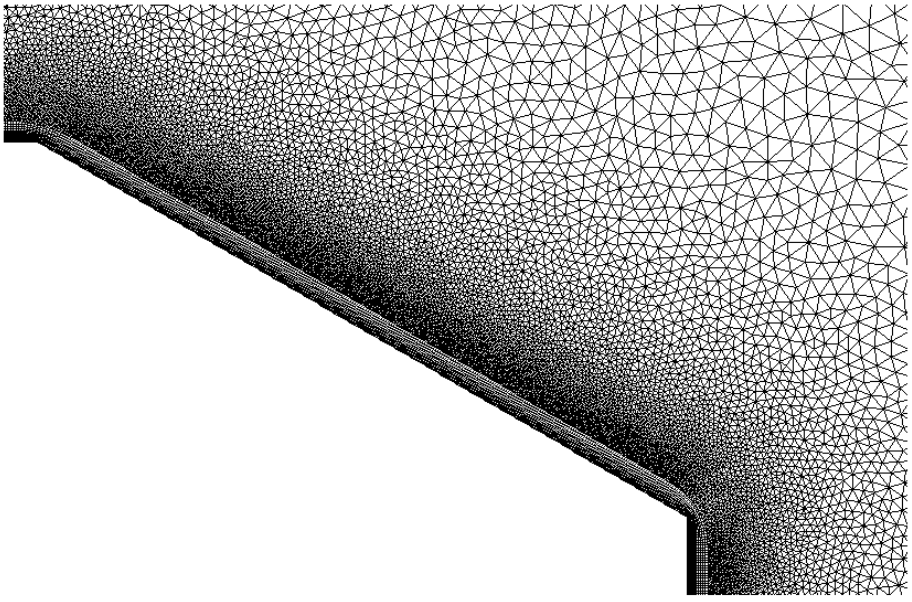

Fig. 47 : Close up screenshot of the hybrid mesh for the Ahmed body 30^o slant angle with a $y^+ = 1$

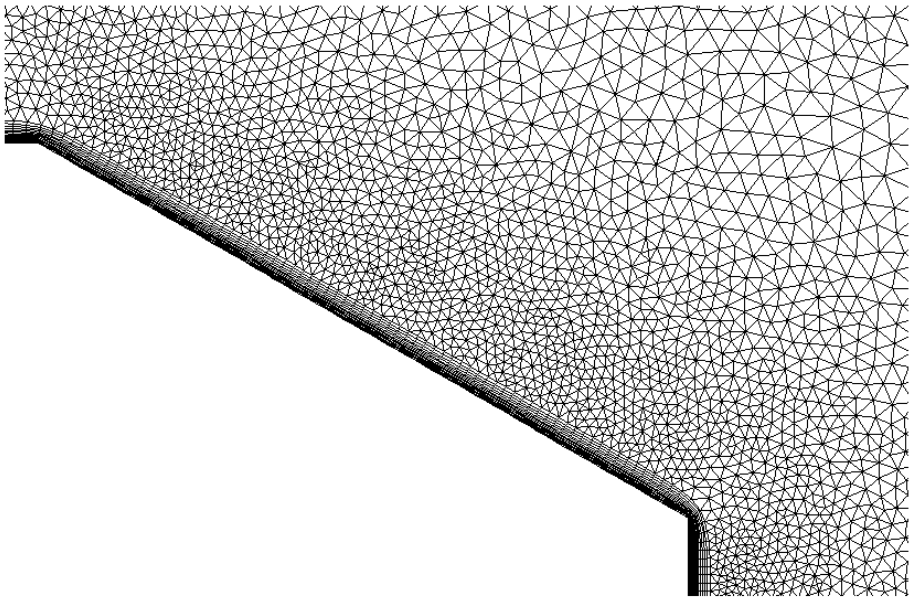

Fig. 48 : Close up screenshot of the hybrid mesh for the Ahmed body 30^o slant angle with a $y^+ = 5$

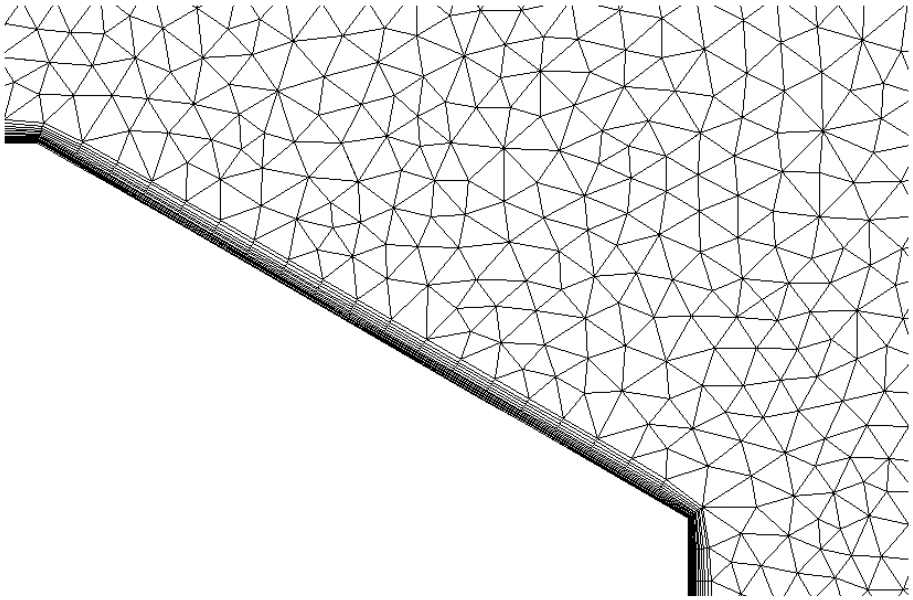

Fig. 49 : Close up screenshot of the hybrid mesh for the Ahmed body 30^o slant angle with a $y^+ = 15$

The difference in the qualities of the structured and unstructured mesh forming around both ends of the slant angles, according to the fluctuation of the y^+ factor (the greater the y^+, the fewer the points), is apparent and is of great difference in the calculations taking place between the three grids examined, something that will be exhibited in the forthcoming pages.

4.3.2 Ahmed Body 25^o Slant Angle

Fig. 50 – 52 exhibit the forming of the hybrid mesh around the Ahmed body for the 25^o (subcritical) slant angle. As in the case of 30^o and by virtue of improving transition of flow from the boundary layer to the domain, mesh was created with hyperbolic extrusion, with certain smoothing parameters used. More precisely, in the 25^o case, the volume factors enabled were equal to 0.00001.

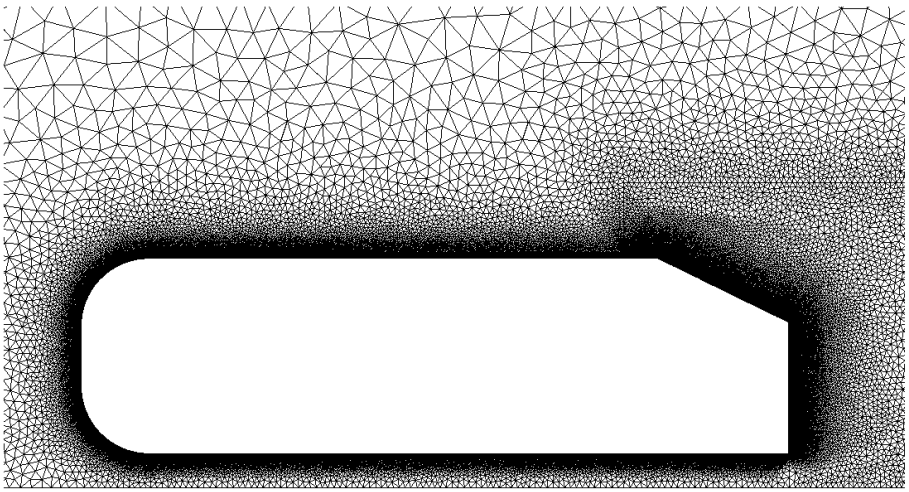

Fig. 50 : Close up screenshot of the Ahmed body for a 25^o slant angle with a $y^+ = 1$

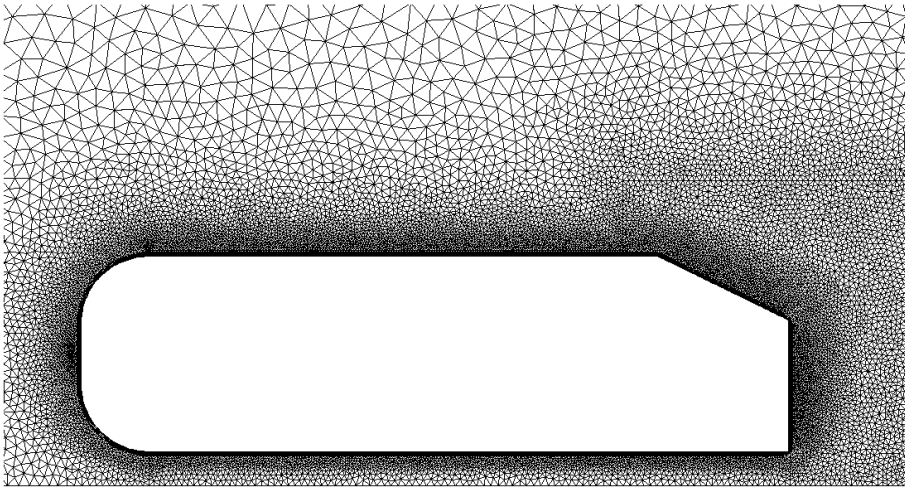

Fig. 51 : Close up screenshot of the Ahmed body for a 25^o slant angle with a $y^+ = 5$

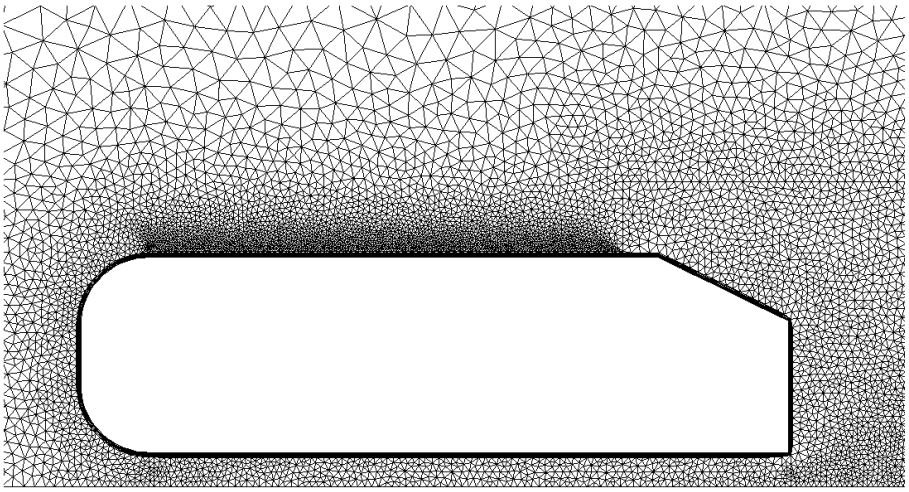

Fig. 52 : Close up screenshot of the Ahmed body for a 25^o slant angle with a $y^+ = 15$

As in the 30^o case, the (apparent) differences in the hybrid meshing and clustering of points and cells along the slant angle and in the wake line, where most of the flow features take place, tend to present a variation in the results of the simulations according to the fluctuation of y^+. In Fig. 53 – 55, these differences are exhibited for $y^+ = 1$, $y^+ = 5$ and $y^+ = 15$, respectively:

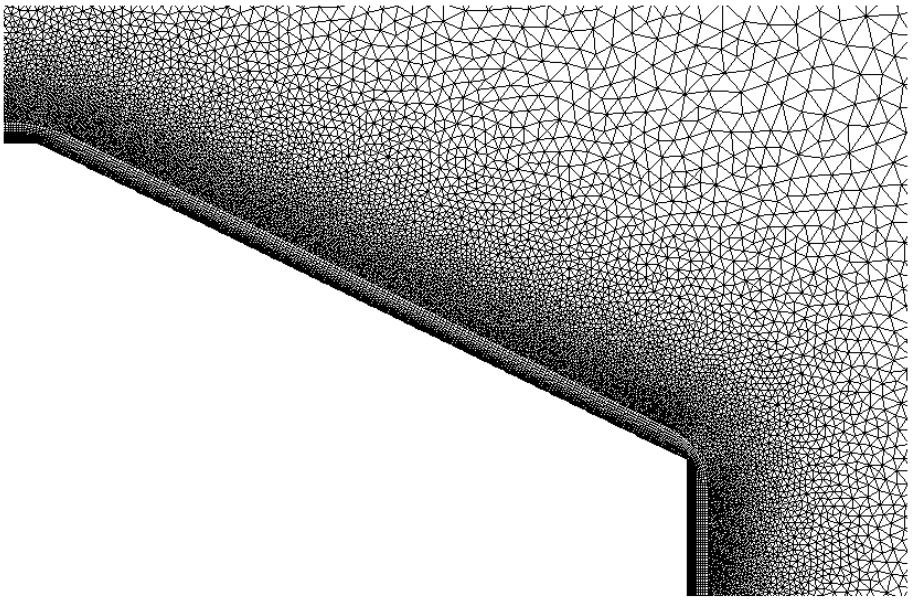

Fig. 53 : Close up screenshot of the hybrid mesh for the Ahmed body 25^o slant angle with a $y^+ = 1$

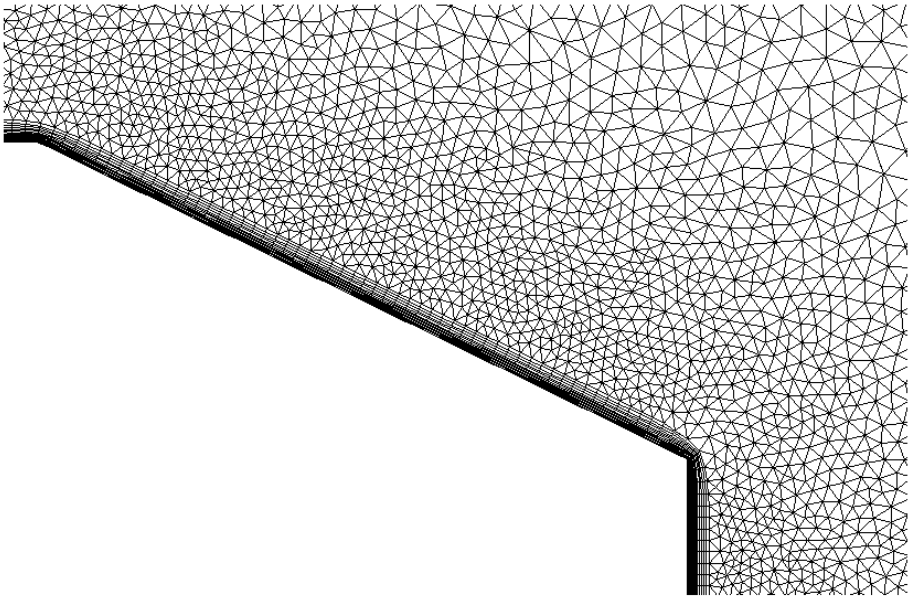

Fig. 54 : Close up screenshot of the hybrid mesh for the Ahmed body 25^o slant angle with a $y^+ = 5$

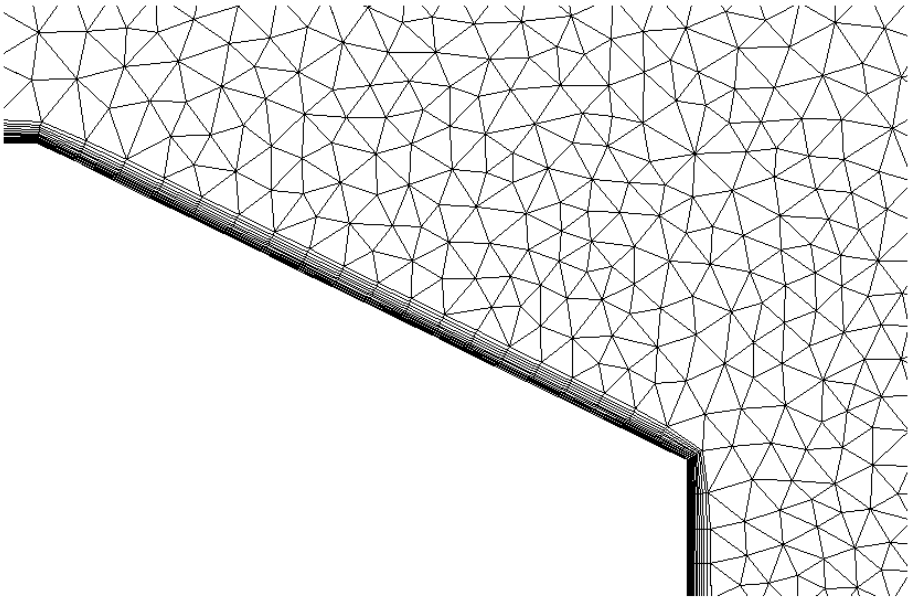

Fig. 55 : Close up screenshot of the hybrid mesh for the Ahmed body *25^{o}* slant angle with a *y^{+} = 15*

It becomes apparent, that as the y^{+} factor raises, there is a (not analogical) growth of the distance from the center of the first cell, to the wall. This fact, consequently, proves the claim expressed in the beginning of the chapter, stating that the bigger the y^{+} factor number, the coarser the grid becomes. This mostly derives, from the fact that with bigger distance of the cell centre from the wall and more scarcely placed points along a connector, a cell covers a bigger area in which many flow effects may take place and as a consequence of that, they might not be depicted appropriately in a simulation, something which could ultimately lead to misleading or even false conclusions about the flow topology and behavior.

4.3.3 Ahmed Body 35^{o} Slant Angle

The hybrid mesh created and used in the simulations of this study for the Ahmed body with a 35^{o} (supercritical) slant angle, is exhibited in Fig. 56 – 58 for y^{+} factors of y^{+} = 1, y^{+} = 5 and y^{+} = 15, respectively in close – up screenshots. In order to improve the mesh quality and cluster the elements in the area where the flow topology exhibits features that are of interest to this study for this case, as well as the other two cases of 30^{o} and 25^{o}, a boundary decay between 0.95 – 0.96 was imposed for the aforementioned domains. All domains in the slant angle have a boundary decay of 0.99 and were initialized and refined according to this parameter for the best possible resolution of the flow phenomena.

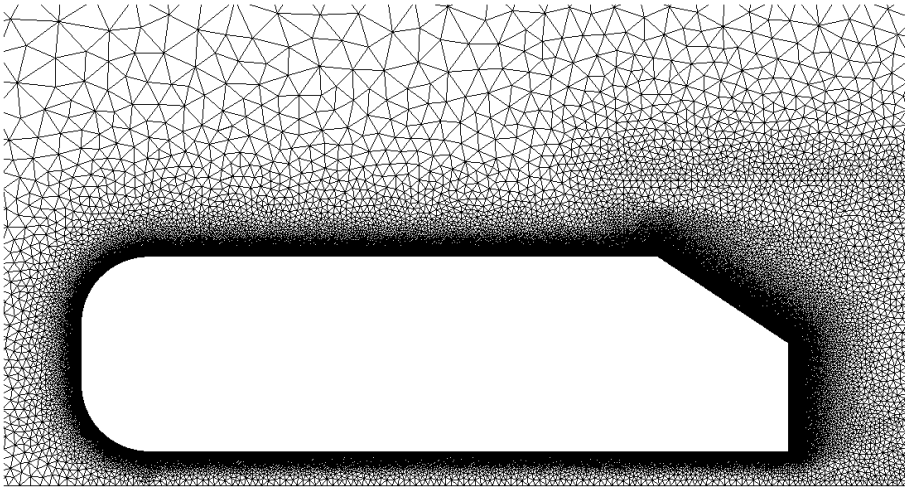

Fig. 56 : Close up screenshot of the Ahmed body for a 35^{o} slant angle with a $y^{+} = 1$

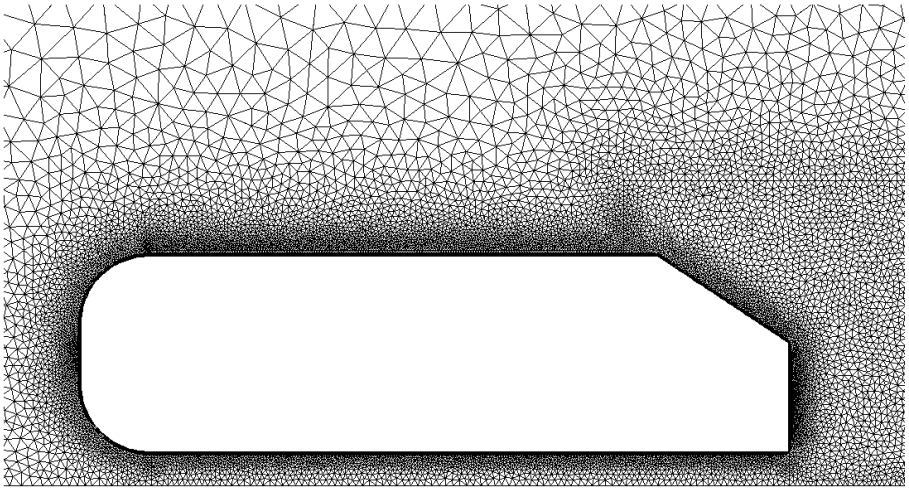

Fig. 57 : Close up screenshot of the Ahmed body for a 35^{o} slant angle with a $y^{+} = 5$

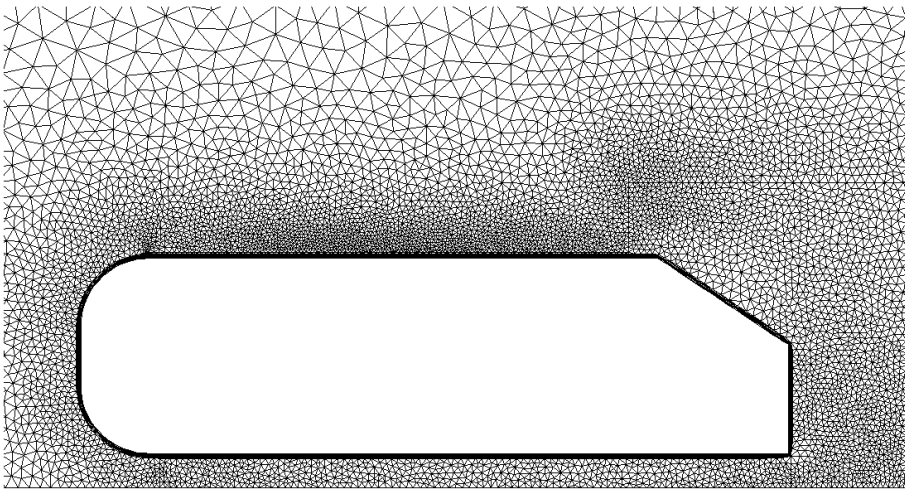

Fig. 58 : Close up screenshot of the Ahmed body for a 35^o slant angle with a $y^+ = 15$

Fig. 59 – 61 comprise of closer views to the supercritical 35^o angle and how the hybrid mesh is affected, through different y^+ numbers. As in the previous slant angle cases, , as the y^+ factor rises, the different spacing (dimension) of the connectors and the wall distance is apparent, leading to coarser grids.

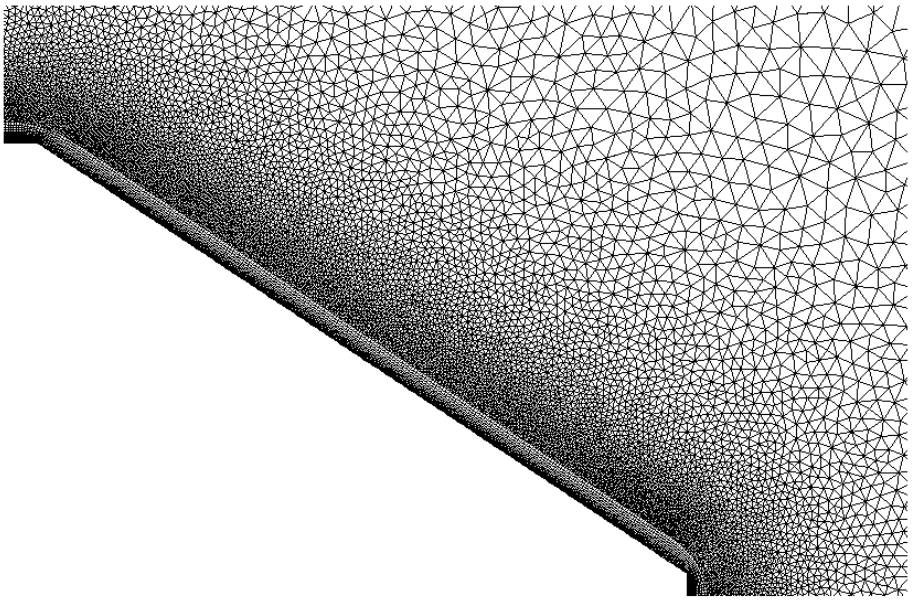

Fig. 59 : Close up screenshot of the hybrid mesh for the Ahmed body 35^o slant angle with a $y^+ = 1$

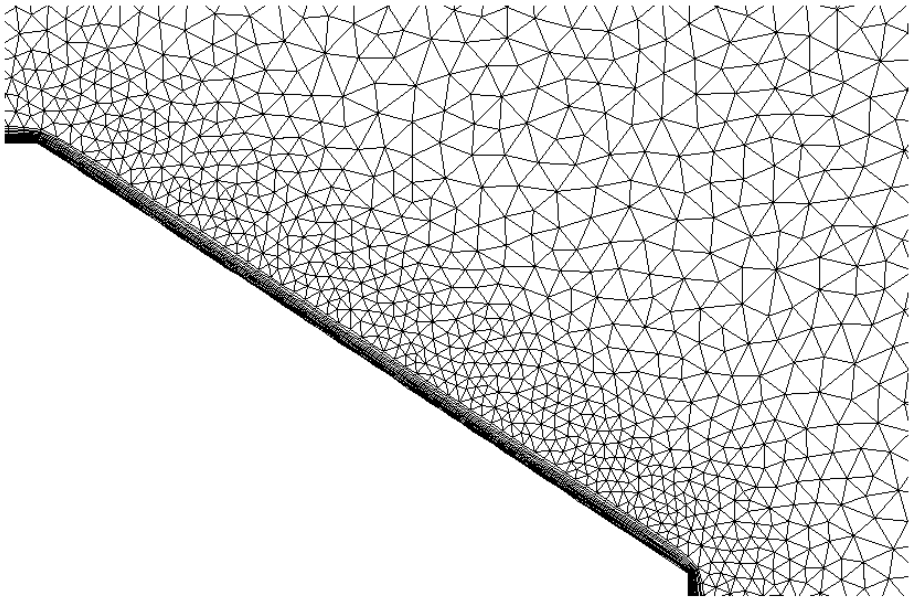

Fig. 60 : Close up screenshot of the hybrid mesh for the Ahmed body 35^o slant angle with a $y^+ = 5$

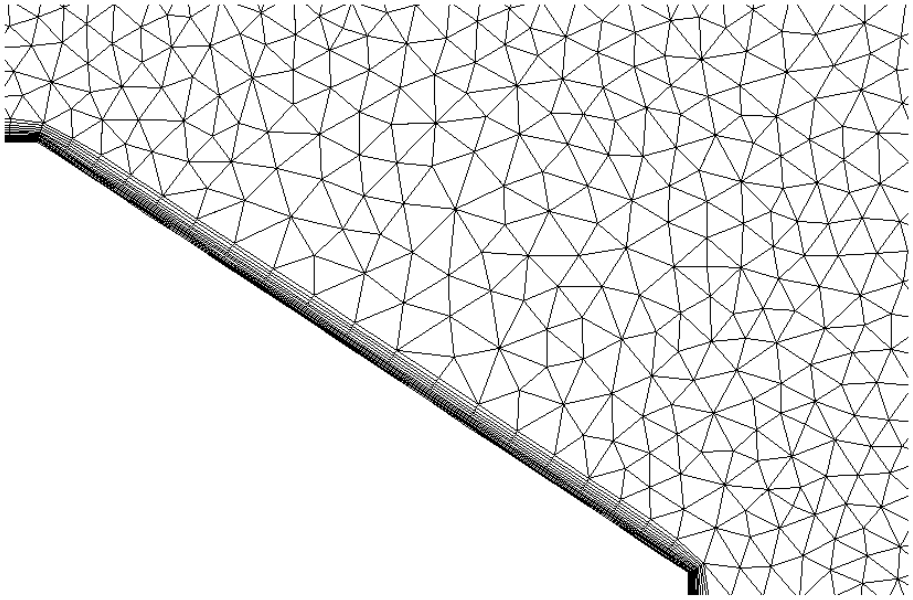

Fig. 61 : Close up screenshot of the hybrid mesh for the Ahmed body 35^o slant angle with a $y^+ = 15$

Despite being created with the same characteristics and parameters as the previous grids, the differences in the hybrid mesh between the three y^+ factors examined in the 35^o slant angle, are not so obvious as in the previous two (30^o, 25^o) slant angles examined.

After thorough and insightful creation of the grids used in the simulations of this study, in the interest of gaining the best possible results, it has to be noted that none of the aforementioned grids exhibited, exceeded the maximum cell skewness of 0.98. However, due to various computational cost limitations and the wide use of commercial workstations for creating the grids and running test simulations both on FLUENT and the Inhouse developed code, the elements had to be kept into a number, that would however assure the best solution possible, in accordance to a logical computational cost.

Concerning the method of hyperbolic extrusion used for creating the unstructured part of the grid surrounding the walls of the Ahmed body, details can be found in Tables 4, 5 and 6 about the methods and the Δs used, for every angle of the Ahmed body. The Δs used for the steps of the extrusion of the structured grid, were extracted according to the Reynolds number used in the study ($Re = 2.8 \times 10^6$), the Reference length of the body (1044 mm) and the y^+ wall distance used for every case.

<u>30^o slant angle</u>

	$y^+ = 1$	$y^+ = 5$	$y^+ = 15$
Initial Δs	0.00095	0.00475	0.01472
Growth Rate	1.17	1.15	1.15
Smoothing parameters (Volume)	0.00001	0.00001	0.00001
Steps	30	22	15

Table 4 : Structured grid extrusion details for the 30^o slant angle

25° slant angle

	$y^+ = 1$	$y^+ = 5$	$y^+ = 15$
Initial Δs	0.00095	0.00475	0.01472
Growth Rate	1.17	1.15	1.15
Smoothing parameters (Volume)	0.00001	0.00001	0.00001
Steps	30	22	15

Table 5 : Structured grid extrusion details for the 25° angle

35° slant angle

	$y^+ = 1$	$y^+ = 5$	$y^+ = 15$
Initial Δs	0.00095	0.00475	0.01472
Growth Rate	1.17	1.15	1.15
Smoothing parameters (Volume)	0.00001	0.00001	0.00001
Steps	30	20	15

Table 6 : Structured grid extrusion details for the 35° angle

In Tables 7, 8 and 9, the minimum orthogonal quality for every grid applied to FLUENT, can be observed. Orthogonal quality maintains a range from 0 to 1, with the values close to 0 corresponding to low quality:

30^{o} slant angle

$y^{+} = 1$	$y^{+} = 5$	$y^{+} = 15$
3.47406×10^{-1} (0.347406)	1.84742×10^{-1} (0.184742)	3.63087×10^{-1} (0.363087)

Table 7 : Minimum orthogonal qualities of the grids used, as calculated by FLUENT for 30^{o} slant angle

25^{o} slant angle

$y^{+} = 1$	$y^{+} = 5$	$y^{+} = 15$
3.47406×10^{-1} (0.347406)	3.25057×10^{-1} (0.325057)	2.12427×10^{-1} (0.212427)

Table 8 : Minimum orthogonal qualities of the grids used, as calculated by FLUENT for 25^{o} slant angle

35^{o} slant angle

$y^{+} = 1$	$y^{+} = 5$	$y^{+} = 15$
3.47373×10^{-1} (0.347373)	3.24902×10^{-1} (0.324902)	2.11894×10^{-1} (0.211894)

Table 9 : Minimum orthogonal qualities of the grids used, as calculated by FLUENT for 35^{o} slant angle

4.4 Simulation Results in FLUENT & UCNS3D

The aforementioned grids were applied to the FLUENT commercial solver, in order to exhibit both robust and accurate results that will be put in comparison with the UCNS3D inhouse developed solver. Simulations in UCNS3D, mostly due to the numerical scheme used and the fact that UCNS3D employs higher order schemes [74], [75], [76], [77], needed many iterations to achieve convergence (more than 400000 with local time stepping). The samples presented, are serving as a comparison value between FLUENT and results from similar experimental or computational cases from the literature review. Simulations were performed using the following configurations in FLUENT:

I.) Solver was density – based, time – steady, with absolute velocity formulation

II.) The turbulence model used was a 1 equation, Spalart – Allmaras strain/vorticity based, with the energy equation set to be solved, as well

III.) Inflow velocity of 40 m/s

IV.) Implicit solution method

V.) For most of the cases, the CFL condition was CFL = 50, except for the 35^o y+1 and y+5 cases, which was 30 in order to help achieve faster convergence. For the same reason, a condition of CFL = 25 was used as well in the 25^o and 35^o y+15 cases.

Tables 10, 11 and 12 (30^o, 25^o and 35^o slant angles, respectively) exhibit the values of C_D (Drag coefficient) and C_L (Lift coefficient), for every grid configuration. All of the 2D grids presented in the study and simulated in FLUENT, had converged solutions. It must be denoted that convergence was not achieved in some of the cases, as a result of various factors, which will be analyzed separately in every chart.

4.4.1.1 Ahmed Body 30º Slant Angle in FLUENT & UCNS3D

Table 10 exhibits the results (C_D and C_L) of the simulations for FLUENT, while Tables 11 and 12 correspond to the two Riemann solver configurations (Rusanov and HLLC respectively), used for UCNS3D. Table 13 is based in values found in the literature review. CFL condition might differ in the FLUENT cases, as an implicit scheme was used, however, for the UCNS3D code CFL = 1, as it uses an explicit scheme.

y+ factor	C_D (Drag Coefficient)	C_L (Lift Coefficient)
y+ 1 CFL = 50	0.138	0.5
y+ 5 CFL = 50	0.135	0.545
y+ 15 CFL = 50	0.123	0.638

Table 10 : Drag and Lift coefficient results for all the grids used for the Ahmed Body with a 30^o slant angle for FLUENT

y+ factor	C_D (Drag Coefficient)	C_L (Lift Coefficient)
y+ 1	0.178	0.574
y+ 5	0.169	0.611
y+ 15	0.144	0.650

Table 11 : Drag and Lift coefficient results for all the grids used for the Ahmed Body with a 30^o slant angle for UCNS3D (Rusanov Riemann solver configuration)

y+ factor	C_D (Drag Coefficient)	C_L (Lift Coefficient)
y+ 1	0.186	0.947
y+ 5	0.169	0.856
y+ 15	0.217	0.827

Table 12 : Drag and Lift coefficient results for all the grids used for the Ahmed Body with a 30^o slant angle for UCNS3D, with the less dissipative HLLC Riemann solver configuration

Reference number	C_D (Drag Coefficient)	C_L (Lift Coefficient)
[2]	0.26	
[4]	0.278	0.352
[34]	0.262	

Table 13 : Drag and Lift coefficient results for 30^o slant angle, based on results found on the literature review

For an inlet velocity of 40 m/s in which this study was set, Ahmed [2] in his original experiment managed to achieve a mean drag coefficient of 0.26. Aider et al. [4] for the same velocity had a mean drag coefficient of 0.278 and Yunlong and Moser [34] a value of 0.262.

4.4.1.2 30^{o} Slant Angle Contours and Plots

Convergence was achieved (through help of adjusting the Courant number = 50) and the Implicit numerical scheme used in the solver, at 800, 877 and 227 iterations for $y^+ = 1$, $y^+ = 5$ and $y^+ = 15$ respectively.

Contours of Velocity Magnitude for FLUENT simulations

$y^+ = 1$

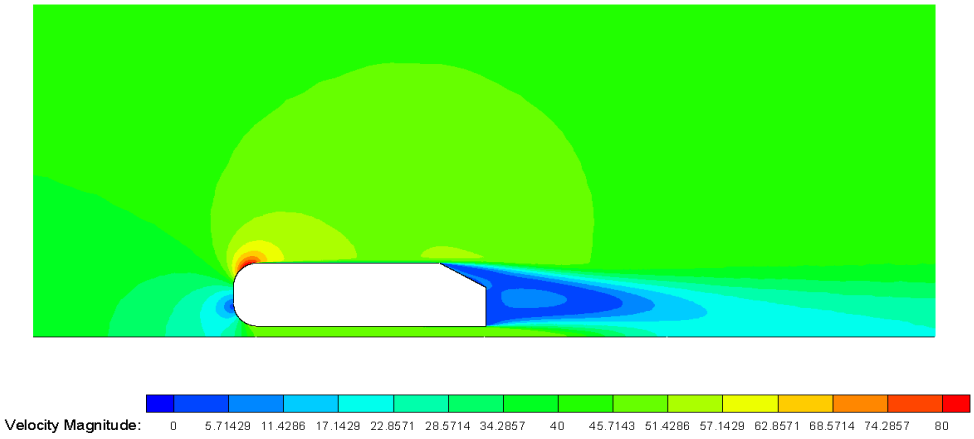

Fig. 62: Contours of velocity magnitude for the 2D *30^{o}* slant angle case with a *y+ = 1*

$y^+ = 5$

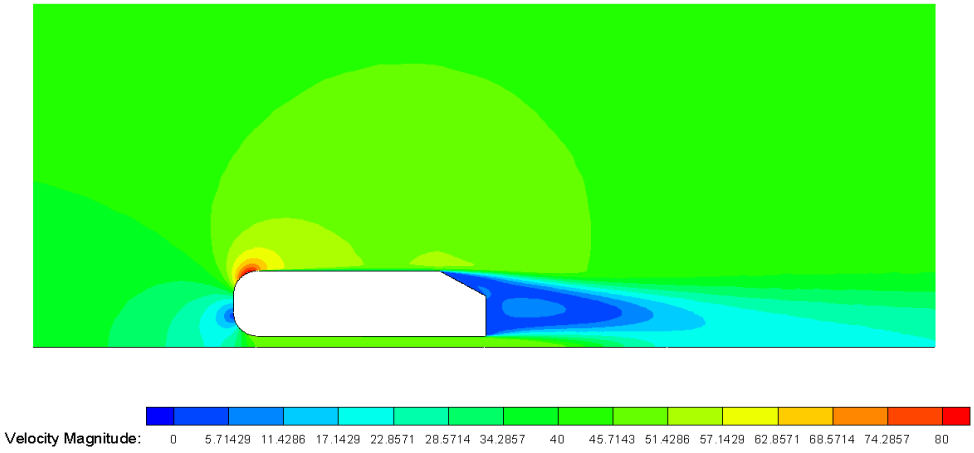

Fig. 63: Contours of velocity magnitude for the 2D *30^{o}* slant angle case with a *y+ = 5*

$y^+ = 15$

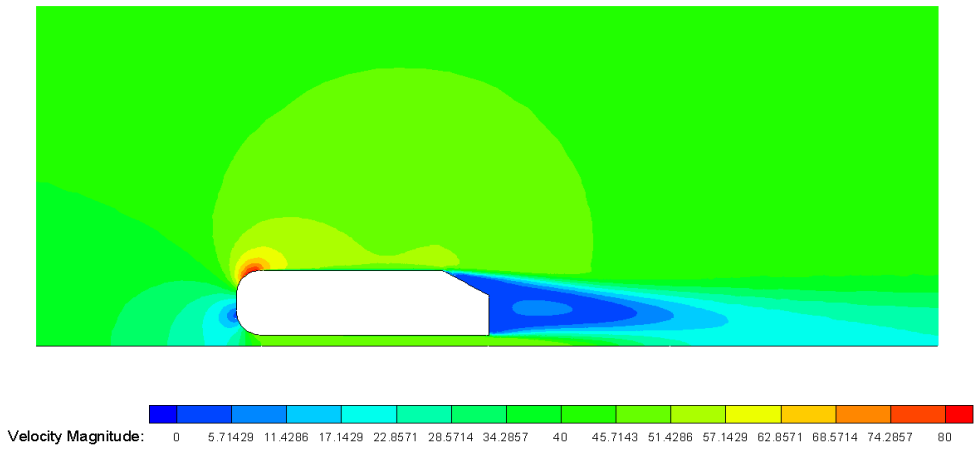

Fig. 64: Contours of velocity magnitude for the 2D *30°* slant angle case with a *y+ = 15*

A flow separation in the upper front of the Ahmed body is apparent from the Contours of the Velocity Magnitude. This flow separation was not observed by Ahmed in his experiments and it is of great interest for further investigation, concerning it's behavior under various circumstances. The difference on how turbulence on the wake is exhibited through the different grids is noticeable as well. As the number of the y^+ factor rises and the grid becomes coarser, the flow effects taking place in the wake are depicted with less detail.

A typical example of that, is the forming of the oval separation bubble created in the wake of the body, as in the $y^+ = 1$ case, in which appears clearly and with detail in the contours but a tendency for accurate depiction to fade is presented as the y^+ factor rises, concluding in depicting only the main bubble created in the $y^+ = 15$. However, the difference is not particularly apparent between the first two ($y^+ = 1$ and $y^+ = 5$) cases.

Streamlines for the FLUENT cases

$y^+ = 1$

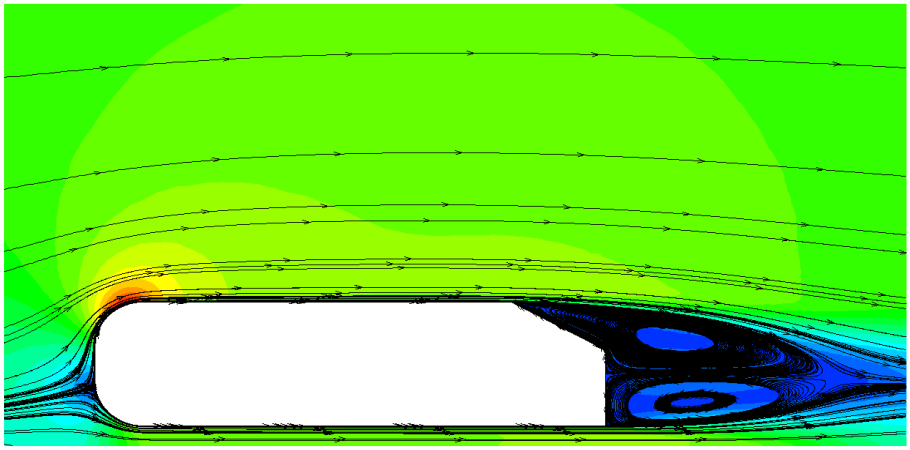

Fig. 65: Streamlines for the 2D 30^o slant angle case with a *y+ = 1*

$y^+ = 5$

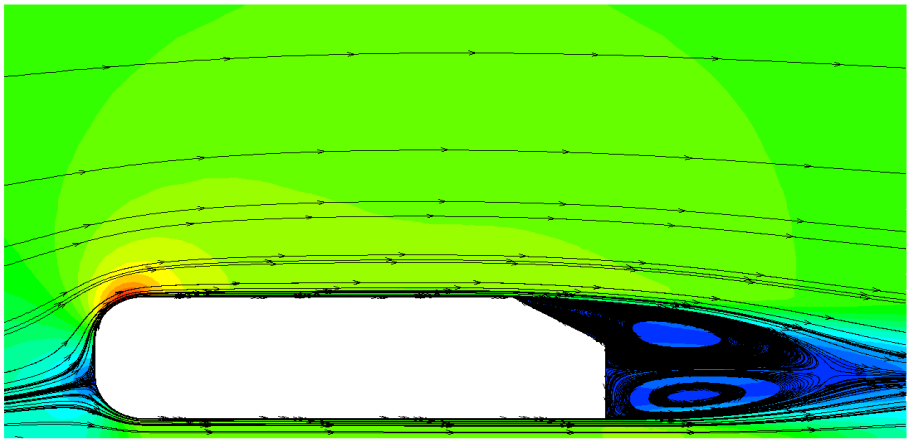

Fig. 66: Streamlines for the 2D 30^o slant angle case with a *y+ = 5*

$y^+ = 15$

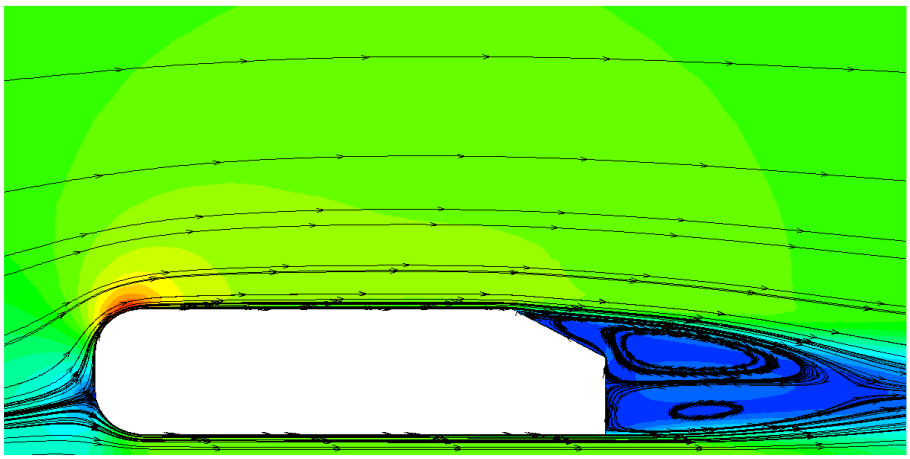

Fig. 67: Streamlines for the 2D 30^o slant angle case with a *y+ = 15*

As in the case of the velocity magnitude contours, a tendency for the details of the flow features to be lost in the near wake of the body, is apparent in the streamlines as well, as the y^+ number is rising and the grid becomes coarser. In the y^+ = 1 case, however, the two vortices created in the wake of the Ahmed body are exhibited. The streamline pattern in the near wake for this case, is quite similar to the one investigated by Ahmed [3] for the typical automobile shape and flow patterns of a production notchback automobile. The two nearly equal halves in which the central plane flow is divided, maintain an opposite (between them) circulatory motion. Fig. 68 and Fig. 69 exhibit the results from the Rusanov Riemann solver in contours of velocity magnitude and turbulent viscosity ratio.

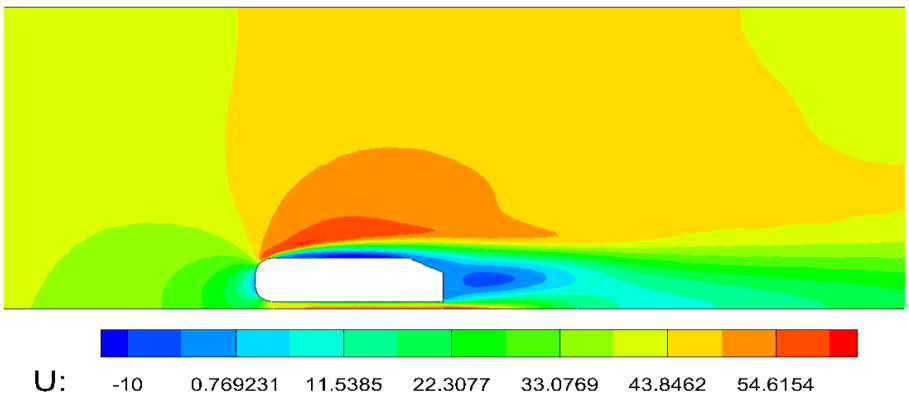

Fig. 68: Contours of velocity magnitude for the 30^o slant angle case in UCNS3D with the RUSANOV solver

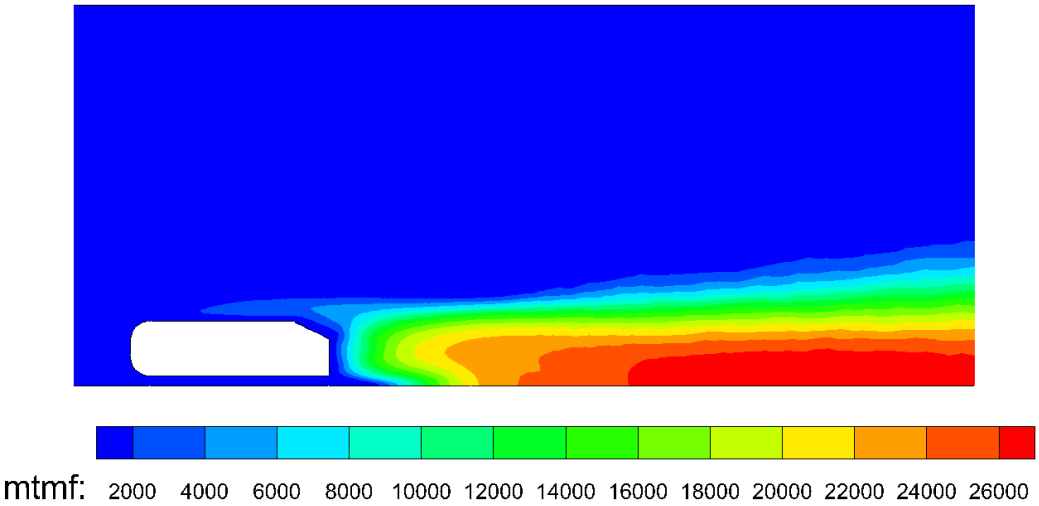

Fig. 69: Contours of turbulent viscosity ratio for the 30^{o} slant angle case in UCNS3D with the RUSANOV solver

Due to the fact that the RUSANOV solver is highly dissipative, some overpredictions of the occurring flow are apparent in the figures, with one of them being the separation bubble created in the upper part of the body, preserved for its whole length downstream the body and getting connected with the one created in the wake region. The turbulent viscosity ratio (mtmf), as observed in Fig. 69 is in the region of ≈26000 which is not an abnormal value for this sort of 2D flow.

4.4.2.1 Ahmed Body 25º Slant Angle in FLUENT and UCNS3D

Table 14 exhibits the results (C_D and C_L) of the simulations in FLUENT, while Tables 15 and 16 for UCNS3D with Rusanov and HLLC solvers, respectively. Table 17 is based in values found in the literature review.

y+ factor	C_D (Drag Coefficient)	C_L (Lift Coefficient)
y+ 1 CFL = 50	0.135	0.526
y+ 5 CFL = 50	0.127	0.576
y+ 15 CFL = 25	0.116	0.669

Table 14 : Drag and Lift coefficient results for all the grids used for the Ahmed Body with a 25^o slant angle for FLUENT

y+ factor	C_D (Drag Coefficient)	C_L (Lift Coefficient)
y+ 1	0.05	0.151
y+ 5	0.174	0.833
y+ 15	0.238	0.911

Table 15 : Drag and Lift coefficient results for all the grids used for the Ahmed Body with a 25^o slant angle for UCNS3D (Rusanov solver configuration)

y+ factor	C_D (Drag Coefficient)	C_L (Lift Coefficient)
y+ 1	0.177	0.949
y+ 5	0.187	0.858
y+ 15	0.228	0.865

Table 16 : Drag and Lift coefficient results for all the grids used for the Ahmed Body with a 25^o slant angle for UCNS3D, with the less dissipative HLLC solver configuration

Reference Number	C_D (Drag Coefficient)	C_L (Lift Coefficient)
[2]	≈ 0.15	
[5]	0.15	
[6]	0.385	0.4225
[46]	0.266	

Table 17 : Drag and Lift coefficient results found in the literature review

In the initial Ahmed [2] study, the drag coefficient was in the region of 0.15, a value which is in accordance with the study of Lienhart et al [5] who managed to achieve a value of 0.15 as well. Thacker et al [6], in their study presented a value

according to the fluctuation of the Reynolds number for a sharp edge configuration of the 25^o slant angle in order to compare results with a rounded edge configuration. Rajsinh and Karuppa [46], simulated a similar case for a 25^o slant angle with freestream velocity of 40 m/s and the use of Spalart – Allmaras model, resulting in a drag coefficient of 0.266

The values taken from obtained from FLUENT for the drag coefficient can be characterized as satisfying, as they are in the same region as the ones taken from the literature review. However, as in the previous case, a safe conclusion not be reached until the UCNS3D cases are converged or reach a steady residual state, to be presented.

4.4.2.2 25^o Slant Angle Contours and Plots

Convergence was achieved (through fluctuating the Courant number) and the Implicit numerical scheme used in the solver, at 765, 388 and 408 iterations for the $y^+ = 1$, $y^+ = 5$ and $y^+ = 15$ cases, respectively. For the three y^+ cases under examination for the 25^o slant angle, FLUENT produced the following charts and contours:

Contours of Velocity Magnitude for FLUENT:

$y^+ = 1$

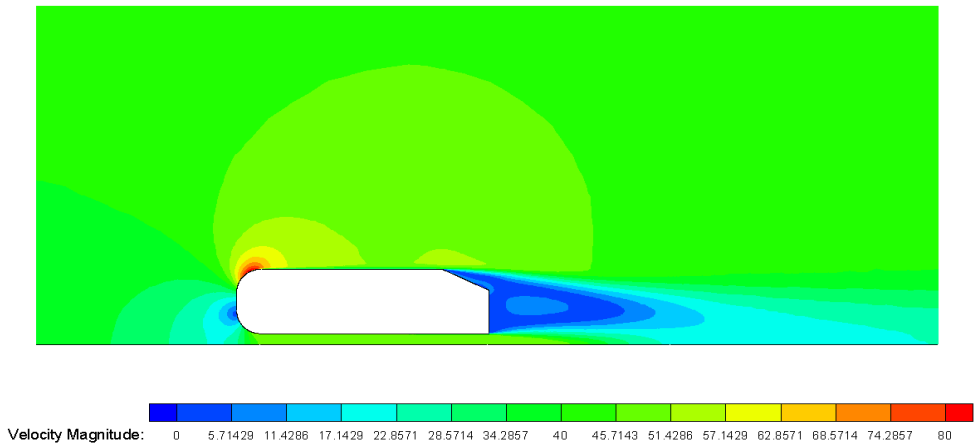

Fig. 70: Contours of velocity magnitude for the 2D *25^o* slant angle case with a *y+ = 1*

$y^+ = 5$

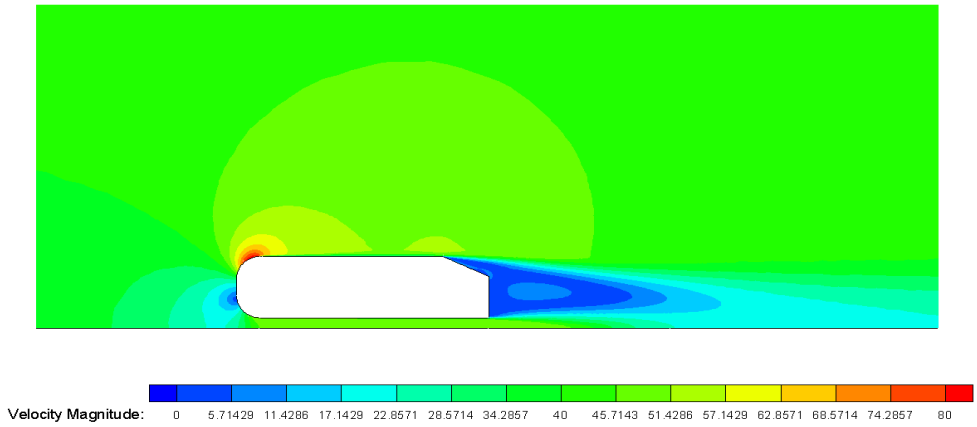

Fig. 71: Contours of velocity magnitude for the 2D 25^o slant angle case with a *y+ = 5*

$y^+ = 15$

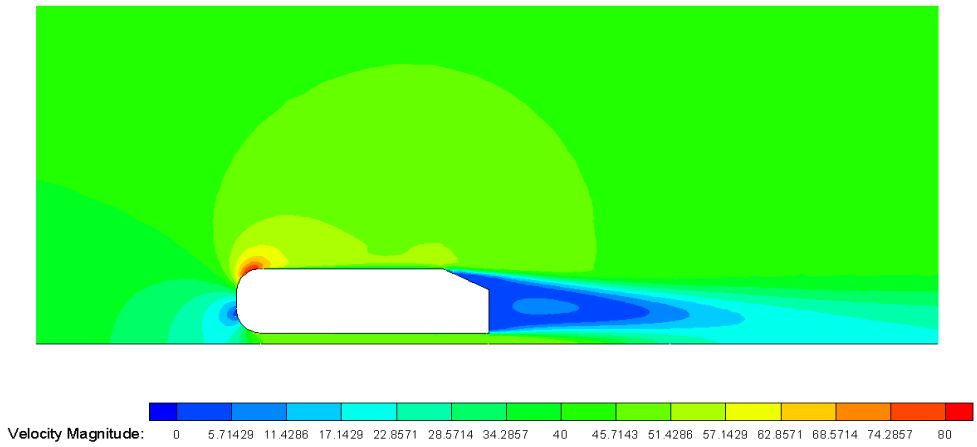

Fig. 72: Contours of velocity magnitude for the 2D 25^o slant angle case with a *y+ = 15*

The flow topology is predicted well in FLUENT and comes in accordance with the literature review [46] examples of the same method (Spalart – Allmaras) and same conditions. The separation bubble in the rear is depicted well in the $y^+ = 1$ case, however, it is once again proved that detail of the grid fades away as the y^+ factor rises, something that can be seen in the contours of velocity magnitude for the $y^+ = 15$ case.

Of great interest is the difference in the size of the separation bubble in the rear, as it is of slightly smaller size than in the 30^o case. Another flow feature which becomes apparent in the flow topology of the $y^+ = 1$ case in the downstream region of the body and seems to be inextricably connected with the slant angle growth, is the appearance of a third bubble due to the flow separation which is clearly visible in this particular angle case (25^o). The effect of the flow pattern exhibited in this case can be seen in the C_D (drag coefficient) values, which are definitely improved in FLUENT in comparison to the corresponding values of the 30^o slant angle case.

Streamlines

$y^+ = 1$

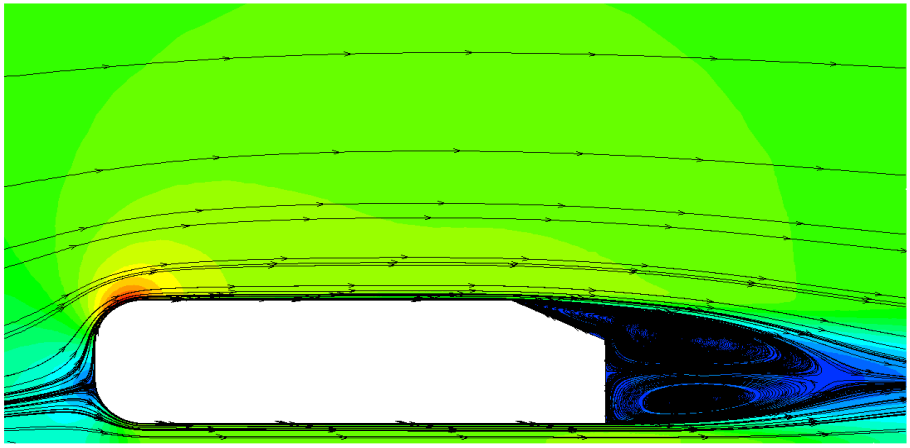

Fig. 73: Streamlines for the 2D *25^o* slant angle case with a *y+ = 1*

$y^+ = 5$

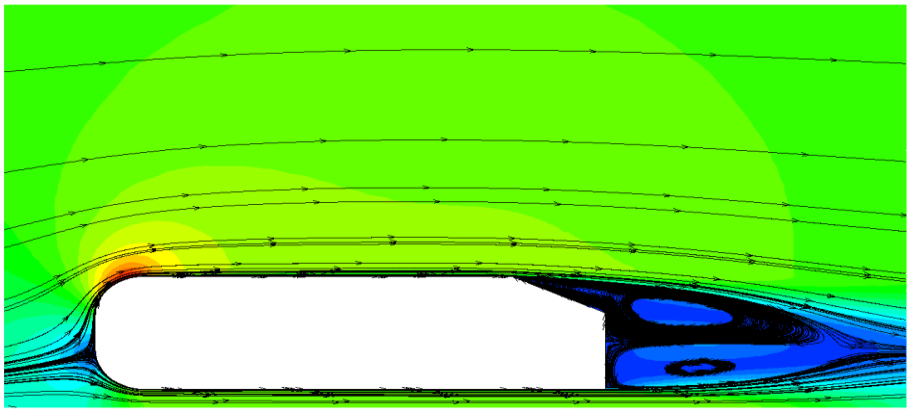

Fig. 74: Streamlines for the 2D *25^o* slant angle case with a *y+ = 5*

$y^+ = 15$

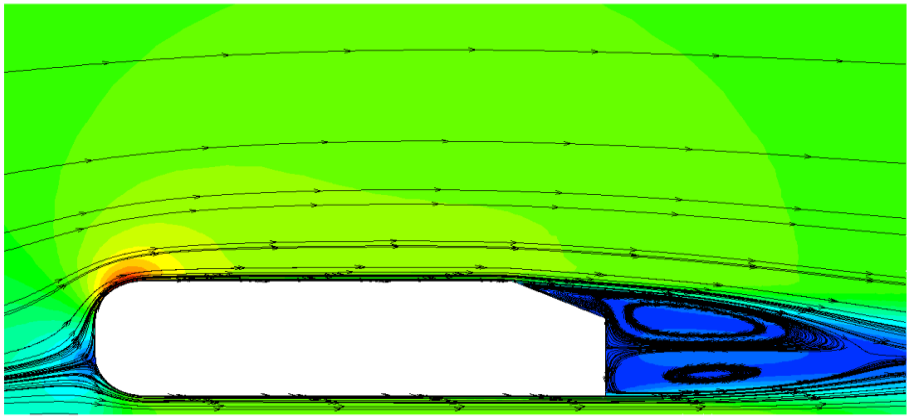

Fig. 75: Streamlines for the 2D *25°* slant angle case with a *y+ = 15*

Despite the fact that the streamlines present the same pattern as their corresponding in the 30° slant angle case, there is a difference in the size of the contra – rotating vortices in the near – wake region of the body. More specifically, the upper half of the central plane flow is of smaller size than in the previous (30° slant angle) case. The smaller flow separation taking place in the 25° slant angle, explains the reduced drag coefficient values received from the simulations in FLUENT in comparison to these of the 30° case.

Concluding for the 25° slant angle case, it can be said that the flow separation takes place throughout the generic body in a smoother way than the rest of the cases examined, something that can be seen both in the flow topology in the near – wake region and with the way the vortices are formed in comparison to the 30° and 35° cases.

4.4.3.1 Ahmed Body 35° Slant Angle in FLUENT

Table 18 exhibits the results (C_D and C_L) of the simulations in FLUENT, for the 35° slant angle cases. For the UCSN3D case and the Rusanov and HLLC solvers configurations, the results can be seen in Tables 19 and 20, respectively. Table 21 exhibits values taken from the bibliography used.

y+ factor	C_D (Drag Coefficient)	C_L (Lift Coefficient)
y+ 1 CFL = 30	0.181	0.535
y+ 5 CFL = 30	0.137	0.534
y+ 15 CFL = 25	0.131	0.591

Table 18 : Drag and Lift coefficient results for all the grids used for the Ahmed Body with a 35^o slant angle for FLUENT

y+ factor	C_D (Drag Coefficient)	C_L (Lift Coefficient)
y+ 1	0.181	0.652
y+ 5	0.193	0.777
y+ 15	0.236	0.838

Table 19 : Drag and Lift coefficient results for all the grids used for the Ahmed Body with a 35^o slant angle for UCNS3D (Rusanov solver configuration)

y+ factor	C_D (Drag Coefficient)	C_L (Lift Coefficient)
y+ 1	0.144	0.899
y+ 5	0.187	0.852
y+ 15	0.209	0.820

Table 20 : Drag and Lift coefficient results for all the grids used for the Ahmed Body with a 35^o slant angle for UCNS3D, with the less dissipative HLLC solver configuration

Reference Number	C_D (Drag Coefficient)	C_L (Lift Coefficient)
[5]	0.17	

Table 21 : Drag and Lift coefficient results found in the literature review

Lienhart et al. [5] managed to achieve a $C_D = 0.17$ value for the 35^o slant angle case. Difficulty was encountered in finding further data for the 35^o slant angle problem with the same setup as in this study.

4.4.3.2 35º Slant Angle Contours and Plots

In order to manage convergence of the solution in this particular (35°, y^+ = 1) case, a slight modification in turbulent viscosity had to be applied. The case was simulated for a turbulent viscosity was set equal to 0.5, along with a Courant number of 30. Convergence was achieved with the Implicit numerical scheme used in the solver, at 642, 913 and 526 iterations for the y^+ = 1, y^+ = 5 and y^+ = 15 cases, respectively. For the three y^+ cases under examination for the 35° slant angle, FLUENT produced the following charts and contours:

Velocity Magnitude

y^+ = 1

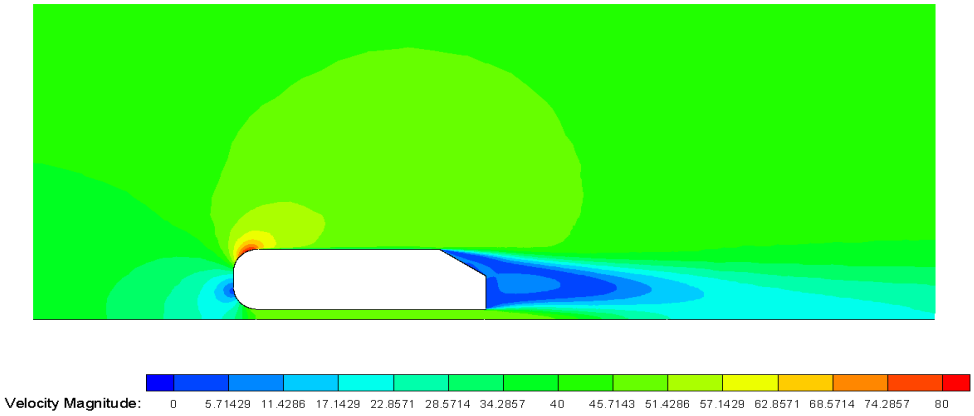

Fig. 76: Contours of velocity magnitude for the 2D *35°* slant angle case with a *y+ = 1*

y^+ = 5

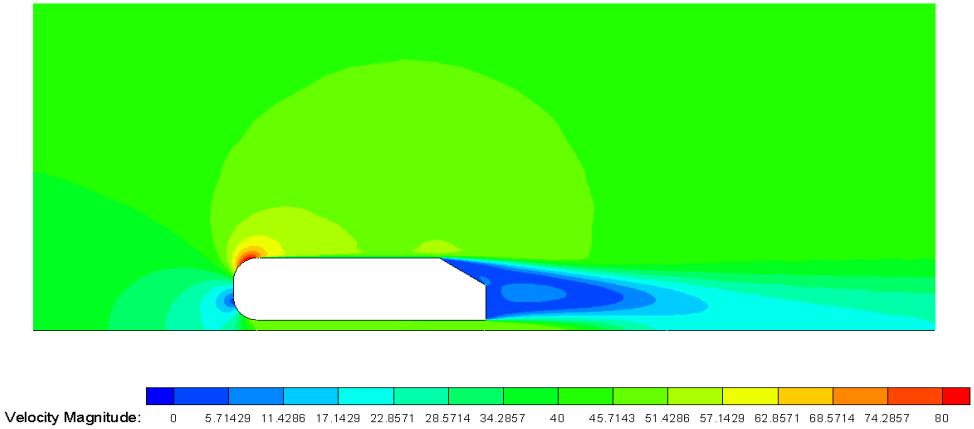

Fig. 77: Contours of velocity magnitude for the 2D *35°* slant angle case with a *y+ = 5*

$y^+ = 15$

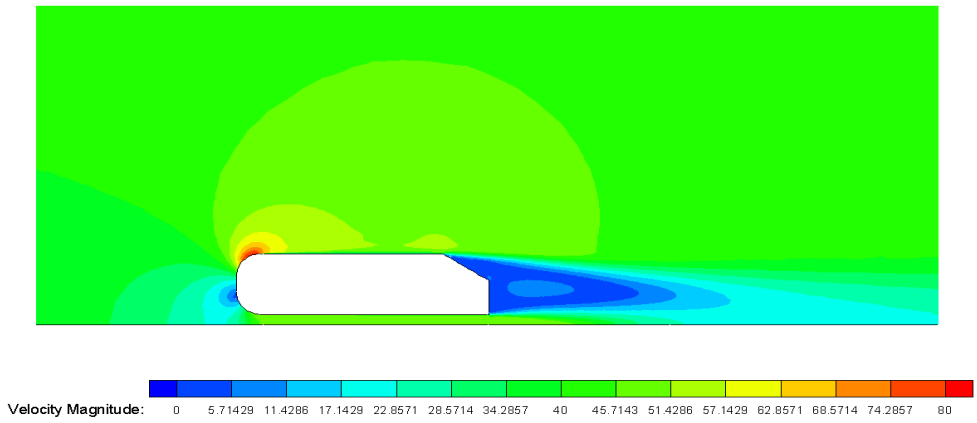

Fig. 78: Contours of velocity magnitude for the 2D *35°* slant angle case with a *y+ = 15*

The main difference in the 35° slant angle cases, is the size of the flow separation bubble created in the near – wake region which is of bigger size in comparison to all the cases examined before. The third separation bubble created due to flow separation just over the slant angle and examined in the 30° slant angle case, appears a tendency to unite with the main separation bubble in the near – wake region of the body. The behavior of the flow separation before the slant angle and how the separation bubble created there tends to get unified with the one in the near – wake region as the slant angle grows bigger, calls for further examination in order to clarify the way in which further growth of the slant angle could affect the aforementioned flow features.

Streamlines

$y^+ = 1$

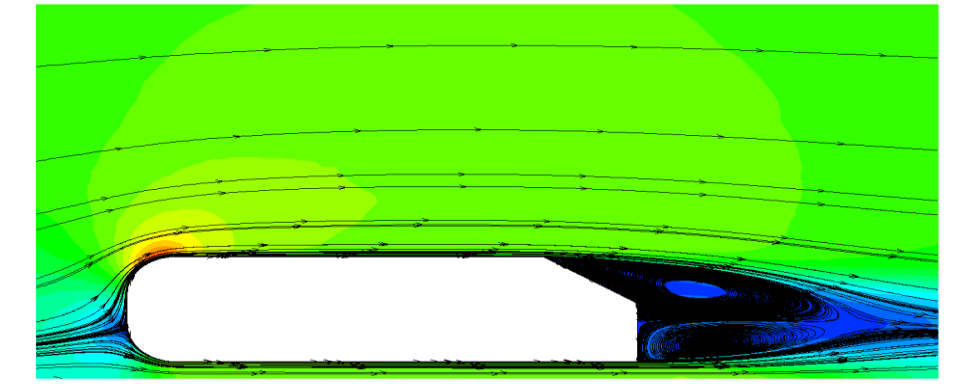

Fig. 79: Streamlines for the 2D *35°* slant angle case with a *y+ = 1*

$y^+ = 5$

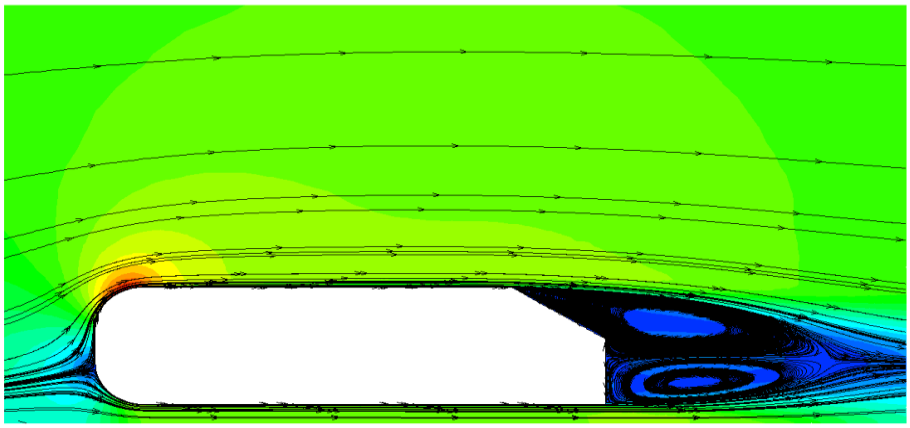

Fig. 80: Streamlines for the 2D 35^o slant angle case with a *y+ = 5*

$y^+ = 15$

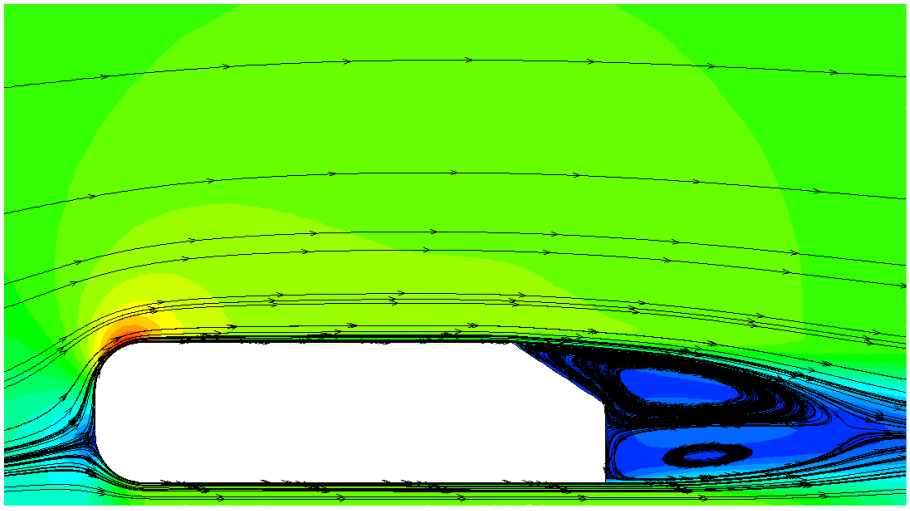

Fig. 81: Streamlines for the 2D 35^o slant angle case with a *y+ = 15*

In this particular case, the turbulence and the longitudinal vortices exhibited are more intense than in the previously examined cases. A free shear layer was formed in the upper region of the slant angle. This comes in connection with the raise of the slant angle degree number (35^o). The vortices created reach in an extent, such that in order to help the simulation achieve convergence in FLUENT, the turbulent viscosity had to be limited to 0.5 and the Courant number reduced to 50. A fully detached flow is exhibited, as observed by Uruba and Hladik [72], as well.

The main feature in which the 35^{o} slant angle case differs from the 25^{o} one, is the way the contra – rotating vortices are exhibited in the near – wake region of the body. More specifically, in the 35^{o} angle case, the upper vortex appears to be stronger than the lower one, in contrast to the 25^{o} and 30^{o} slant angle case, where the upper vortex is weaker than the bottom one. The dissipative schemes used may be responsible for the visualization results. The difference between dissipative and dispersive schemes is connected to the spatial derivatives used. When the aforementioned derivatives are expanded from the Taylor series, in order to observe errors and the propagation of the waves, a wavenumber approach can be feasible. While the dissipative schemes mostly consist of the functions of the waves dying in magnitude, the dispersive schemes consist of a lack of calculation for the speed of the wave, resulting in it presenting a "lag" behind the actual function. This can be further observed by doing wavenumber analysis for schemes as low as 2nd order.

4.5 Cd and Cl Results in FLUENT and UCNS3D for the 2D Cases

4.5.1 Cd Results

A comparison between the Drag Coefficient values returned in the results from the simulations in FLUENT and how these are fluctuating with a change in the y+ number is exhibited in Fig. 82.

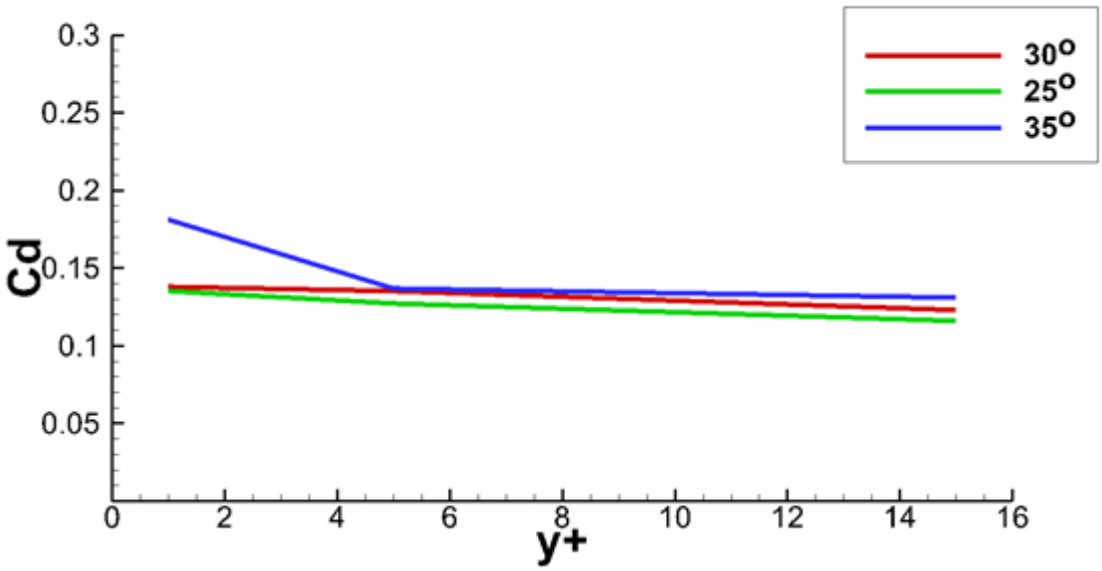

Fig. 82: Cd and y+ values from the results of the 2D simulations in FLUENT

It is apparent that there is an inversely proportional connection between the drag coefficient and the y+ values, as while the latter increase, the first exhibit a tendency to decrease and thus, further diverging from the experimental ones. The cd values closest to the experimental ones were obtained through the result feedback of the simulations in the y+1 cases (fine grid). However, these values, still diverged from the experimental ones, and as the grid became coarser, there was a tendency for this result divergence to grow bigger. These results might make sense in a way, if the number of variables in the problem setup, which add up to the production of such results by FLUENT, are taken into account. First and foremost, the full flow features cannot be unraveled due to the 2D nature of the cases. The use of the Spalart – Allmaras turbulence model for highly detached flows such as flows around an automobile, resemblances of which are examined here, is unsuitable. Additionally, the Riemann solver used in FLUENT, appears to be a highly dissipative one and taking into account the more coarse grid as the y+ value increases, as well, it is only natural that the final results will diverge greatly in comparison to the experimental ones.

Results obtained for the drag and lift coefficients with the UCNS3D inhouse developed code, can be observed in Fig. 83 and Fig. 84 for the cases of Rusanov and HLLC Riemann solvers, respectively.

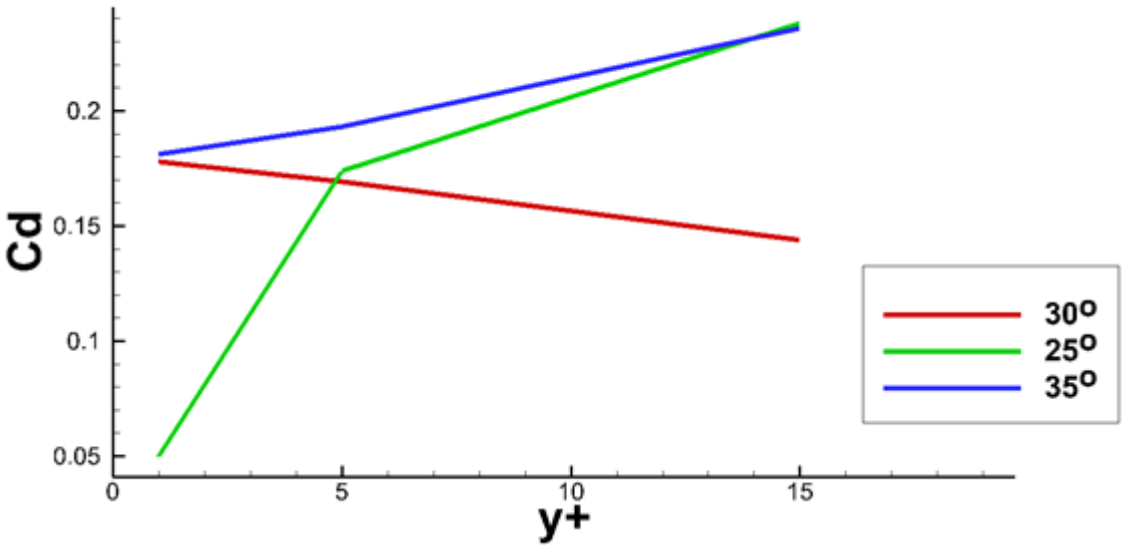

Fig. 83: Cd and y+ values from the results of the 2D simulations in UCNS3D with RUSANOV solver

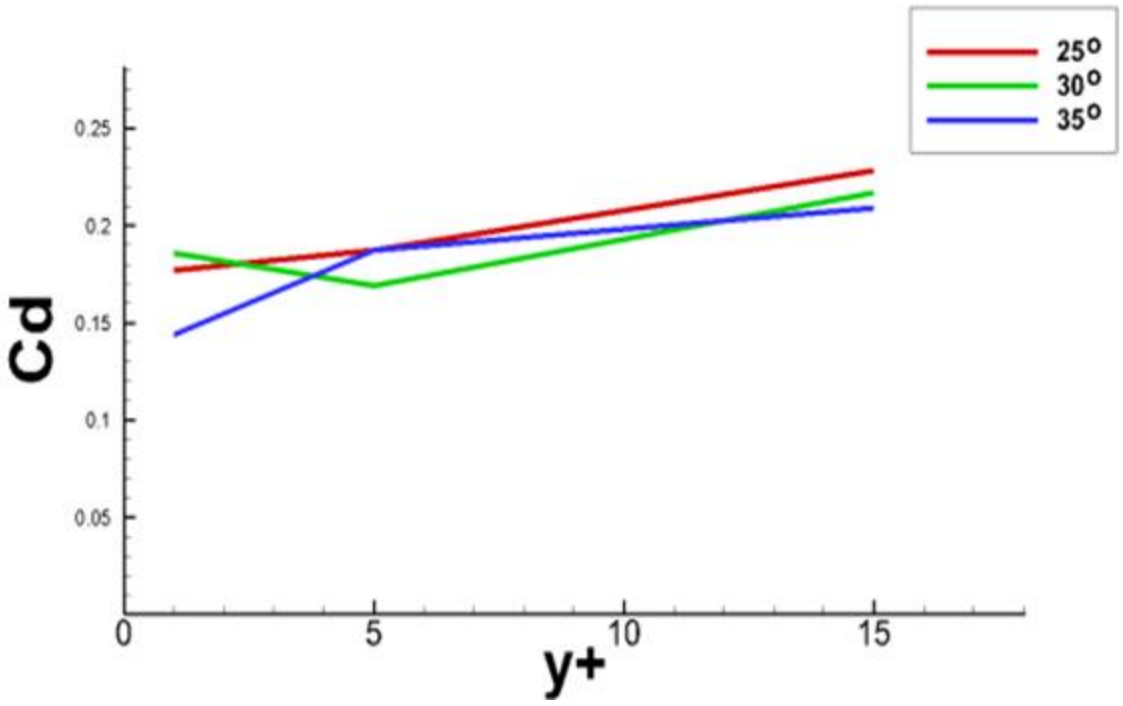

Fig. 84: Cd and y+ values from the results of the 2D simulations in UCNS3D with HLLC solver

It is apparent from Fig. 82 – 84 that there is a controversy in the results obtained. In the 30° slant angle case, the values obtained with FLUENT, averaging at ≈0.13, are diverging in comparison with the experimental values of ≈0.27, as the values obtained are almost half of the experimental ones. The results from the HLLC solver are the ones being closer to the experimental ones, averaging ≈0.19, however divergence is still exhibited when compared. For the 25° and the 35° slant angle cases, the results from FLUENT are coping well with the ones from previous studies, something which is the case only for the y+=1 and y+=5 cases in the HLLC solver, as the remaining results are diverging from the numbers of previous studies. Results returned from the more dissipative Rusanov solver, were unrealistic, except for the 35° y+1 and y+5 slant angle cases, which beared resemblance to the ones found in bibliography.

4.5.2 Cl Results

In Fig. 85, a lift coefficient – y+ plot can be observed for the FLUENT simulations. Fig. 86 and Fig. 87 exhibit the same plot for the results obtained in UCNS3D with the Rusanov and HLLC solvers, respectively.

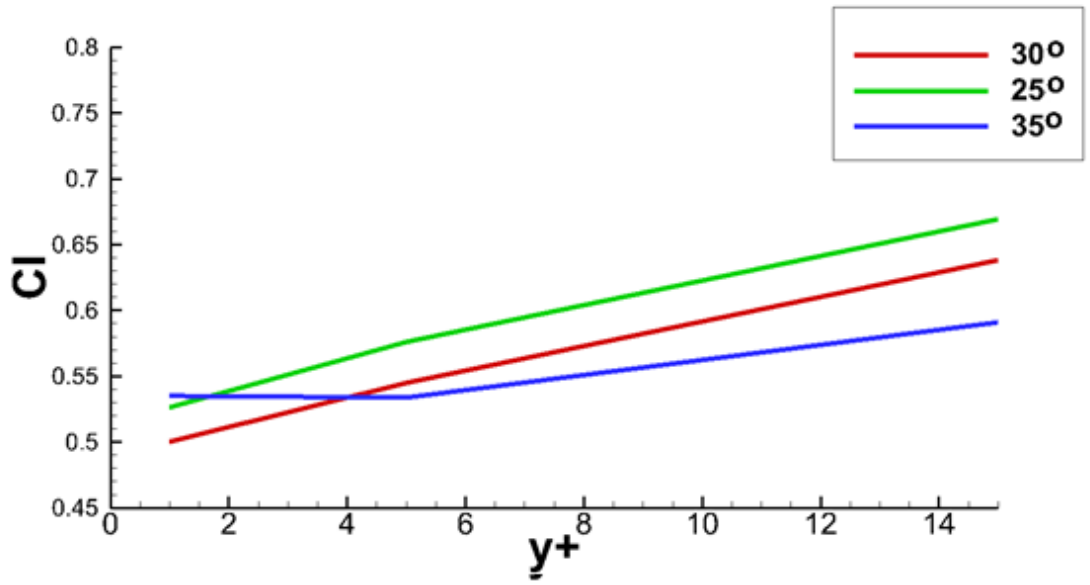

Fig. 85: Cl and y+ values from the results of the 2D simulations in FLUENT

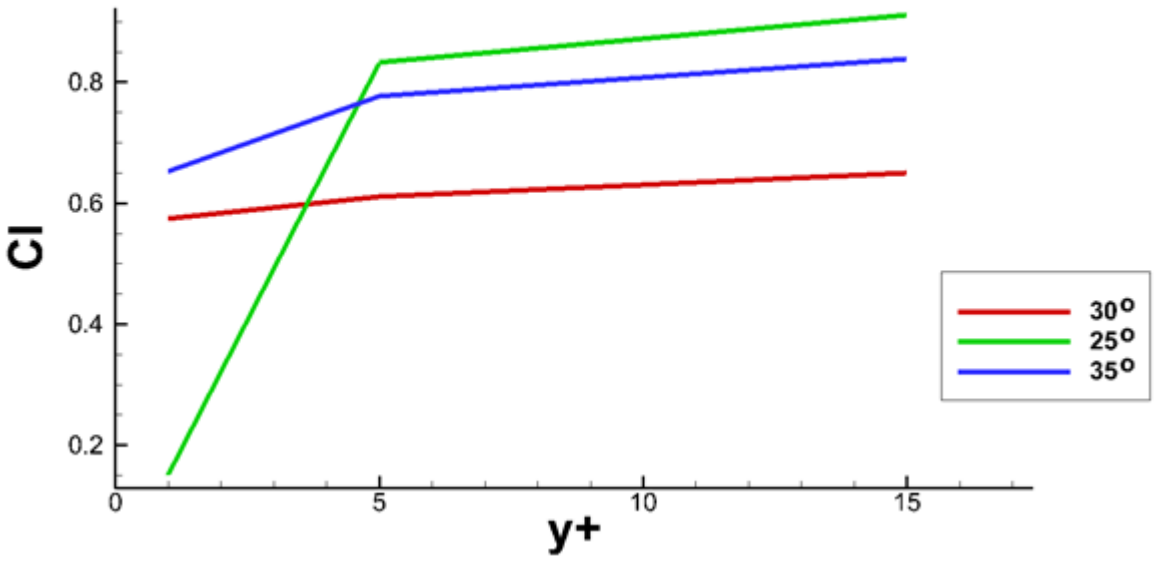

Fig. 86: Cl and y+ values from the results of the 2D simulations in UCNS3D with RUSANOV solver

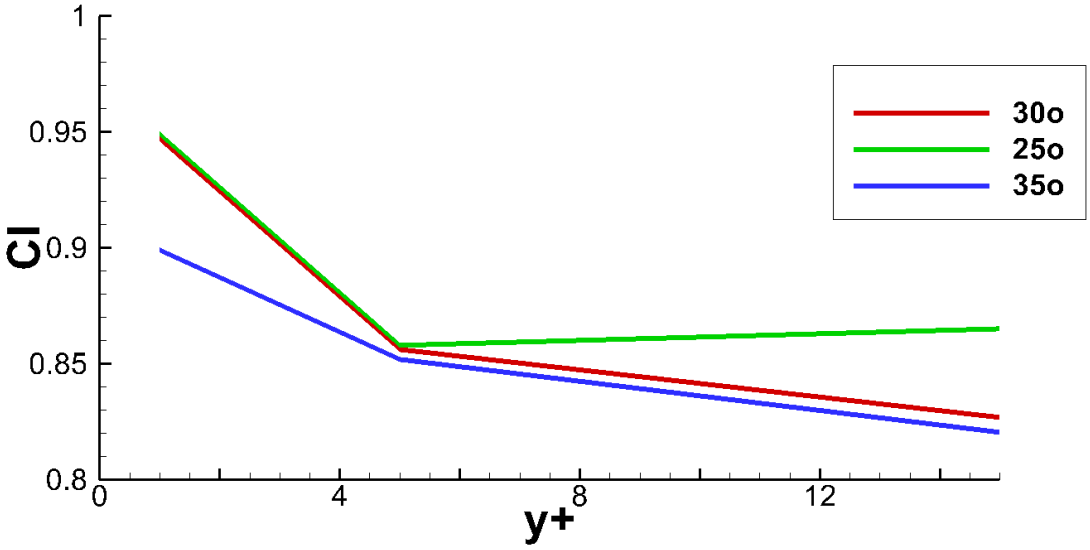

Fig. 87: Cl and y+ values from the results of the 2D simulations in UCNS3D with HLLC solver

The values obtained for the lift coefficient in the FLUENT simulations with a 2nd order scheme used, are the closest in the experimental values, despite the fact that they are still diverging from them. The results from UCNS3D were greatly diverging from the bibliography values, even reaching cl ≈ 0.949 the 30° slant angle y+1 case, a value almost triple than the values expected (≈ 0.35). As the y+ value raises and the grid becomes coarser, the lift coefficient presents a tendency to constantly raise in FLUENT, reaching unrealistic values, while in UCNS3D the values tend to stabilize in the unrealistic value cl ≈ 0.8 – 0.9 area.

4.6 Conclusions for the 2D Cases

There are of course some parameters that should be taken into consideration, when examining the flow around the Ahmed body. First and foremost should be that the Ahmed body is an inherently difficult problem to resolve. The solution to the flow patterns and structures exhibited in every slant angle case are very challenging, as each is presented with moderate difficulty and characteristics. This has as a result the need to constantly improve the methods (turbulence models, numerical schemes and other parameters) used to resolve the problem, as some might be more effective and provide better results in certain cases than others will.

In all the cases examined so far, the computational results, both in a commercially acclaimed solver such as FLUENT, but in UCNS3D as well, might exhibit discrepancies in comparison to these extracted by experiments, mostly due to the fact that the problem setup up to this point, is a 2D case, in a problem created to be solved in three dimensions. Unreliable results might come as a consequence of using a 2D instead of a 3D interface to solve the problem.

The creation of a smooth grid and emphasis in the points where the flow features are observed is of crucial importance before running a simulation in every (commercial or not) solver. The grids used so far are modified and detailed with this exact same logic, but it must be denoted that due to the fact of running test and final simulations in commercial machines (for FLUENT), a limitation was put to the number of elements and cells adjusted to the capabilities of the machines used, in order to avoid consuming all the RAM. Element number was kept to a minimum in order to cope with the personal machines computing power, in an effort to be combined with maximum efficiency this could provide and reliability in the results extracted. As described analytically in the 3rd Chapter, the grid constructed was structured in the boundary layer around the Ahmed body and unstructured in the rest of the domain, aiming mostly at capturing various flow features taking place in the boundary layers. One of these features which is of great interest, is a separation presented in the upper part, downstream of the Ahmed body, right after the front curve, not mentioned by Ahmed in his initial study. Furthermore, the grid was enhanced by adding "patches" of more detailed unstructured domains in the regions the flow phenomena examined in this study, were taking place. Concerning the contours and results depicted for the grids used in connection with resolving the problem, it is apparent from the cases examined, that the flow patterns and features are exhibited in the best possible way for a y^+ factor equal to 1 ($y^+ = 1$). As observed in the rest of the cases ($y^+ = 5$ but especially the $y^+ = 15$ one), the flow patterns taking place are not that clearly depicted as the y^+ factor is rising, something leading to the conclusion that many flow features might be lost, with the use of a coarser grid. The differences between the $y^+ = 1$ and $y^+ = 5$ cases, can be described as minor.

However, this analytical depiction comes with a cost, as the $y^+ = 1$ cases, mostly due to their greater number of elements (something not always meaning a more analytical solution will emerge, however this stands for this case) are harder to resolve, something that is exhibited in the number of the residuals until convergence was achieved for each case.

Should an analytical grid be combined with extensive and rigorous flow phenomena, such as the longitudinal vortices pattern presented in the 35^o slant angle case, achieving convergence for an analytical ($y^+ = 1$) grid, is even harder. It should be denoted, that in the 35^o slant angle, $y^+ = 1$ case, various parameters had to be adjusted in order to achieve convergence, naming, the change of Courant number in comparison to the rest of the cases and the turbulent viscosity, which had to be reduced in some cases, again. If an indirect conclusion had to be extracted, it could be said that the ideal grid case for a 2D simulation is the $y^+ = 5$, as the solutions can be relatively easily converged, without making use of extensive RAM memory, something that implies the grid can be simulated without particular difficulties in a commercial

machine without the help of HPC support and in the same time, not many flow features are lost, making this a reliable and efficient case.

The choice of the turbulence model used, is of extreme importance, in order to capture all sorts of flow features and patterns taking place in the flow around the Ahmed body. Some turbulence models might be capable of tracing specific flow phenomena, while others might not, offering as a consequence a more reliable and robust solution to the problem. It is strongly recommended to run various simulations in different turbulence models and comparing their results, before concluding to measurements of any kind. The use of vorticity / strain based Spalart – Allmaras turbulence model, along with resolving the energy equation was used in this study. The use of this particular turbulence model, might be responsible for the discrepancies experienced in the 35^{o} slant angle, y^{+} = 1 case. Due to the fact that this model is suitable for flows that do not exhibit a great detachment, it might have presented a failure of modeling the turbulence and the longitudinal vortices created, especially in the supercritical 35^{o} slant angle. Taking these facts into account and in conjunction with the analytical grid used for the y^{+} = 1 case, reducing the turbulent viscosity and Courant number in order to achieve convergence, is only reasonable.

It is of no question that the main phenomena of interest in the flow around the Ahmed body, are inextricably connected with the longitudinal vortices created in different slant angles in the near – wake region downstream the body. In this area, the creation of two contra – rotating vortices in the center of the flow plane are of interest, as well as the creation of a third separation bubble, downstream in the beginning of the slant angle. According to the results and contours extracted from FLUENT, the upper vortex seems to be of greater intensity than the one at the bottom in the 35^{o} slant angle case, something which comes in contrast to what happens in the 30^{o} and 25^{o} slant angle cases, where the lower vortices are more intense. The size of these vortices, varies as well, with the size of the slant angle having a crucial part to the flow pattern. It is observed so far, that as the θ of the slant angle gets bigger, more rigorous and intense phenomena are exhibited in the near – wake region and the separation bubble presents a tendency to grow bigger as well.

Chapter 5 : Results for 3D Simulations

The 3D cases in this study are the ones presenting realistically the Ahmed body problem. The flow is unraveled in its full extent, exhibiting all the basic characteristics of this case study, such as the flow separation in the slant angle, the contra rotational vortices and some flow detachments in the main body, allowing realistic approach through applying a successful numerical method with RANS equations. As a result of adding an extra dimension and examining the problem in a 3D workspace, some issues are raised, rendering the solution of the problem very hard. The effectiveness and robustness of the results produced from both a commercial 2^{nd} order solver such as FLUENT and the higher order schemes used by UCNS3D for extreme conditions (Mach number M = 0.11) when applied in different y+ grid setups, would be tested. The unsteadiness of the problem itself with the rigorous vortex shedding exhibited in the slant angle, in conjunction with the highly oscillatory behavior of the residuals and a turbulence model not used for flows of this type, make convergence almost impossible for a steady state approach. It should be further added, that in the 3D cases restrictions in the computational budget applied, mostly associated with available RAM memory, both in creating the grid and running the simulations, as well. As a result of that, the simulations needed to be run in the ASTRAL HPC unit, resulting in delays in getting results, mostly due to the long queues for job submission.

5.1 Initial Conditions

The initial conditions for the 3D cases examined, were the same as in the 2D cases, which were based on works encountered in the bibliography. The velocity of the air in the inlet was set at $40 m/s^{-1}$. Reynolds number was $Re = 2.8 \times 10^6$ with the outflow gauge pressure being at 100000 Pa (atmospheric).

5.2 Domain Size

No alterations took place in the x and y axes of the domain, in comparison with the 2D cases. The lengths of the z axis vertices were 150 cm. As a result of that, the external domain used was a rectangular of 700 cm x 200 cm x 250 cm. The boundary conditions given to the domain were “Inflow” for the velocity – inlet, “Outflow” for the outlet and “Symmetry” for the surrounding surfaces, except for the one the Ahmed body stands in, simulating the road. Due to the fact that the legs are into contact with the road and in order to achieve the best possible realistic results, the aforementioned surface accumulated the boundary condition of “Moving Wall”. The speed in which the surface was moving, is the same as the velocity inlet and equal to $40 m/s^{-1}$. The Ahmed body in comparison with the external domain can be seen in the following figures:

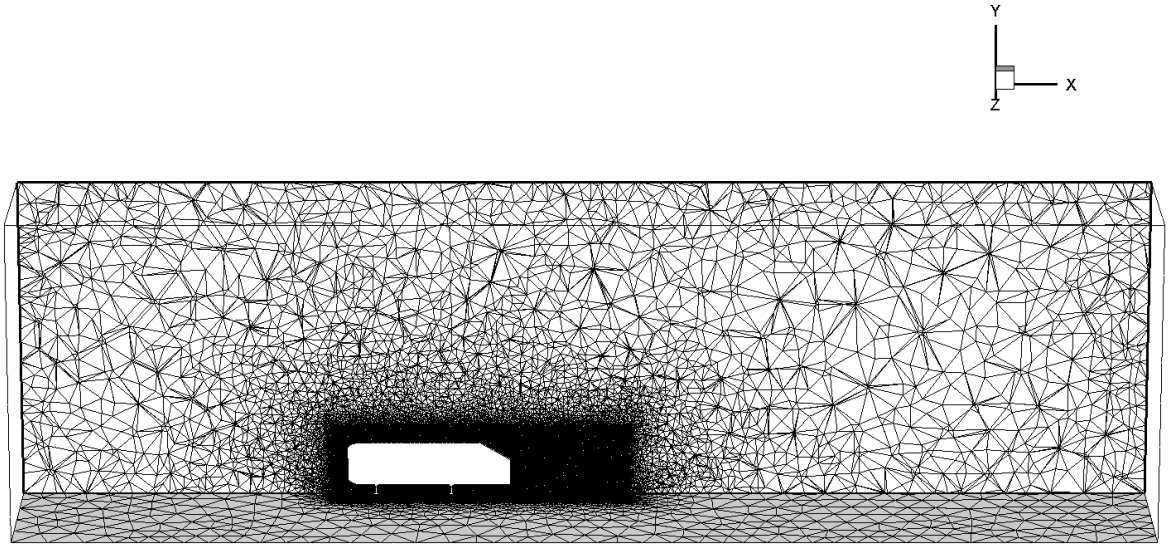

Fig. 88: External (*700cm x 200cm x 250cm*) dimension domain for Ahmed body with a slant angle of 30^o and a $y^+ = 1$

In Fig. 89, the Ahmed body with the subcritical 25^o slant angle can be seen with the external domain used

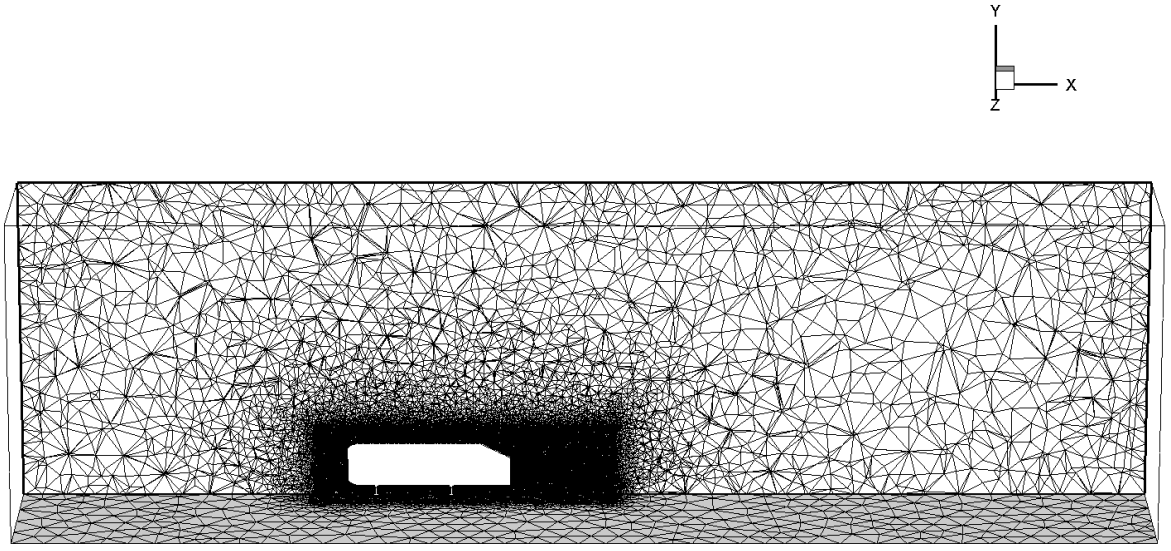

Fig. 89: External (*700cm x 200 cm x 250cm*) dimension domain for Ahmed body with the subcritical 25^o slant angle and a $y^+ = 1$

The same size of domain (700 cm x 200 cm x 250 cm) as the one exhibited in Fig. 90, was the one used for the supercritical 35^o slant angle, as well.

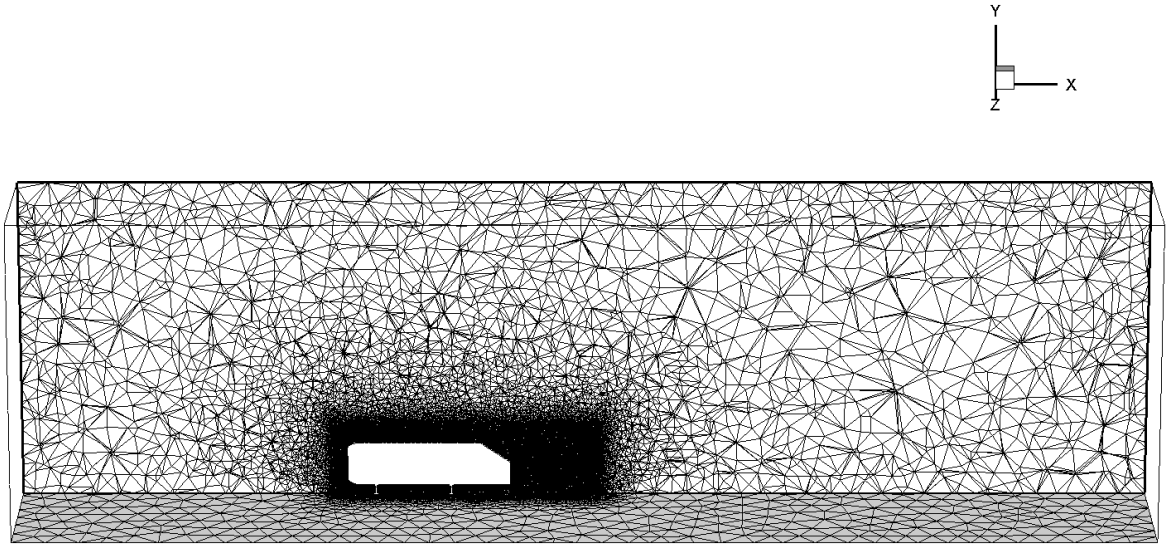

Fig. 90: External (*700cm x 200 cm x 250cm*) dimension domain for Ahmed body with the supercritical slant angle of 35^o and a $y^+ = 1$ value

5.3 Grid Details

As in the 2D cases, one grid was created for each of the three different slant angle cases (30^o, 25^o, 35^o). For each slant angle case respectively, three different grids were created for fine, medium and coarse grid (y+1, y+5, y+15) in the FLUENT simulations. Due to time and computational budget restrictions, only one y+ case was simulated in the UCNS3D code, the y+ = 15. The simulations took place for two different numerical schemes, an MUSCL scheme with a 2^{nd} order of accuracy and 3^{rd} order of accuracy WENO scheme. In order to capture the flow phenomena, especially the ones associated with turbulence, such as vortex sheddings and the contra rotational vortices in the wake region of the body, a density box was applied. Having a very small cell size for detailed analysis of the flow features and in such a size, so coverage of all the main flow patterns in the wake of the Ahmed body could be covered as it can be seen in Fig. 91, the density box captured properly the ongoing phenomena in the aforementioned area.

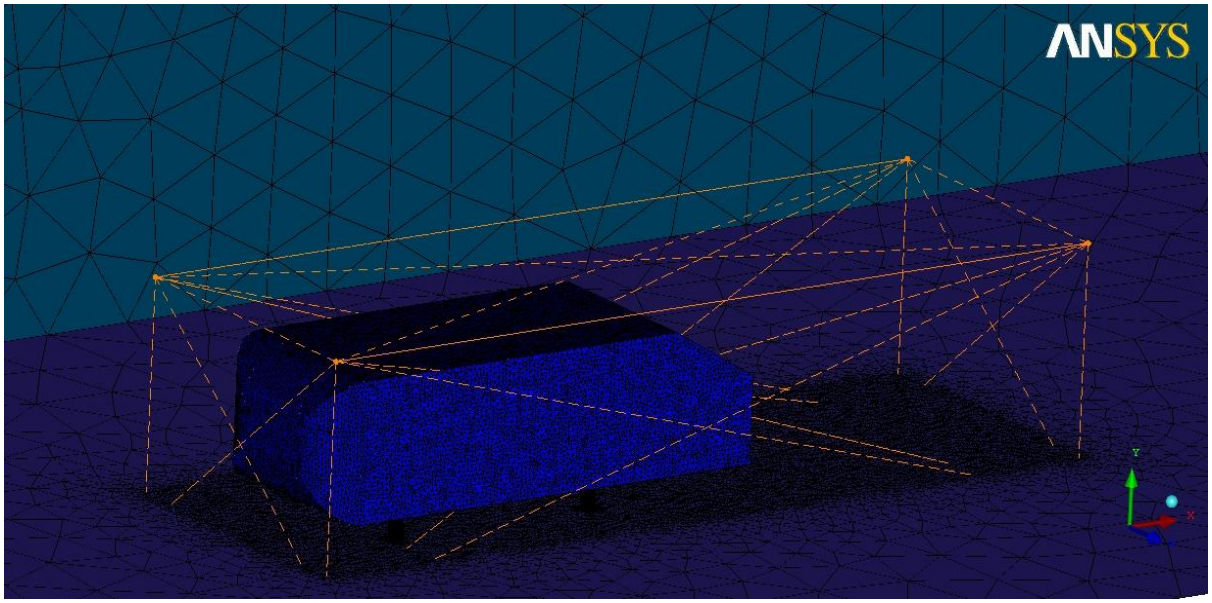

Fig. 91: Density box applied in all the grids used for the 3D simulations of the Ahmed body. Here, in the *30^o* slant angle (original) case

In Tables 22 – 24 analytical information about the creation of the grids and their composites can be found for each case simulated. It is of great importance to note here, than due to a special wall treatment existing for low y+ numbers in the region of $1 \leq y+ \leq 30$ in FLUENT, allowing the application of the turbulence model independent of the near wall y+ resolution, a minimum number of 10 layers had to be applied to the prism layers created in order for the aforementioned wall treatment to take effect. Additionally, the UCNS3D code did not contain any feature of this sort in connection to the wall treatment.

30^o Slant Angle	Total Nodes	Total Elements (Cells)	Prism Elements (TRI_3)	Quadrilateral Elements (TETRA_4)
y^+ 1 (Fine)	1380404	5261005	84177	3703617
y^+ 5 (Medium)	1053724	4299458	64289	3253266
y^+ 15 (Coarse)	904551	3995551	64796	3243438

Table 22: Statistics for the three different 3D grids created for the 30^o slant angle

25^o Slant Angle	Total Nodes	Total Elements (Cells)	Prism Elements (TRI_3)	Quadrilateral Elements (TETRA_4)
y^+ 1 (Fine)	1324787	4948510	64311	3416931
y^+ 5 (Medium)	1024336	4123799	64458	3077532
y^+ 15 (Coarse)	875642	3823286	64405	3071348

Table 23: Statistics for the three different 3D grids created for the subcritical 25^o slant angle

35^o Slant Angle	Total Nodes	Total Elements (Cells)	Prism Elements (TRI_3)	Quadrilateral Elements (TETRA_4)
y^+ 1 (Fine)	1205194	4244975	62702	2718801
y^+ 5 (Medium)	920984	3509737	63038	2465448
y^+ 15 (Coarse)	785551	3287769	77567	2525202

Table 24: Statistics for the three different 3D grids created for the supercritical 35^o slant angle

5.3.1 Ahmed Body 30^o, 25^o, 35^o Slant Angles

As in the 2D cases and EQ. 82, the y+ factor is represented as a dimensionless distance for wall – bounded flows. The discrimination of the grids, is again y+ = 1 for a fine grid, y+ = 5 and y+ = 15 for medium and coarse grids, respectively. In Fig. 92 – 94, the grids with a focus on the slant angle can be observed, for each slant angle case. The clustered, more detailed cells inside the density boxes, are apparent.

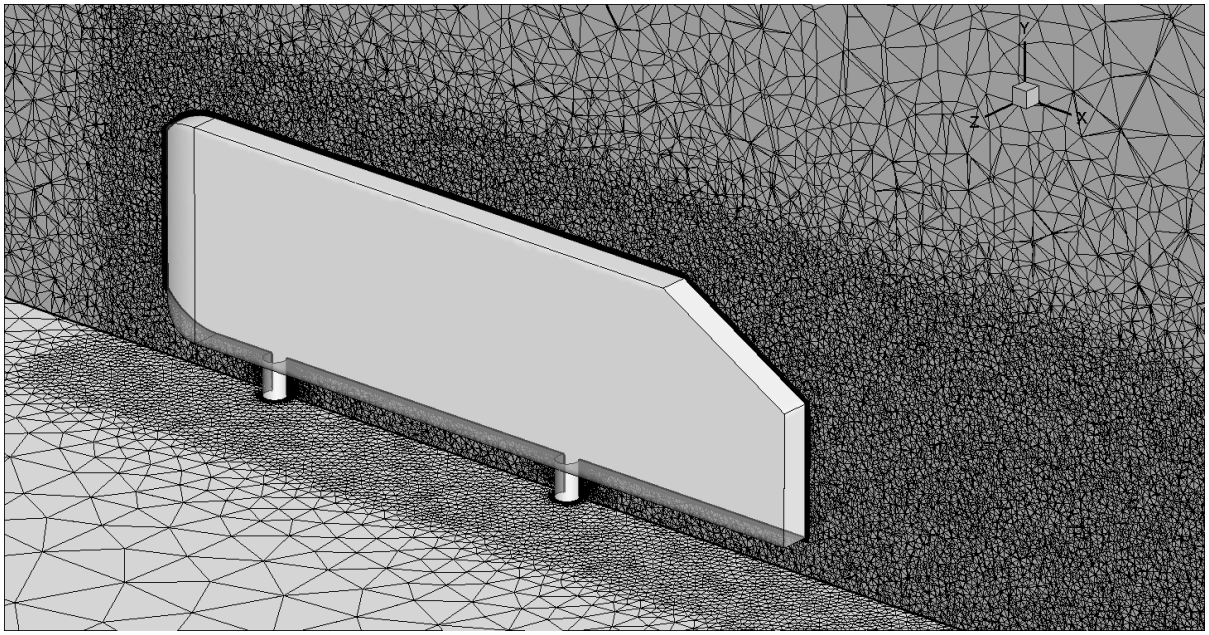

Fig. 92: Close capture of the slant angle for the 30^{o} slant angle case

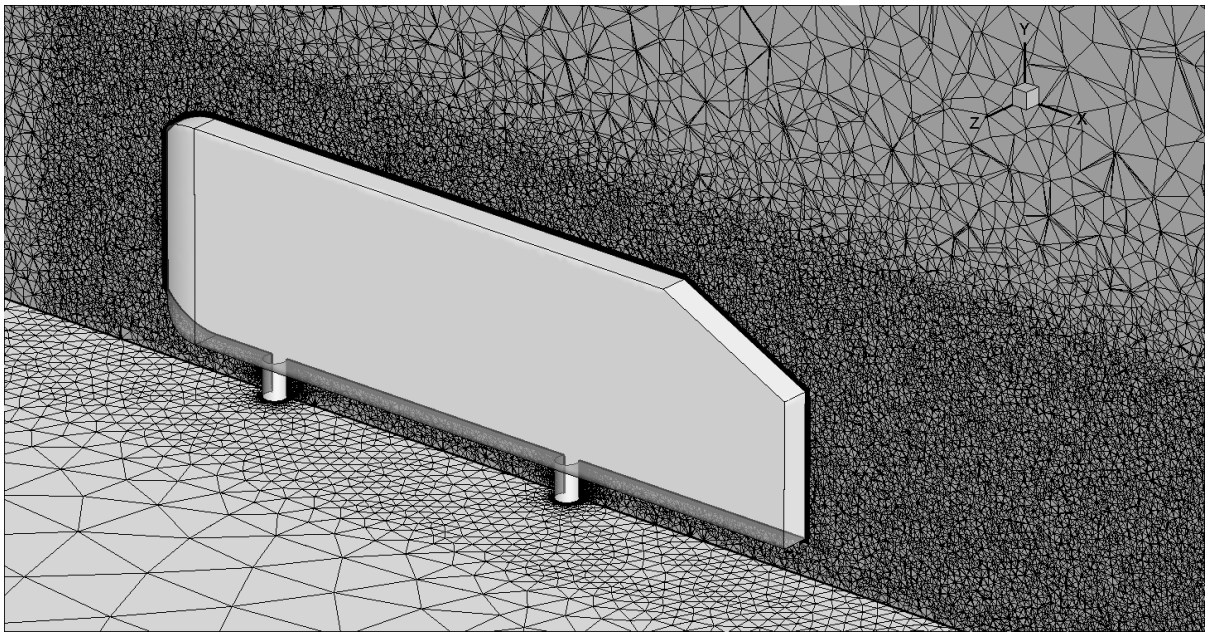

Fig. 93: Close capture of the slant angle for the 25^{o} slant angle case

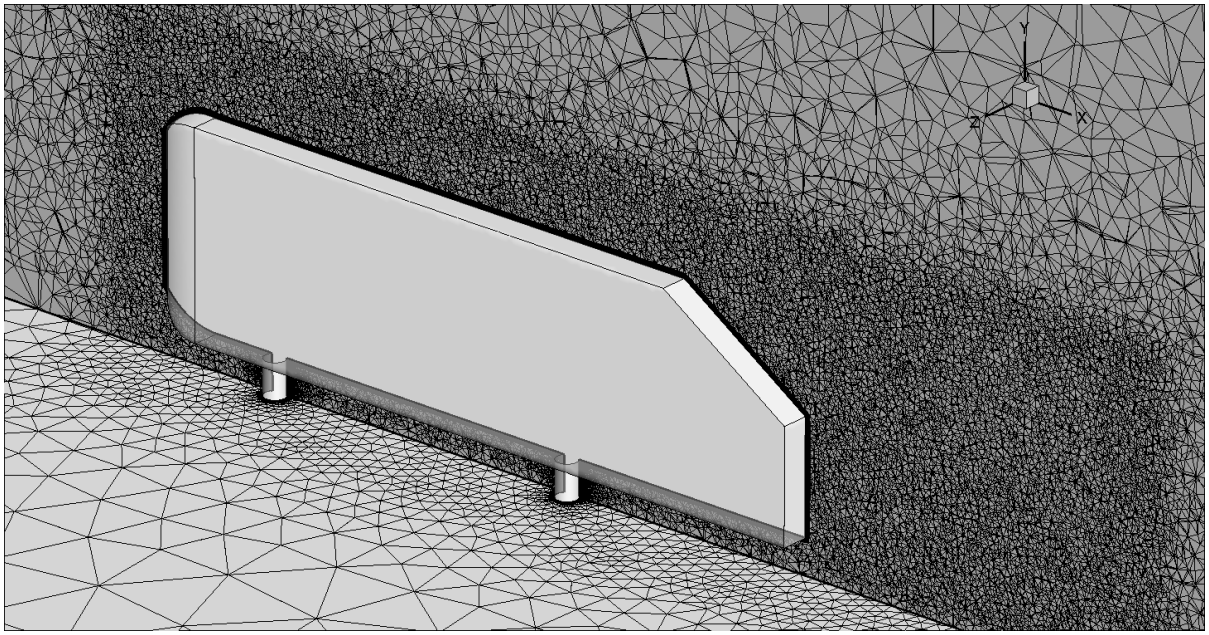

Fig. 94: Close capture of the slant angle for the 35^{o} slant angle case

5.3.2 Structured Grid Extrusion Details in 3D Cases

As mentioned in chapter 5.3, due to a sensitive wall treatment in the Spalart – Allmaras turbulence model in FLUENT, the minimum number of layers in the structured grid of the boundary layer around the bluff body, was 10. The structured grid extrusion details can be seen in Tables 25 – 27. The grids were created in ICEM and the orthogonal quality feedback from FLUENT for each grid, can be seen.

30^o slant angle

	$y^+ = 1$	$y^+ = 5$	$y^+ = 15$
Initial Δs (Height)	0.00095	0.00475	0.01472
Height Ratio	1.175	1.175	1.175
Number of layers	30	20	14
Total height	0.679777	0.6558439	0.69813597
Quality	$1.378x10^{-2}$	$5.44x10^{-2}$	$5.13x10^{-2}$

Table 25: Details of the structured grid extrusion for the 30^o slant angle

For convenience reasons and in order to make comparison between results of the various cases easier, there was an effort to maintain similar numbers in the Height Ratio used, as well the Total Height among the same y+ cases in all the slant angles used. These Total Height values for the structured grid, were 0.679777 for the y+1 cases and 0.6558439 with 0.698136 for the y+5 and y+15 cases, respectively.

25^{o} slant angle

	$y^{+} = 1$	$y^{+} = 5$	$y^{+} = 15$
Initial Δs (Height)	0.00095	0.00475	0.01472
Height Ratio	1.175	1.175	1.175
Number of layers	30	20	14
Total height	0.679777	0.6558843	0.698136
Quality	$1.319x10^{-2}$	$5.78x10^{-2}$	$4.02x10^{-2}$

Table 26: Details of the structured grid extrusion for the 25^{o} subcritical slant angle

35^{o} slant angle

	$y^{+} = 1$	$y^{+} = 5$	$y^{+} = 15$
Initial Δs (Height)	0.00095	0.00475	0.01472
Height Ratio	1.175	1.175	1.175
Number of layers	30	20	14
Total height	0.679777	0.6558843	0.698136
Quality	$1.242x10^{-2}$	$4.16x10^{-2}$	$6.77x10^{-2}$

Table 27: Details of the structured grid extrusion for the 35^{o} supercritical slant angle

5.4 Simulation Results in FLUENT and UCNS3D

In order to attempt comparison with both the previous 2D cases and directly with the solver configuration applied in the UCNS3D solver, the configuration in FLUENT was the following:

I.) Solver was density – based, time – steady, with absolute velocity formulation (compressible, non – transient solver configuration)
II.) The turbulence model used was a 1 equation, Spalart – Allmaras strain/vorticity based, with the energy equation set to be solved, as well
III.) Inflow velocity of 40 m/s
IV.) Implicit solution method
V.) The CFL condition for all the cases was the default in FLUENT CFL = 5 (UCNS3D uses an explicit scheme, not allowing fluctuation of the CFL condition).

The solutions in the 3D geometries did not manage to converge, mostly due to the unsteady nature of the problem and the highly oscillatory profile exhibited in the residuals. Further analysis will follow in the upcoming chapters.

5.4.1.1 Ahmed Body 30^o Slant Angle in FLUENT and UCNS3D

In Table 28, the drag and lift coefficient values obtained with the aforementioned configuration can be seen, for the 3D geometries in FLUENT.

y+ factor	C_D (Drag Coefficient)	C_L (Lift Coefficient)
y+ 1 CFL = 5	0.325	0.058
y+ 5 CFL = 5	0.01	0.2495
y+ 15 CFL = 5	0.035	0.298

Table 28: Drag and Lift coefficient results for all the grids used for the Ahmed Body with a 30^o slant angle for FLUENT

Table 29 exhibits the values obtained from the simulations that took place in UCNS3D.

y+ factor	C_D (Drag Coefficient)	C_L (Lift Coefficient)
y+ 15 MUSCL 2nd Order CFL = 1	0.0414	0.079
y+ 15 WENO 3rd Order CFL = 1	0.0433	0.0588

Table 29: Drag and Lift coefficient results for all the grids and numerical schemes used for the Ahmed Body with a 30^o slant angle for UCNS3D

It should be denoted for Table 28, that the difference in the drag coefficient values are owed to the fact that the simulations for the y+1 case took place with a pressure – based (incompressible) solver. This selection was made mostly due to shortage of available time in conjunction with the additional time needed to solve the problem with compressible equations, as well as extended queues in the Astral HPC unit.

5.4.1.2 30º Slant Angle Contours and Plots

Fig. 95 exhibits the contours of velocity magnitude for the FLUENT simulations. In Fig. 96, the turbulent viscosity of the 30° slant angle case can be seen.

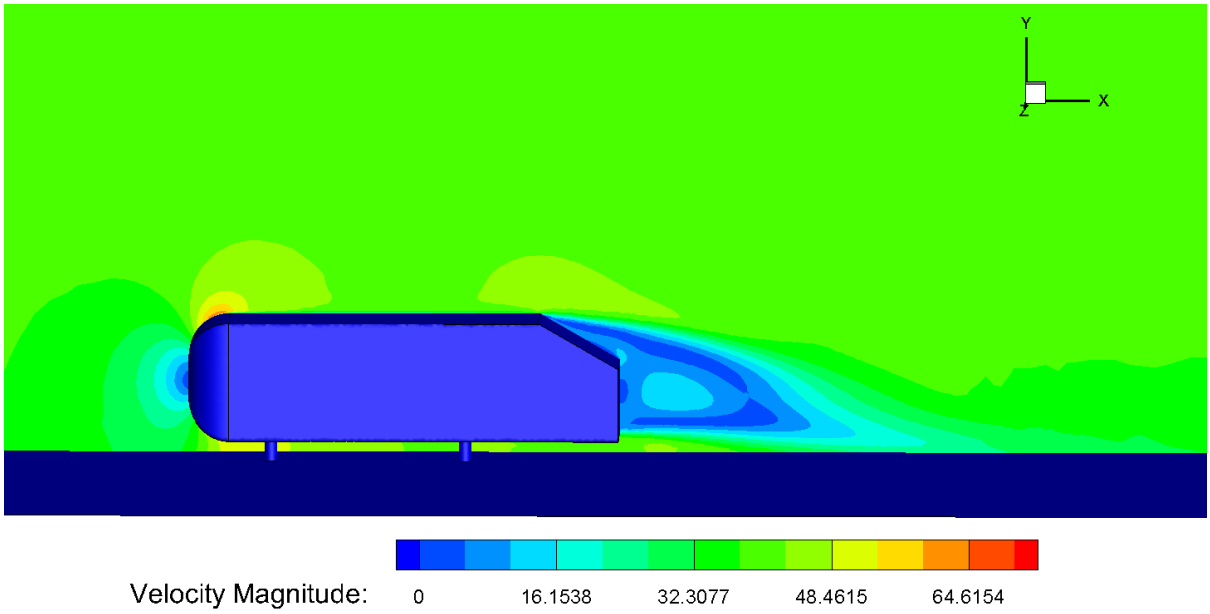

Fig. 95: Contours of velocity magnitude for the *30°* slant angle case

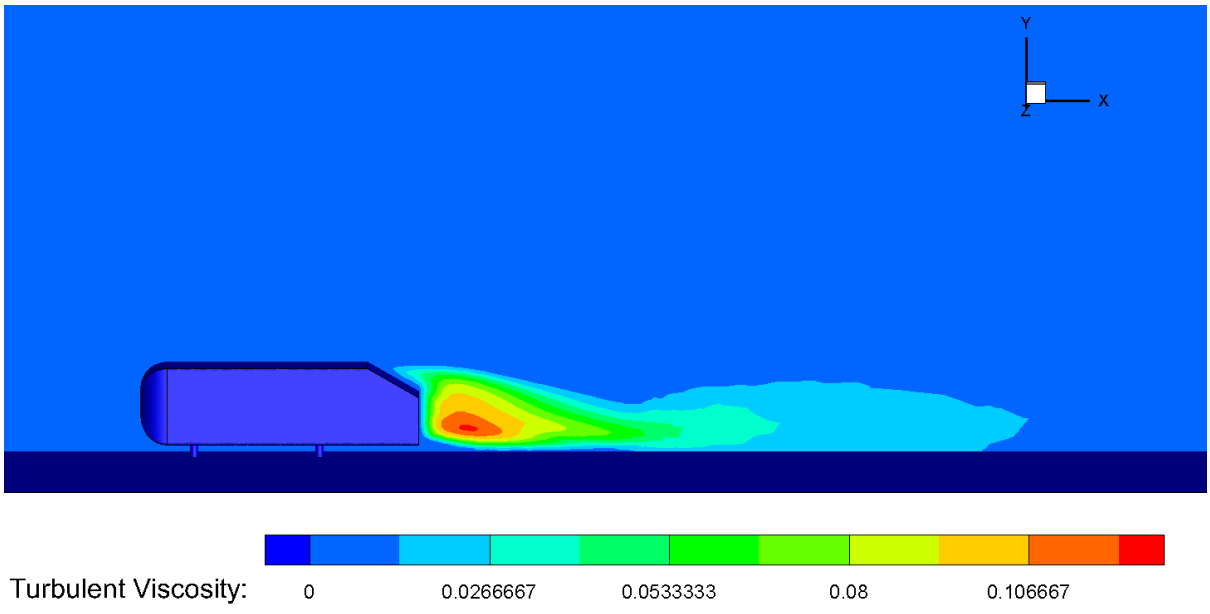

Fig. 96: Contours of turbulent viscosity for the *30°* slant angle case

Maximum turbulent viscosity was equal to 0.12, something which came in accordance with the 2D results. The separation bubble in the back was depicted properly in the contours of the velocity magnitude as exhibited in the streamtraces of the wake region in Fig. 97.

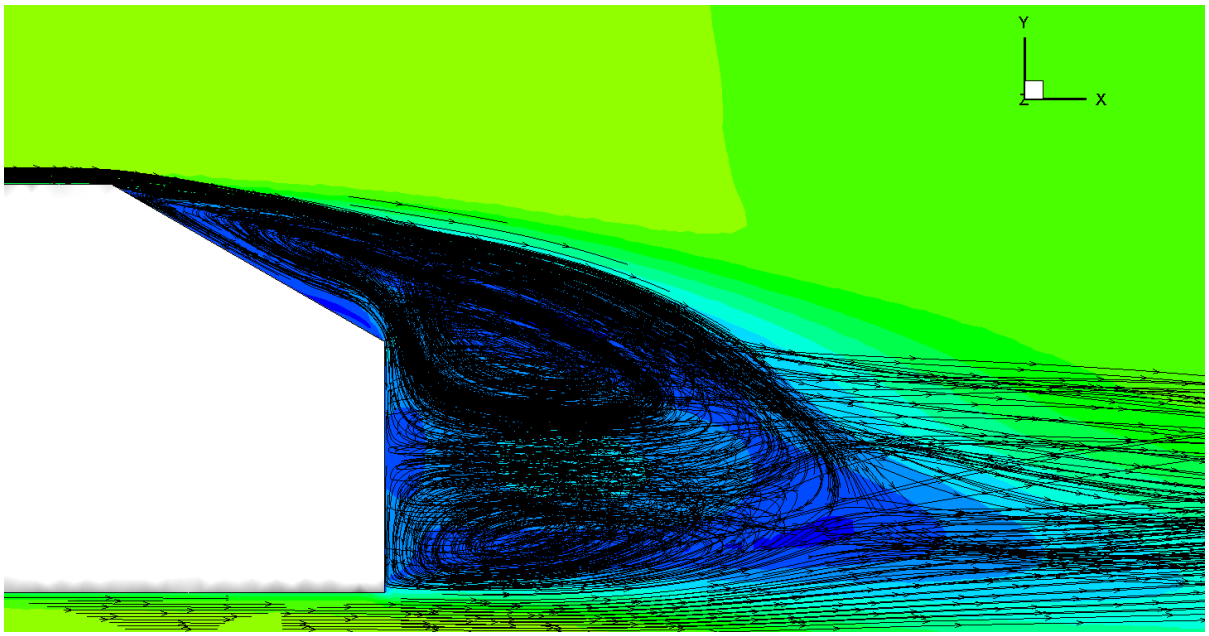

Fig. 97: Streamtraces in the wake region for the 30^o slant angle case in FLUENT

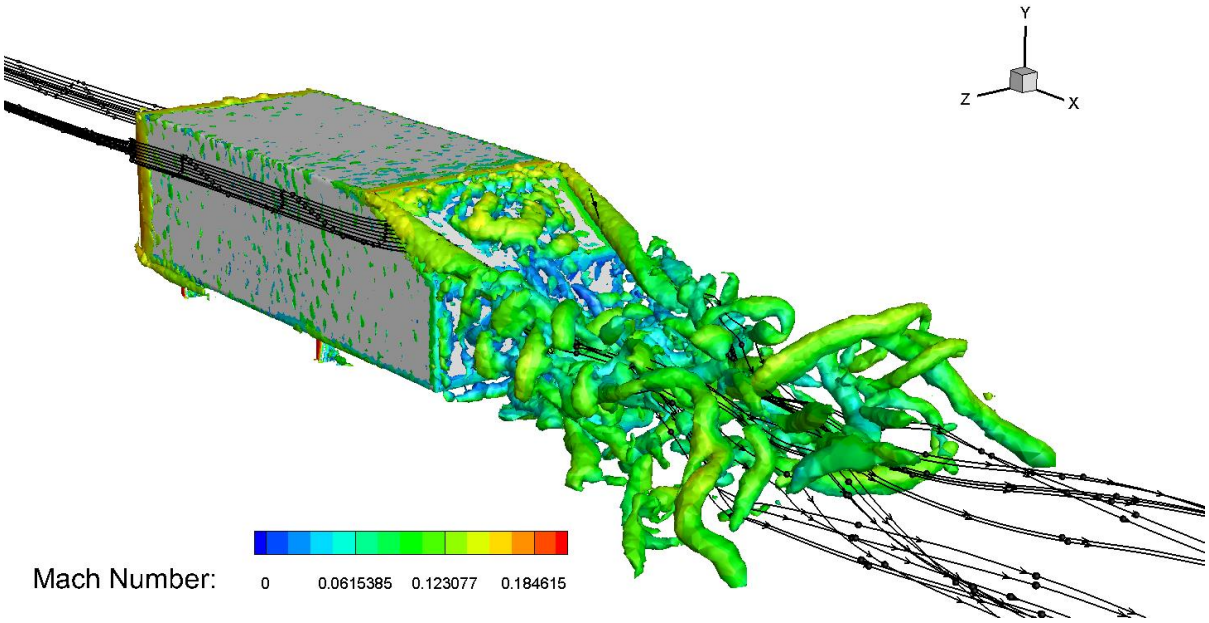

Fig. 98: Isosurfaces of Q – criterion colored by Mach number for the 30^o slant angle case in UCNS3D

In Fig. 98, the isosurfaces of Q – criterion can be seen in order to visualize the vortices appearing in the UCNS3D simulations, colored by Mach number. Fig. 99 is exhibiting the isosurfaces of eddy (turbulent) viscosity ratio, colored according to Mach number, as well. A flow separation is apparent in the slant angle, as well three separations in the middle of the body, one in the upper part and two in the left and right side of the body, respectively. The maximum value of turbulent viscosity was equal to ≈0.12, making this the second most rigorous case in terms of turbulence, next to the 35^{o} slant angle case.

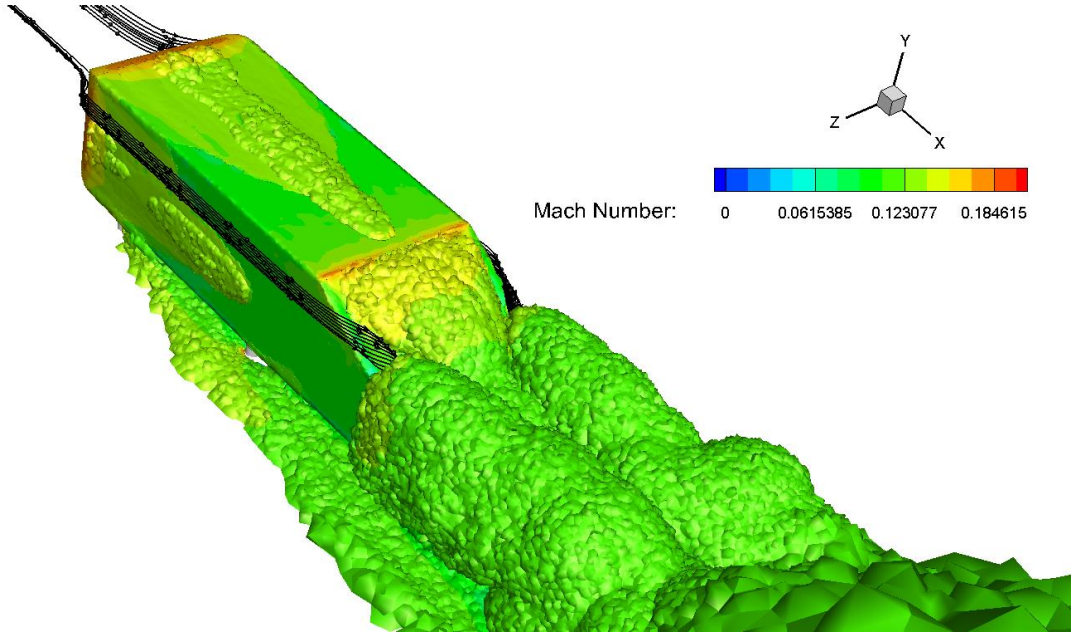

Fig. 99: Isosurfaces of eddy (turbulent) viscosity ratio colored by Mach number for the 30^{o} slant angle case in UCNS3D

5.4.2.1 Ahmed Body 25^o Slant Angle in FLUENT and UCNS3D

In Table 30, the drag and lift coefficient values obtained with the aforementioned configuration can be seen, for the 3D geometries in FLUENT.

y+ factor	C_D (Drag Coefficient)	C_L (Lift Coefficient)
y+ 1 CFL = 5	0.322	0.174
y+ 5 CFL = 5	-0.04	0.218
y+ 15 CFL = 5	0.034	0.3023

Table 30: Drag and Lift coefficient results for all the grids used for the Ahmed Body with a 25^o slant angle for FLUENT

Table 31 exhibits the values obtained from the simulations that took place in UCNS3D.

y+ factor	C_D (Drag Coefficient)	C_L (Lift Coefficient)
y+ 15 MUSCL 2nd Order CFL = 1	0.0423	0.064
y+ 15 WENO 3rd Order CFL = 1	0.0416	0.0498

Table 31: Drag and Lift coefficient results for all the grids and numerical schemes used for the Ahmed Body with a 25^o slant angle for UCNS3D

As in the 30^o slant angle case, the difference in the drag coefficient values in the y+ = 1 case, are owed to the fact that the simulations for this particular case took

place with a pressure – based (incompressible) solver and the selection is justified by the same reasons, as in the previous case.

5.4.2.2 25º Slant Angle Contours and Plots

Fig. 100 exhibits the contours of velocity magnitude for the FLUENT simulations. In Fig. 101, the turbulent viscosity of the 25° slant angle case can be seen. TV = 0.10852

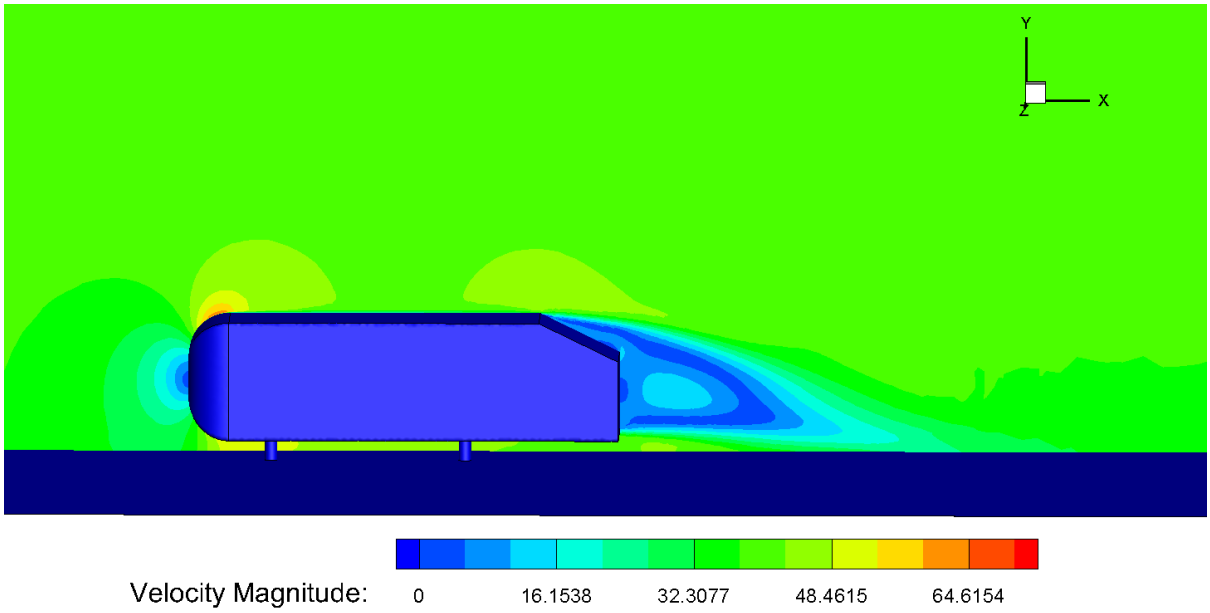

Fig. 100: Contours of velocity magnitude for the *25°* slant angle case

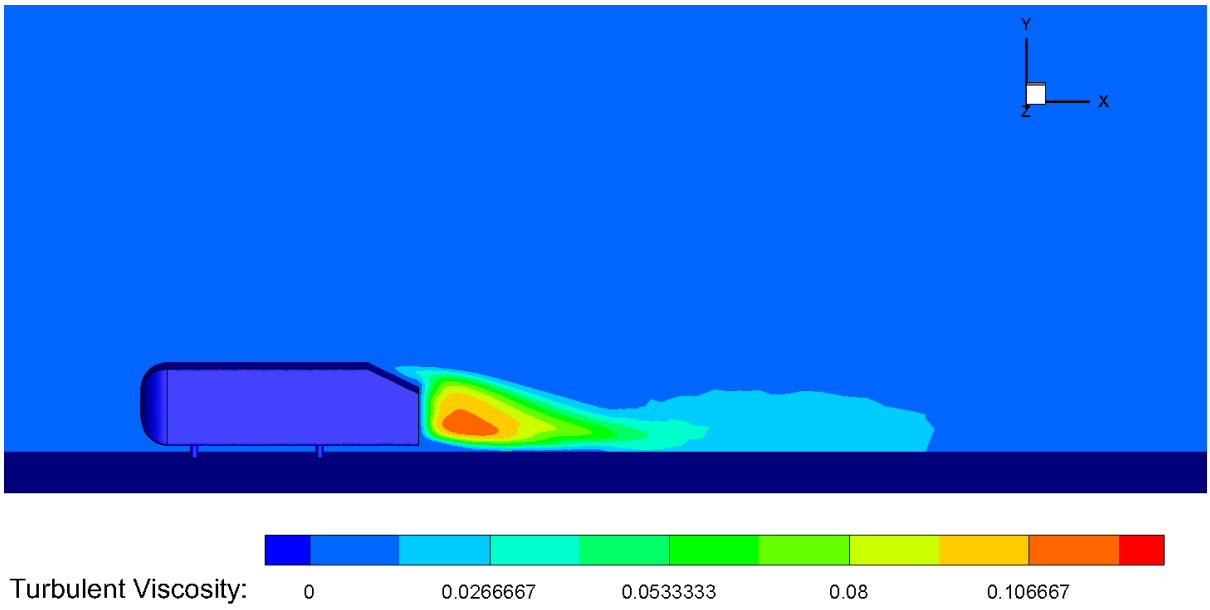

Fig. 101: Contours of turbulent viscosity for the *25°* slant angle case

Visualization of the results from the UCNS3D simulations with post – processing in Tecplot can be seen in Fig. 102 and Fig. 103, for the Q – criterion (visualization of vortices) and turbulent viscosity ratio, respectively, both colored according to the Mach number. It is apparent in Fig. 103 that vortex shedding in the slant angle is not that rigorous as in the rest of the cases.

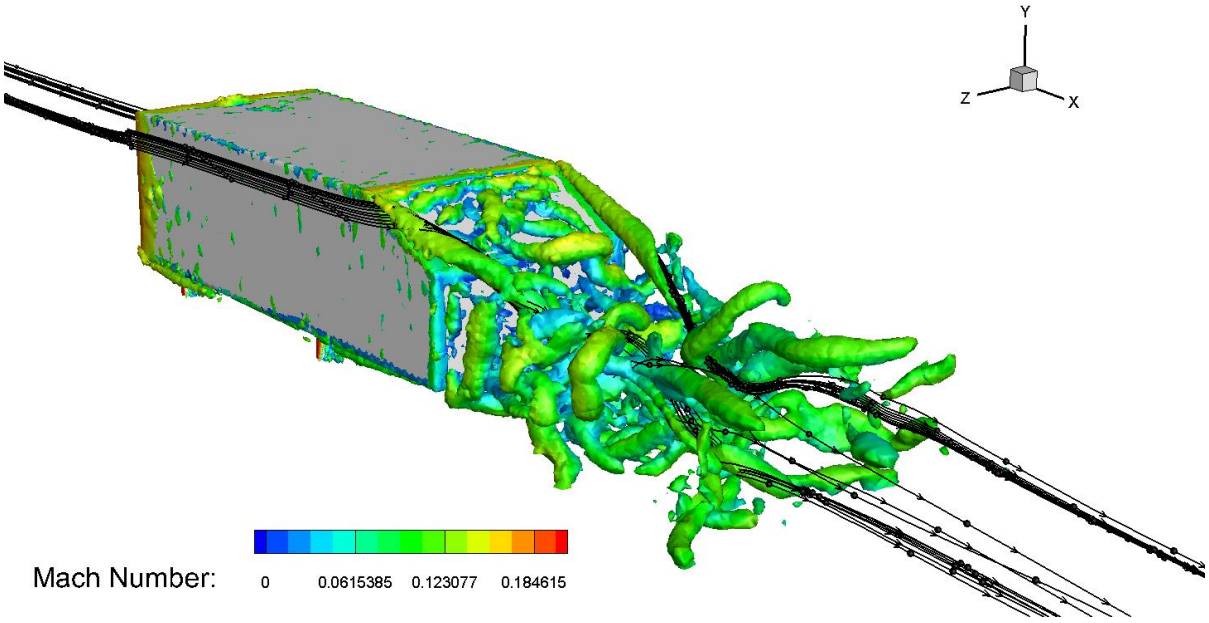

Fig. 102: Isosurfaces of Q – criterion colored by Mach number for the 25^o slant angle case

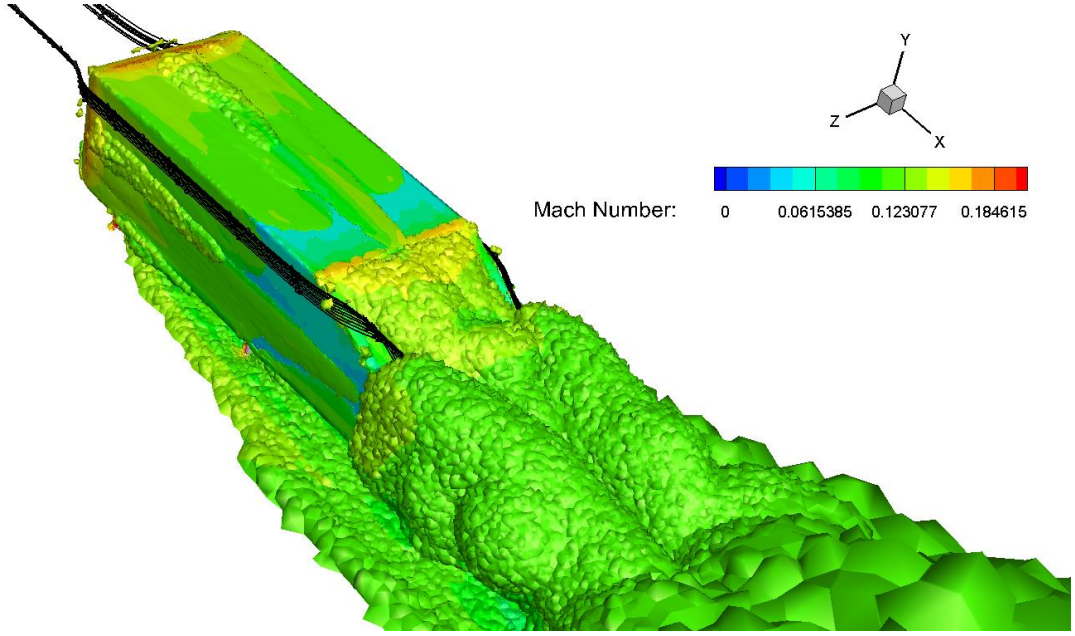

Fig. 103: Isosurfaces of eddy (turbulent) viscosity ratio colored by Mach number for the 25^o slant angle case

The difficulty of solving the problem, as well as the highly oscillatory nature of the residuals can be seen in Fig. 104 with the residuals of the 25^{o} slant angle case being exhibited. It is apparent, that after 167500 iterations, a repetitive residuals profile is shown and the solution does not indicate possible convergence, as the residual values are not dropping.

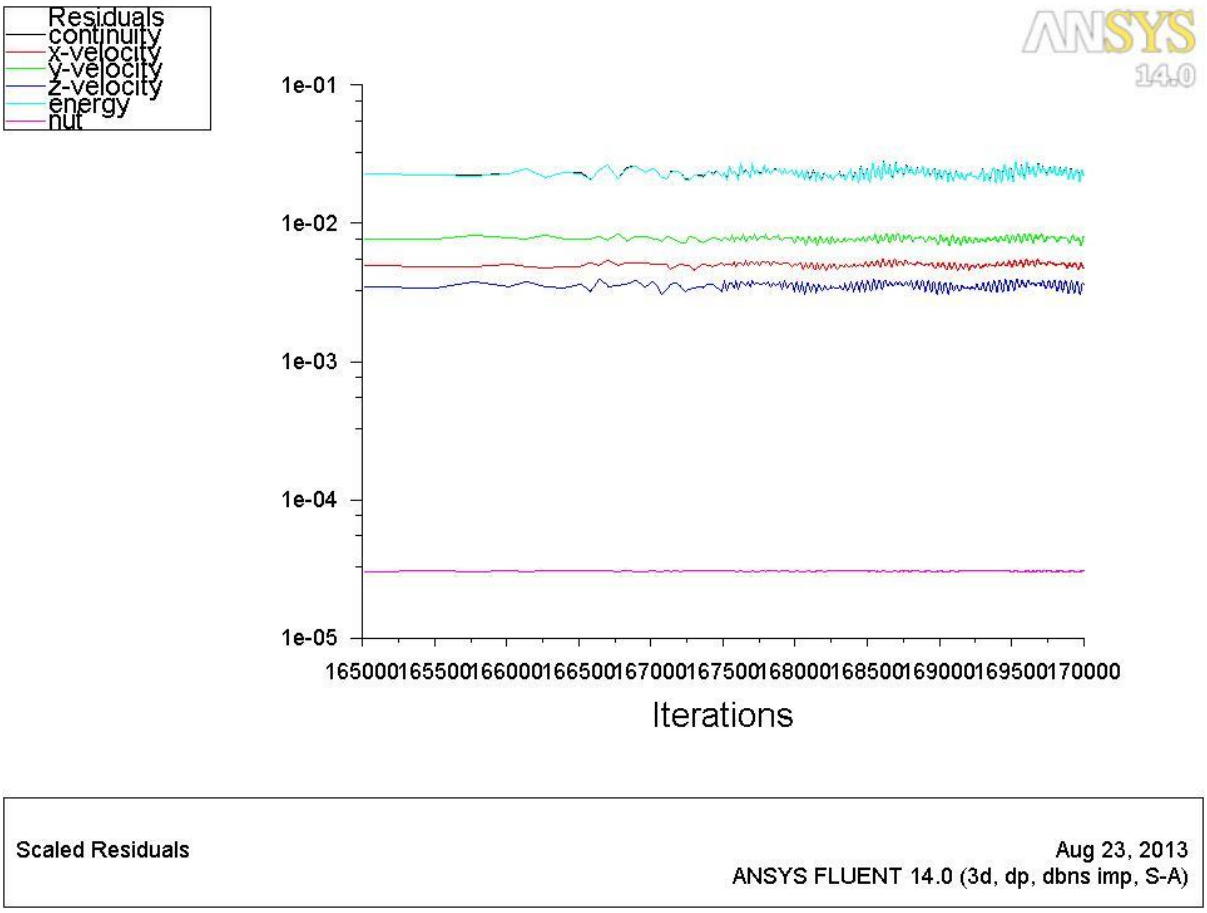

Fig. 104: Oscillations in residuals for the *25^{o}* slant angle case

5.4.3.1 Ahmed Body 35^{o} Slant Angle in FLUENT and UCNS3D

Table 32, exhibits the drag and lift coefficient values for the 3D geometries in FLUENT, obtained with the aforementioned configuration.

y+ factor	C_D (Drag Coefficient)	C_L (Lift Coefficient)
y+ 1 CFL = 5	0.325	0.0631
y+ 5 CFL = 5	0.214	0.2289
y+ 15 CFL = 5	0.035	0.2951

Table 32: Drag and Lift coefficient results for all the grids used for the Ahmed Body with a 35^{o} slant angle for FLUENT

Table 33 exhibits the values obtained from the simulations that took place in UCNS3D.

y+ factor	C_D (Drag Coefficient)	C_L (Lift Coefficient)
y+ 15 MUSCL 2nd Order CFL = 1	0.0424	0.091
y+ 15 WENO 3rd Order CFL = 1	0.0538	0.0645

Table 33: Drag and Lift coefficient results for all the grids and numerical schemes used for the Ahmed Body with a 35^{o} slant angle for UCNS3D

In accordance with the rest of the y+ = 1 cases examined in this study, the y+ = 1 case in the 35^{o} slant angle, was simulated as well, with a pressure – based (incompressible) solver.

5.4.3.2 35º Slant Angle Contours and Plots

The contours of velocity magnitude for the FLUENT simulations, are exhibited in Fig. 105, while the turbulent viscosity of the 35° slant angle case can be seen in Fig. 106.

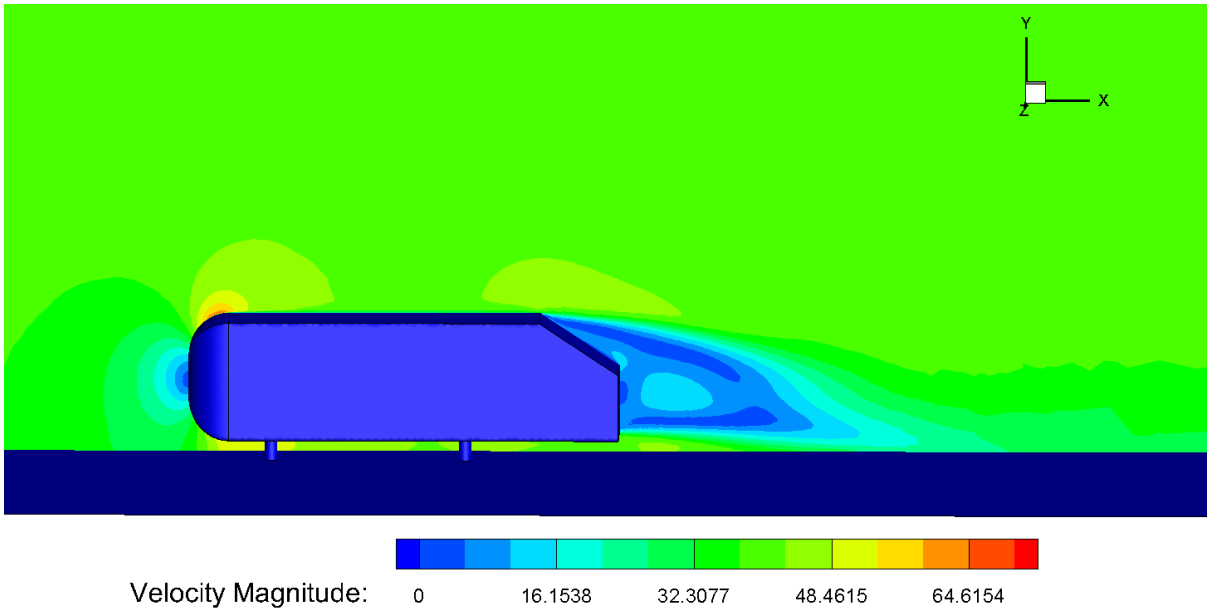

Fig. 105: Contours of velocity magnitude for the *35°* slant angle case

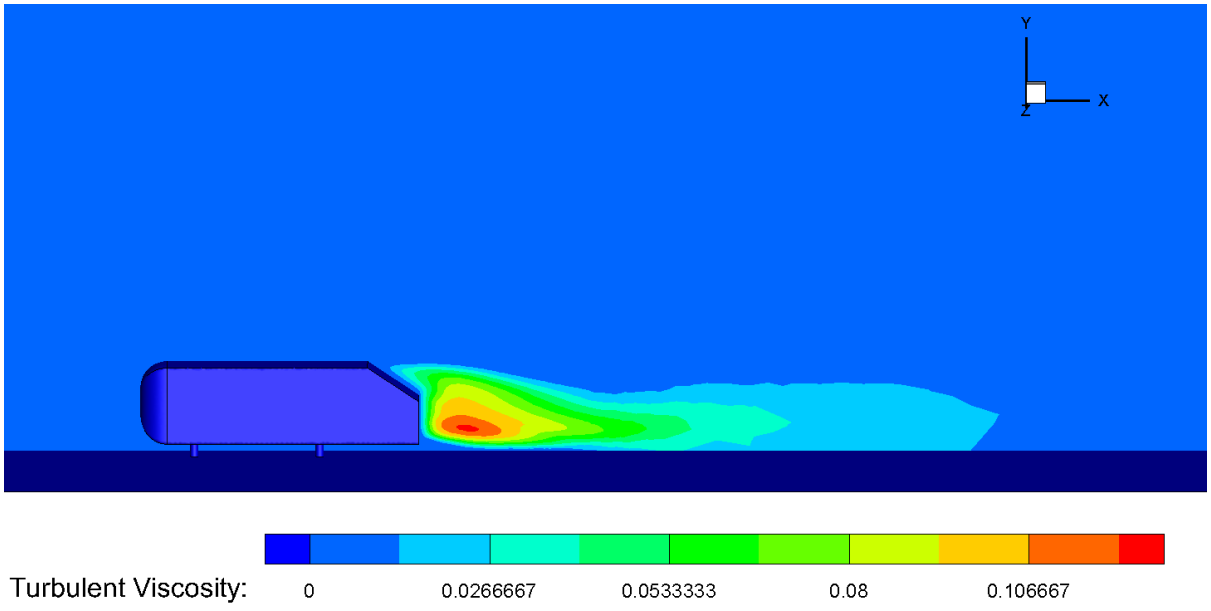

Fig. 106: Contours of turbulent viscosity for the *35°* slant angle case

The same phenomena in the flow separation bubble as in the 2D cases, are apparent in the 3D geometries. The separation bubble and the vortex sheddings exhibited are the most rigorous of all the cases examined resulting in a value for turbulent viscosity equal to 0.12, which is one of the higher values examined. The aforementioned can be observed in Fig. 107 and Fig. 108 which exhibit the results from the UCNS3D simulations for the Q – criterion and turbulent viscosity ratio.

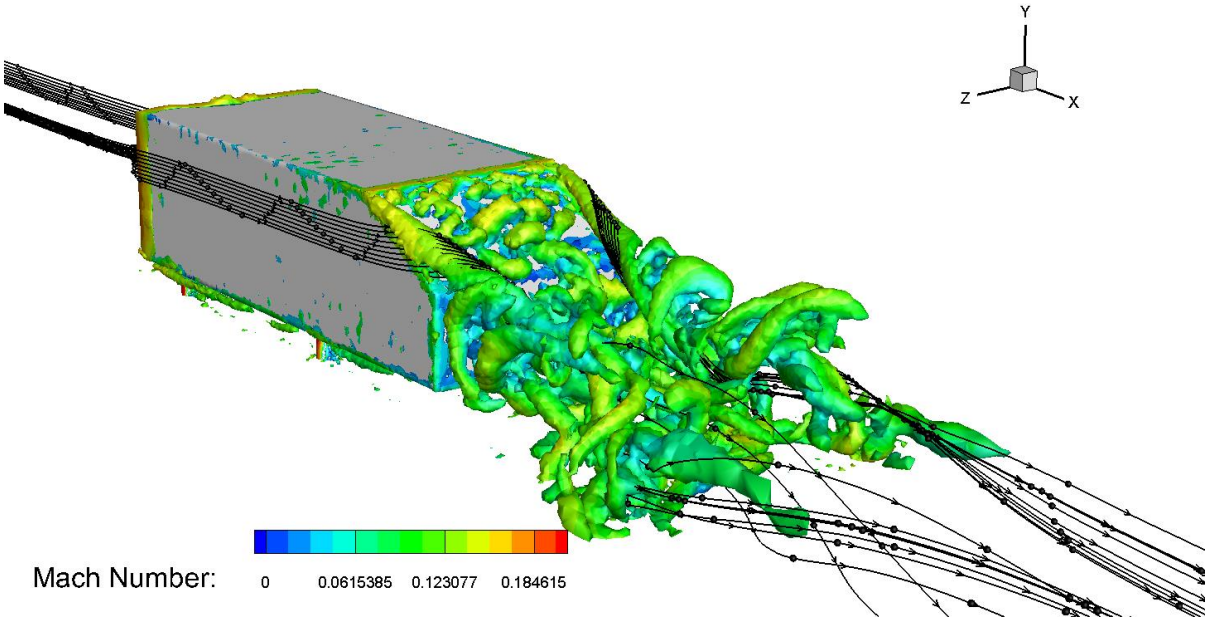

Fig. 107: Isosurfaces of Q – criterion colored by Mach number for the 35^o slant angle case in UCNS3D

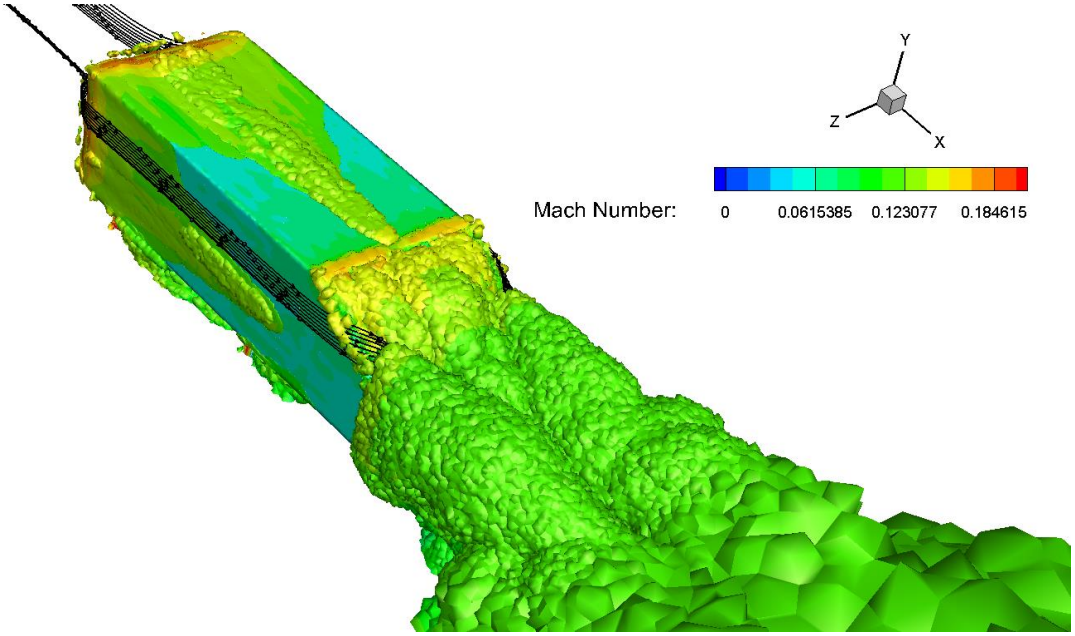

Fig. 108: Isosurfaces of eddy (turbulent) viscosity ratio colored by Mach number for the 35^o slant angle case in UCNS3D

5.5 Cd and Cl Results in FLUENT and UCNS3D for the 3D Cases

5.5.1 Cd Results

The results obtained from the FLUENT simulations can be seen in Fig. 109.

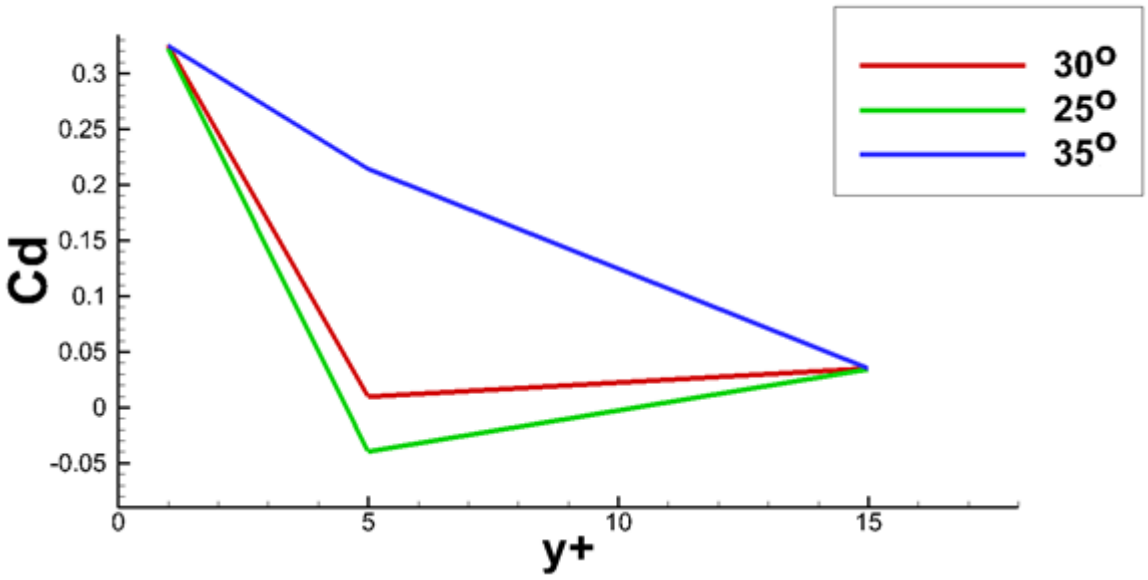

Fig. 109: Cd and y+ values from the results of the 3D simulations in FLUENT

It is observed from Fig. 109, that with an exception of the y+ = 1 cases which were run with an incompressible setup for the solver (pressure based), the rest of the values are unrealistic, even reaching negative values in the 25° slant angle case and the higher values are observed in the 35° slant angle case.

The results for the drag coefficient values obtained from the simulations run in the UCNS3D code with two different numerical schemes (MUSCL 2nd order and WENO 3rd order), can be found in Fig. 110.

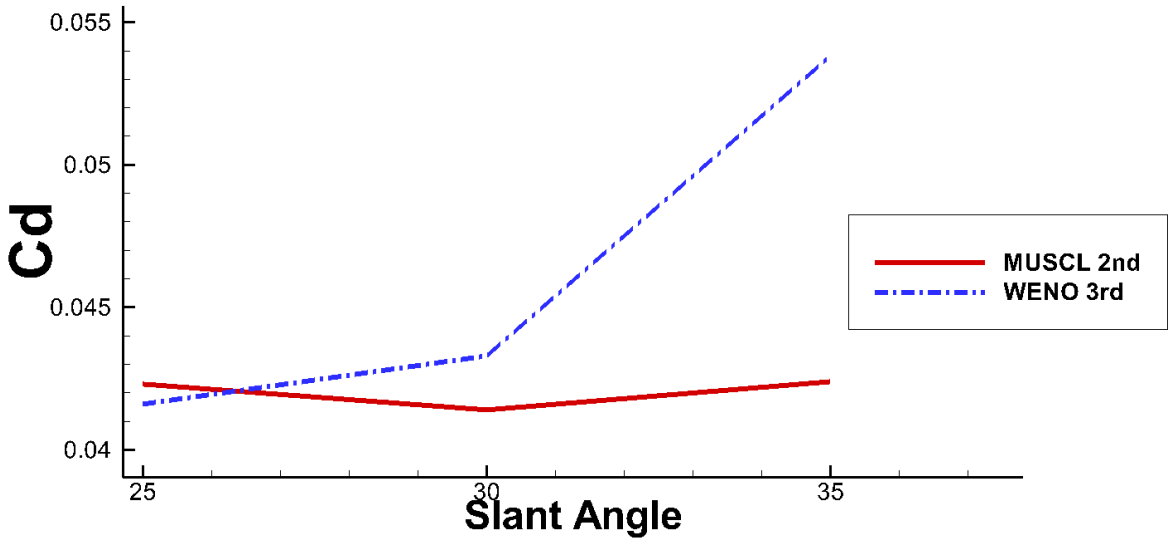

Fig. 110: Cd and slant angle values from the results of the 3D simulations in UCNS3D

It can be noticed that the cd values for the MUSCL scheme are fluctuating in a very small range and not many differences can be observed in the values, even between different slant angles. The WENO scheme is producing results in a more sensible manner, as the drag coefficient values rise with increasing the slant angle (the most intense phenomena are noticed in the 35^{o} slant angle case), yet they are far from being able to be ranging anywhere near the experimental.

5.5.2 Cl Results

The results obtained for the lift coefficient values in the simulation that took place in FLUENT, can be seen in Fig. 111. Fig. 112 displays the results for the lift coefficient produced by the simulations in UCNS3D.

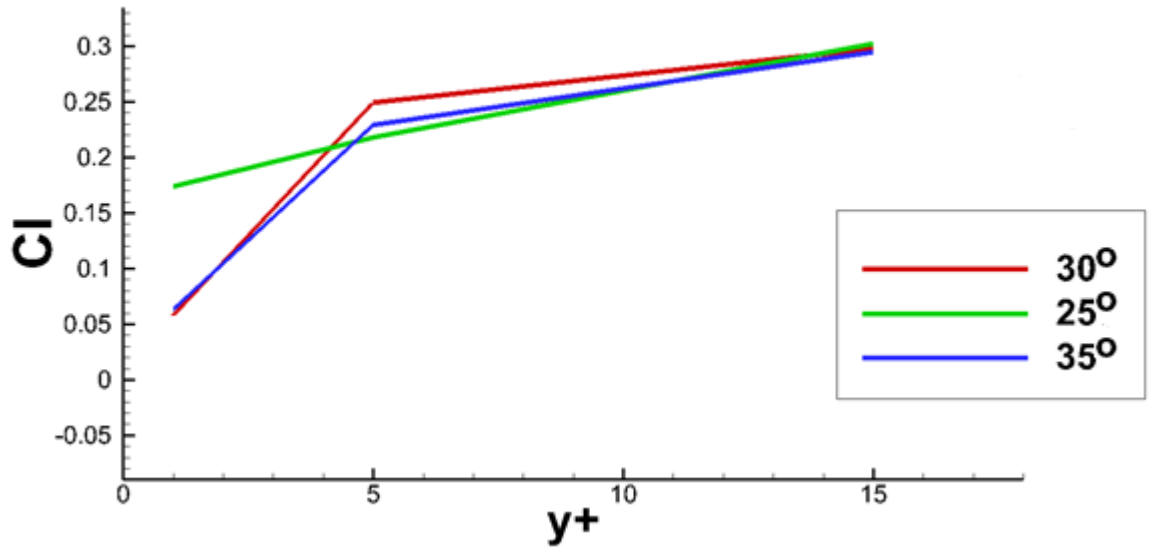

Fig. 111 Cl and y+ values from the results of the 3D simulations in FLUENT

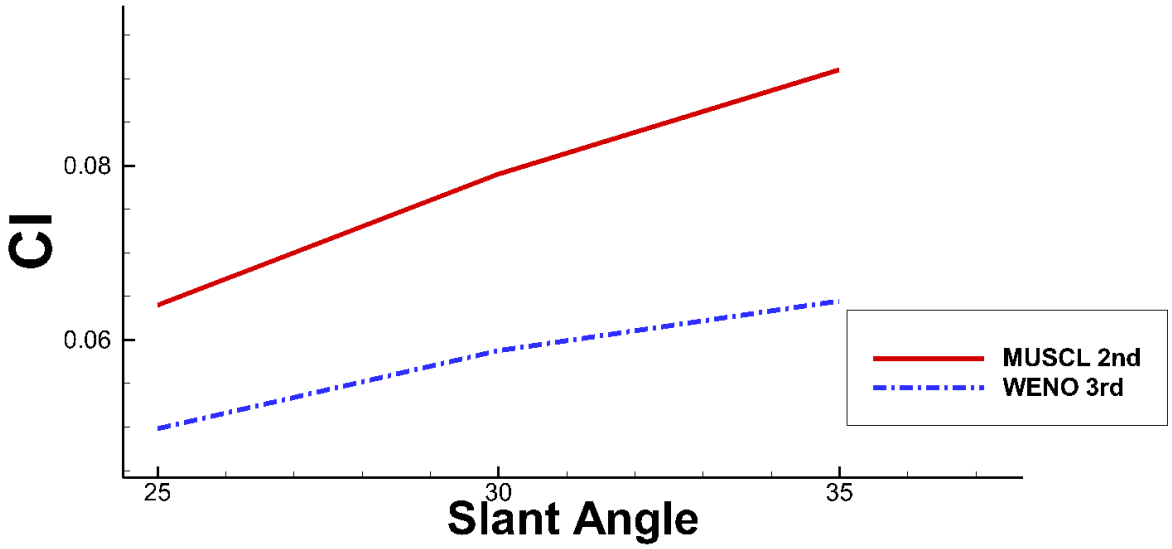

Fig. 112: Cl and slant angle values from the results of the 3D simulations in UCNS3D

As in the drag coefficient values and without the exception of the y+ = 1 cases, the lift coefficient values are again unrealistic and range in a completely different region than the experimental, which are more than double the highest value obtained (25^{o} slant angle case with y+ = 15). The simulations in UCNS3D exhibited a tendency for the lift coefficient values to rise along with the slant angle. The values produced by FLUENT, in comparison with both the corresponding ones in the MUSCL and WENO schemes, had a better level of accuracy, however their range was far off from being anywhere close to the experimental ones.

5.6 Conclusions for the 3D Cases

The Ahmed body geometry was simulated in a commercial solver (FLUENT) with a 2^{nd} order of accuracy solver for various grid configurations and the inhouse developed UCNS3D code using MUSCL 2^{nd} and WENO 3^{rd} order of accuracy schemes, a y+ = 15 grid configuration. The turbulence model used, was one equation Spalart – Allmaras in a compressible configuration (strain / vorticity based) in order to test the aforementioned solver configurations in extreme conditions (very low Mach number – Mach = 0.11). The aim was to test the results returned, both with the experimental in order to conclude about their realism and the robustness of the UCNS3D code as well, in comparison with a commercially available and widely acclaimed solver, such as FLUENT. In terms of realism of values, the results obtained are nowhere near the experimental in all the cases, except for the drag coefficients in the y+1 FLUENT cases, that were run with an incompressible setup for convenience reasons, mostly associated with restrictions in the available time, deriving from large queues in the ASTRAL HPC unit. As a result of the aforementioned, it is apparent that the compressible solver setup for such a case, besides consisting a slower approach due to the extra terms contained in the computations taking place, poses an unsuitable solution as well, as it presents unrealistic results. The RANS equations solved with Spalart – Allmaras turbulence model, exhibit a highly oscillatory behavior in the residuals and convergence was not achieved in any of the cases. Additionally, this particular turbulence model proved a weakness in capturing the rigorous vortex sheddings, vortices and various discrepancies taking place in the slant angle and wake region of the Ahmed body, thus proving it's unsuitable for modeling turbulence in large flow separations, such as these exhibited in the cases examined. In the simulations taking place in FLUENT, the highest order of schemes (MUSCL 3^{rd} order) was not used, as the purpose of this study was to study high resolution schemes (with the ability to resolve all wavenumbers in a given mesh), which comprise mostly of 2^{nd} order schemes without oscillations which focus on unsteady flow phenomena, in an effort to achieve smaller errors with lower order of accuracy for the same grid configurations, in comparison with the higher order schemes used in the UCNS3D simulations.

The phenomena were more intense in the 35^{o} slant angle case and softer in the 25^{o} slant angle case, implying an association with the slant angle (more rigorous phenomena in greater angles), as the turbulent viscosity values were rising along with the slant angle. The drag and lift coefficient values obtained from both FLUENT and UCNS3D are ranging in the same region for all the y+5 and y+15 cases in both solvers, which points that in terms of accuracy the schemes used are very close between these two solvers, however they are greatly diverging from the experimental ones. This conclusion is not valid however for the drag coefficient values of the y+1 cases (simulated incompressible), as they are quite close to experimental values of ≈0.3, but the lift coefficient values of these cases nonetheless were greatly diverging from the

experimental, as well. From all of the aforementioned, the conclusion that the setup used to simulate the flow around the Ahmed body in this study, despite exhibiting some interesting features, further analysis of which might be the subject of further research, is not the suitable one for this type of flow and did not produce realistic results to be based upon.

If a conclusion was to be made in order to make some useful remarks about the key findings of the 3D simulations in connection with the configurations used to simulate the flow around the Ahmed body, these would be the following:

I.) In connection with the Spalart – Allmaras turbulence model:

- The Spalart – Allmaras turbulence model is considered suitable for wall – bounded flows with a small flow separation. This model is effectively modeling turbulence in transonic flows or slightly separated flows (airfoils, nozzles, etc) or other complex commercial configurations, something which is not the case with the Ahmed body, clearly giving this turbulence model initially a handicap in simulating the Reynolds stress for automotive – type flows in comparison to other turbulence models, such as k – ε or k – ω. [83]
- Spalart – Allmaras solves a transport equation for the eddy viscosity and models its diffusion, production and destruction. Imposing wall boundary conditions and free stream are considered to be its advantages in comparison with k – ε [83], [84].
- The cpu time needed of the one – equation Spalart – Allmaras turbulence model is smaller than the cpu time needed for two – equation models such as k – ε or k – ω [82].
- Being a one – equation model, through solving the transport equation, only one of the turbulent scales is solved.
- Due to the nature of the flow around the Ahmed body and mostly associated with the shear flows exhibited, the strength of the turbulence model to produce turbulence from the mean shear flow is inadequate. As a result of that, low values of eddy viscosity are observed. The turbulence production is a function of the Reynolds number [86] The turbulence index (i_t) from Spalart and Allmaras, having a value of almost 1 in turbulent regions and near zero in laminar regions is a criterion for this sort of behavior.

II.) In connection with solving the Reynolds Averaged Navier – Stokes equations:

- As the results exhibited, for solving low Mach number flows and especially with strong density variation, the RANS compressible

equations are inadequate and not the appropriate type for computation, mostly due to the limitation concerning the small time step in the explicit methods by numerical stability requirements. As a result, these methods for solving practical flow problems, would require a vast amount of time [88].

- The accuracy of simulations taking place with solving the Navier Stokes is inextricably connected with accurately predicting the turbulent flow field and its main characteristics.
- This accuracy is further dependent on the closure of the RANS equations, the Reynolds tensor. It derives from the convective term of the Navier – Stokes equations and is constituted by the double correlation of the turbulent fluctuations. The computation of the Reynolds stress tensor and its accuracy is the task of the turbulence model [82].
- The basic challenges upon attempting successful turbulence prediction in aerodynamics applications are firstly the separation of the boundary layer and its growth, followed by the aftermath of the separation and the momentum transfer [87].
- The former makes demands of very high accuracy and gives little advantage to models of higher complexity but it's simpler while the latter is the basis for many complex RANS models and newer strategies according to which, even for 2D geometries, 3D time – dependent simulations are the norm. [87]
- The finer grid cases of y+ = 1 for all the geometries were used with the RANS models in order to resolve the boundary layer of the turbulent flow. A y+ = 1 distance for the first nodes is essential in order to better resolve the boundary layer. In order to numerically model a turbulent flow with RANS, a fine mesh is needed in the boundary layer [89].
- Extra effort was put in using necessary local grid refinements, such as the density boxes used around the Ahmed body in order to resolve the flow near singularities. In cases of unstructured meshes, considerable constraints are imposed on the mesh generator by these requirements [89].
- In critical zones of the flow (such as the ones having a locally high Peclet number or in areas with steep gradients) in order to stabilize the solution, numerical dissipation is essential. The same method is used for values such as turbulent viscosity and pressure in order to preserve positivity [89].
- One of the RANS simulations drawbacks is that the turbulence scales are modeled instead of being resolved due to the large diversity of time and space scales, something which offers a significant gain in computational

budget, however, the final solution of the problem is compromised and may produce misleading results [83].

III.) In connection with the Higher – order schemes used:

- In order to simulate flows with complex patterns in their solution such as these presented in the case of the Ahmed body, higher order methods are essential for proper resolution.
- In terms of balancing between simplicity of code, computational budget and the demanded resolution in results, an adequate choice for a vast variety of problems or cases would be a first or second order scheme. If piecewise simple solutions (very close to linear) are sought, such as the solution of most Riemann problems with several discontinuities in between, this statement is valid [79]. However, the 2^{nd} order solutions for this case, such as the ones in FLUENT, did not manage to offer a very analytical solution of the problem or in any case, convergence.
- In almost all of the Ahmed body cases simulated with the Spalart – Allmaras turbulence model, poor convergence of the residual turbulence was shown. This presented a tendency to be more intense near reattachment. This implies that the solutions were not converged by responsibility of the unsuitable turbulence model used, instead of the order of the numerical method.
- Situations such as the Ahmed body, with a rich structure and discontinuities in the smooth part of the solution, are preferably simulated with higher – order schemes, as with schemes of lower order the structure of the solution might be very complicated, something which, along with a long time evolution might make these schemes impractical in the quest of an acceptable solution [79].
- Using a higher – order scheme (for example during the convection of a vortex for a long time), is a much more economical way in terms of cpu time to obtain the same level of resolution in some cases [79]. This is valid, for the operation count, as well.
- + when solving with lower – order schemes [81] but require finer treatment with higher – order ones.
- In comparison with the finite difference WENO schemes, finite volume WENO schemes in 2D are 4 times more expensive in terms of computational power. This value rises to 9 times more expensive in the 3D cases.
- Lower – order schemes are widely used in industry for various applications. However, they are considered to be insufficient for

viscosity dominant flows (vortical flows and boundary layer flows, such as the ones exhibited in the Ahmed body), as well as for turbulence and aeroacoustics [81]. This is apparent among others, from the highly oscillatory behavior in the simulations using lower – order schemes, such as the ones in FLUENT.

IV.) In connection with the Ahmed body case:

- For the currently available computational procedures, three dimensional bodies and the flow separations exhibited in these, pose a great challenge.
- The points of interest in the Ahmed body in terms of flow separation, mostly lie in the slant angle, the vertice of the rear window, the wake region, the roof and the sides of the body.
- The large height to length ratio leading to bluntness in bluff bodies resembling automobile shapes cannot be avoided, as there is a need in commercial vehicles for a roomy inside cavity. The great separation resulting from that fact in the wake region, is immensely affecting the drag of the bluff body.
- The main flow phenomena and flow separations and vortices (both contra – rotational and streamwise) exhibited [4], [52] in the Ahmed body are a c – pillar separating shear layer exhibited on both sides at the tip of the slant angles, rolling and forming two longitudinal vortices, a separation (and reattachment in the 25^{o} slant angle case) in the slant angle surface, which forms a separation bubble and a large flow separation in the vertical base, which forms two recirculation bubbles from two contra – rotational longitudinal vortices.
- A successfully applied turbulence model will depict the aforementioned flow separations, along with the vortex shedding and the contra – rotational vortices in the wake, which are the main points of interest here, features which become especially rigorous in the wake region owing this mostly to the geometry of the body.
- The unsteadiness in the flow separation, which derives from the unsteadiness of motion in the wake, cause for a failure to capture the ongoing phenomena using RANS simulations.
- A credible approach towards resolving the separation process cannot be offered by the linear eddy – viscosity models, mostly due to obtaining very low levels of turbulence in the separated shear layer [90] so that the flow after being separated does not reattach.

- The unrealistic values of the pressure field on the slant and the weakness of the side vortices due to defective turbulence production consequently cause poor lift values [90].
- According to [5], [2], [90], the flow in the 35^{o} slant angle is fully detached, with a relatively modest modeling challenge.
- At the 25^{o} slant angle, a separation from the roof window corner and reattachment characterizes a time mean behavior.
- As a result of the former and since the flow is separated without being reattached in the 30^{o} slant angle case, the critical angle which defines the point at which the flow is separated and the point at which the flow gets reattached, is for some angle near 25^{o}.
- Drag and lift are mostly affected by the way the flow behaves in the slant surface in the rear and the flow features downstream the body affect these values directly.
- The three features of interest in the wake region of the Ahmed body, experimentally [2] have been proved to be:
  a.) Two large tip vortices, streamwise – oriented, separating from the two upper corners of the slant angle
  b.) A separation which reattaches (in the 25^{o} slant angle case) between the roof and the slant and
  c.) The contra – rotational vortices affecting the drag and the lift of the body in the wake region.
- The shear separated layer between the roof and the slant angle is inextricably connected with the tip vortices [90]. Due to its ability of capturing adverse pressure gradients, the Spalart – Allmaras turbulence model is able to exhibit the flow detachment in the 35^{o} slant angle case and the reattachment in the 25^{o} slant angle case, but the values obtained with this configuration, are unrealistic.

5.7 Future Work

The unsteadiness of the problem itself with the rigorous vortex shedding exhibited in the slant angle, in conjunction with the highly oscillatory behavior of the residuals and a turbulence model not appropriate for flows of this type, make convergence impossible for a steady state approach and produce unrealistic results, as well. The results might have been improved, if some transient simulation (URANS or LES) cases took place for the aforementioned grids in order to try and achieve the most possible realistic approach of the flow around the Ahmed body by trying to resolve the turbulence scales instead of simply modeling them and obtaining a time – averaged solution. However, this is a work demanding excessive computational budget and something of the sort was not possible with both the time and the computational resources available throughout this study.

Of excessive interest are the flow separations created in the upper and side parts of the Ahmed body revealed from the UCNS3D simulations, which require further investigation with perhaps a more suitable turbulence model for the problem, which could resolve this kind of flow separation and properly capture and solve the shear stresses exhibited, such as a k – ω SST or a k – ε realizable. These turbulence models combined with a higher 5^{th} order WENO scheme, could produce some interesting results. An interesting approach for the separation bubble in the wake region would be the use of vortex generators in the junction between the roof of the body and the slant angle window, allowing for further observation on how such an approach would affect the flow separation downstream the Ahmed body for different slant angles, such as the ones examined in this study.

5.8 Gantt Chart for MSc by Research

5.9 References

[1] Thacker A., Aubrun S., Leroy A., Devinant P. “Effects of suppressing the 3D separation on the rear slant on the flow structures around an Ahmed body”, J. Wind Eng. Ind. Aerodyn. 107 – 108 (2012) 237 – 243

[2] Ahmed S.R., Ramm G. “Some Salient Features of the Time – Averaged Ground Vehicle Wake”, SAE Technical Paper 840300, 1984

[3] Ahmed S.R. “An Experimental Study of the Wake Structures of Typical Automobile Shapes”, J. Wind Eng. Ind. Aerodyn. 9 (1981) 49 – 62

[4] Aider J. – L., Francois – Beaudoin J., Wesfreid J. E. “Drag and Lift Reduction of a 3D Bluff Body Using Active Vortex Generators”, Exp. Fluids (2010), 48:771 – 789, DOI 10.1007/s00348 – 009 – 0770 – y

[5] Lienhart H., Stoots C., Becker S., “Flow and Turbulence Structures in the Wake of a Simplified Car Model (Ahmed Model), Lehrstuhl fur Stromungsmechanik (LSTM), Universitat Erlangen – Nurnberg

[6] Thacker A., Aubrun S., Leroy A., Devinant P. “Effects of suppressing the 3D separation on the rear slant on the flow structures around an Ahmed body”, J. Wind Eng. Ind. Aerodyn. 107 – 108 (2012) 237 – 243

[7] Leclerc C., 2008. “Reduction de trainee d’un vehicule automobile simplifie a l’aide du controle actif par jet synthetique”. These de Doctorat. Institut de Mecanique des Fluides de Toulouse

[8] Thacker A., Aubrun S., Leroy A., Devinant P. “Effects of suppressing the 3D separation on the rear slant on the flow structures around an Ahmed body”, J. Wind Eng. Ind. Aerodyn. 107 – 108 (2012) 237 – 243

[9] Joslin R.D. (1998) Aircraft laminar flow control. Annu Rev Fluid Mech 30:1 – 29

[10] Hucho W.H. (1998) Aerodynamics of road vehicles, Cambridge University Press, Cambridge

[11] Franck G., D’Elia J., “CFD modeling of the flow around the Ahmed vehicle model”,

[12] Leclerc C., Levalois E., Gillieron P., Kourta A. (2006) Aerodynamic drag reduction by synthetic jet: 2D numerical study around simplified car. In 3rd AIAA flow control conference, 5 – 8 June 2006, San Francisco, CA, USA. AIAA Paper 2006 – 3337

[13] Chun S., Lee I., Sung H. J. (1999) Effect of spanwise – varying local forcing on turbulent separated flows over a backward – facing step. Exp. Fluids 26:437 – 440

[14] Aider J. L., Beaudoin, J. F. (2008) Drag and lift reduction of a 3d bluff body using flaps. Exp. Fluids 44(4):491 – 501

[15] Verzicco R., Fatica M., Iaccarin G., Moin P., Khalighi B. (2002) Large Eddy simulation of a road vehicle with drag reduction devices, AIAA J 40(12):2447 – 2455

[16] Duriez T., Aider J. – L., Westfreid J. E. (2006) Base flow modification by streamwise vortices. Application to the control of separated flows. In Control of Separated Floes, ASME technical paper, FEDSM2006 – 98541, Miami, USA

[17] Song S., Eaton J. K. (2002) The effects of wall roughness on the separated flow over a smoothly contoured ramp. Exp Fluids 33:38 – 46

[18] Roumeas M., Gillieron P., Kourta A. (2009) Analysis and control of the near – wake flow over a square – back geometry. Comput. Fluids 38(1):60 – 70

[19] Strykowski P. J., Sreenivasan K. R. (1990) On the formation and suppression of vortex shedding at low Reynolds number. J Fluid Mech 218:71-107

[20] Dalton C., Xu Y., Owen J. C. (2001) The suppression of lift on a circular cylinder due to vortex shedding at moderate Reynolds numbers. J Fluids Struc 15:617 – 628

[21] Giannetti F., Luchini P. (2007) Structural sensitivity of the first instability of the cylinder wake J. Fluid Mech 581:167 – 197

[22] Ahmed S.R. "An Experimental Study of the Wake Structures of Typical Automobile Shapes", J. Wind Eng. Ind. Aerodyn. 9 (1981) 49 – 62

[23] Thacker A., Aubrun S., Leroy A., Devinant P. "Effects of suppressing the 3D separation on the rear slant on the flow structures around an Ahmed body", J. Wind Eng. Ind. Aerodyn. 107 – 108 (2012) 237 – 243

[24] Tsuei J. L., Savas O., Hedrick J. K. "Transient Platoon Aerodynamics During Passing Maneuvers and In – line Oscillations", California PATH Research Report, UCB – ITS – PRR – 2000 – 26

[25] H. Schlichting, et al. "Boundary Layer Theory", ISBN: 3 – 540 – 67939 – I, Reprint – 2003

[26] Hucho W. H. (1998) Aerodynamics of road vehicles, Cambridge University Press, Cambridge

[27] Roshko A., Koenig K., 1978. Interaction effects on the drag of bluff bodies in tandem. In: Aerodynamic Drag Mechanisms of Bluff Bodies and Road Vehicles, Proceedings of a Symposium held at the General Motors Research Laboratories, Warren, MI, September 27 – 28, 1976, Plenum Press, 1978, ISBN 0 – 306 – 31119 – 4

[28] Watkins S., Saunders J. W., Kumar H. B. 1992, Aerodynamic drag reduction on goods trains. J. Wind Eng. Ind. Aerodyn. 40, 147 – 178

[29] Amirnordin S. H., Wan Salim W. S. – I., Ariffin M. F., Seri S. M., Akmal N. M., Taib H. A., Alimin A. J. "Numerical Analysis on the Effects of Air Flow in the Wake of a Large Vehicle on Trailing a Passenger Car", Proceedings of MUCET 2010, Malaysian Technical Universities Conference on Engineering and Technology, June 28 – 29, 2010, Melaka, Malaysia

[30] Browand F., Hammache M., 2004. "The limits of drag behavior for two bluff bodies in tandem". SAE 2004 – 01 – 1145, also SP – 1874, published by SAE Int. ISBN 0 – 7680 – 1410 – 7

[31] Le Good G.M., Garry K.P., 2004. “On the use of reference models in automotive aerodynamics”. SAE 2004 – 1 – 1308 also SP – 1874, published by SAE International, ISBN 0 – 7680 – 1410 – 7

[32] Watkins S., Vino G. “The effect of vehicle spacing on the aerodynamics of a representative car shape”, Journal of Wind Engineering and Industrial Aerodynamics 96 (2008) 1232 – 1239

[33] Uruba V. “Lateral Vortex dynamics behind Ahmed body”, PAMM – Proc Appl. Math. Mech. 10, 455 – 456 (2010) / DOI 10.1002 / pamm.201010220

[34] Yunlong L., Moser A. “Numerical modeling of airflow over the Ahmed body”, Proceedings of CFD2003, Canada, V2, P 507 – 512, 2003

[35] Hinterberger C., Garcia – Villalba M., Rodi W. “Large Eddy simulation of flow around the Ahmed body”, in "Lecture Notes in Applied and Computational Mechanics / The Aerodynamics of Heavy Vehicles: Trucks, Buses, and Trains", R. McCallen, F. Browand, J. Ross (Eds.), Springer Verlag, ISBN: 3-540-22088-7, 2004

[36] Spohn A., Gillieron P. “Flow Separations Generated by a Simplified Geometry of an Automotive Vehicle”, IUTAM Symposium Unsteady Separated Flows (2002)

[37] Gillieron P., Chometon F. “Modeling of stationary – three dimensional detached airflows around an Ahmed Reference Body”, Third International Workshop on Vortex, ESAIM, Proceedings, Vol. 7, 1999, pp 173 – 182

[38] Motin A., Ali M.A.T. ”An experimental investigation of the effect of vehicle spacing on boundary layer characteristics in the 2 – vehicles platoon”, Proceedings of the International Conference on Mechanical Engineering 2009 (ICME 2009), ICME09 – FM – 25, 26 – 28 December 2009, Dhaka, Bangladesh

[39] White F.M. (1991), Viscous fluid flow, 2nd ed, McGraw – Hill, New York

[40] Peretmere R. CFD Analysis of a Race Car: The Reynard Inverter, MSc Thesis, Cranfield University, September 2009

[41] Hammas M., Johannson J., Skarnell H. (2010), “Large Eddy Simulation of the flow around an Ahmed body with active flow control”, Chalmers University of Techology, Department of Applied Mechanics, Division of Fluid Dynamics, Bachelor Thesis TMEX02 – 10 – 23

[42] Lorenz E. N. (1963), “Deterministic nonperiodic flow”, Journal of the Atmospheric Sciences, vol. 20, no.2, pp. 130 – 141

[43] Ferziger J. H. and Peric M. (2002), “Computational Methods for Fluid Dynamics”, Springer, vol. 3, pp. 196 – 200

[44] Anderson J. D. (1995), Computational Fluid Dynamics – The basics with applications, McGraw – Hill, New York

[45] Versteeg H. K. and Malalasekera W. (1995), An introduction to computational fluid dynamics: the finite volume method, Longman Scientific and Technical, New York

[46] Chauhan R. B., Raj K., R. Thundill “Numerical Investigation of the external flow around the Ahmed reference body using Computational Fluid Dynamics”, Research Journal of Recent Sciences, Vol. 1 (9), 1 – 5, September (2012), ISSN 2277 – 2502

[47] Sagar K., Subrata R, Vallero M., Wurtzler K., Forsythe J. (2001), “Detached Eddy Simulation over a reference Ahmed Car Model”

[48] Tsoutsanis P., Titarev V. A., Drikakis D. “WENO schemes on arbitrary mixed – element unstructured meshes in three space dimensions”, Journal of Computational Physics (2010), doi: 10.1016/j.jcp.2010.11.023

[49] Ferreira V. G., De Queiroz R. A. B., Lima G. A. B., Cuence R. G., Oishi C. M., Azevedo J., McKee S. “A bounded upwinding scheme for computing comvection – dominated transport problems”, Computers & Fluids (2012), 208 – 224

[50] Smith R. M., Hutton A. G. “The numerical treatment of advection: A performance comparison of currents methods”, Numer. Heat Transfer 1982;5:439 – 61

[51] Minguez M., Pasquetti R., Serre E. “High – Order large – eddy simulation of flow over the “Ahmed body” car model”, Physics of fluids 20, 095101 (2008)

[52] Vino G., Watkins S., Mousley P., Watrouff J., Prassad S. (2005) “Flow structures in the near – wake of the Ahmed model”, J. Fluids Struc. 20(5): 673 – 695

[53] Ichinose K., Ito S. “Accuracy of drag prediction on bluff bodies using CFD”, Technical Notes / JSAE Review 19 (1998) 151 – 160

[54] Bordei S., Popescu F. “Aerodynamic results for a notchback race car”, The Anals of “Dunarea de Jos” University of Galati, Fascicle V, Technologies in Machine Building, ISSN 1221 – 4566, (2011)

[55] Blazek J. “Computational Fluid Dynamics : Principles and applications”, ELSEVIER, 2001, ISBN : 008 043009 0

[56] Bruner, C. W. S. “Geometric Properties of Arbitrary Polyhedra in Terms of Face Geometry”. AIAA Journal, 33 (1995), p. 1350.

[57] Pulliam, T. H., Steger J. L. “Recent Improvements in Efficiency, Accuracy and Convergence for Implicit Approximate Factorization Algorithms”, AIAA Paper 85 – 0360, 1985.

[58] Thomas P.D., Lombard C.K. “Geometric Conservation Law and Its Application to Flow Computations on Moving Grids”. AIAA Journal, 17 (1979), PP. 1030 – 1037

[59] Lesoinne M., Farhat C. “Geometric Conservation Laws for Flow Problems with Moving Boundaries and Deformable Meshes and their Impact on Aeroelastic Computations”. AIAA Paper 95 – 1709, 1995; also in Comp. Meth. Appl. Mech. Eng., 134 (1996), pp. 71 – 90

[60] Guillard H., Farhat C. “On the Significance of the GCL for Flow Computations on Moving Meshes”, AIAA Paper 99 – 0793, 1999

[61] Liepmann H. G. W., Roshko A. “Elements of Gas Dynamics”. John Wiley & Sons, New York, 1957

[62] Mohanraj R., Neumeier Y., Zinn B. T. “Characteristic – Based Treatment of Source Terms in Euler Equations for Roe Scheme”, AIAA Journal, 37 (1999), pp. 417 – 424

[63] Frink N. T., Parikh P., Pirzadeh S. “A Fast Upwind Solver for the Euler Equations on Three – Dimensional Unstructured Meshes”, AIAA Journal, 24 (1986), pp. 611 – 618

[64] Strang W. Z., Tomaro R. F., Grismer M. J. “The Defining Methods of Cobalt: A Parallel, Implicit, Unstructured Euler / Navier – Stokes Flow Solver” AIAA Paper 99 – 0786, 1999

[65] Frink N. T. “Recent Progress Toward a Three – Dimensional Navier – Stokes Solver”, AIAA Paper 94 – 0061, 1994

[66] Mavriplis D. J., Jameson A., Martinelli L. “Multigrid solution of the Navier – Stokes Equations on Triangular Meshes” ICASE Report, No 89 – 11, 1989

[67] Mavriplis D. J. “Multigrid Solutions of the Two – Dimension Euler Equations on Unstructured Triangular Meshes” AIAA Journal, 26 (1988), pp. 824 – 831

[68] Barth T. J., Jaspersen D. C. “The design and Application of Upwind Schemes on Unstructured Meshes” AIAA Paper 89 – 0366, 1989

[69] Hwang C. J., Wu S. J. “Adaptive Finite Volume Upwind Approach on Mixed Quadrilateral – Triangular Meshes” AIAA Journal, 31 (1993), pp. 61 – 67

[70] Kano S., Nakahashi K. “Navier – Stokes Computations of HSCT Off – Design Aerodynamics Using Unstructured Hybrid Meshes” AIAA Paper 98 – 0232, 1998

[71] Blazek J., Irmisch S., Haselbacher A. “Unstructured Mixed – Grid Navier – Stokes Solver for Turbomachinery Applications” AIAA Paper 99 – 0664, 1999

[72] Uruba V., Hladik O. “On the Ahmed Body Wake” Colloquium FLUID DYNAMICS 2009, Institute of Thermomechanics AS CR, v.v.i., Prague, October 21 – 23, 2009

[73] ANSYS FLUENT, version 14, Theory Guide, Chapter 4.2.1, “Overview of the Spalart – Allmaras turbulence model”

[74] Titarev V. A., Tsoutsanis P., Drikakis D. “WENO schemes for mixed-element unstructured meshes” Communications in Computational Physics 8 (3) (2010) 585–609

[75] Tsoutsanis P., Titarev V. A., Drikakis D. “WENO schemes on arbitrary mixed-element unstructured meshes in three space dimensions” Journal of Computational Physics 230 (4) (2011) 1585–1601

[76] Tsoutsanis P., Antoniadis A., Drikakis D. “WENO Schemes on Arbitrary Unstructured Meshes for Laminar, Transitional and Turbulent Flows” Journal of Computational Physicsdoi:10.1016/j.jcp.2013.09.002

[77] Antoniadis A., Tsoutsanis P., Drikakis D. “High-order schemes on mixed-element unstructured grids for aerodynamic flows” AIAA 2012 Conference New Orleans 2012

[78] Toro E. “Riemann Solvers and Numerical Methods for Fluid Dynamics: A Practical Introduction” Springer, 3rd ed. 2009

[79] Cheng J., Shu W. – C. “High order schemes for CFD: A Review”

[80] Shi J., Zhang Y. – T., Shu W. – C. “Resolution of High Order WENO Schemes for Complicated Flow Structures”

[81] Deng X., Meiliang M., Tu G., Zhang H., Zhang Y. “High – Order and High – Accurate CFD Methods and Their Applications for Complex Grid Problems” Commun. Comput. Phys. doi: 10.4208/cicp. 100510.150511s, Vol. 11, No. 4, pp/ 1081 – 1102, April 2012

[82] Catalano P., Amato M. “An evaluation of RANS turbulence modelling for aerodynamic applications” Aerospace Science and Technology 7 (2003) 493 – 509

[83] Deck S., Duveau P., D’ Espiney P., Guillen P., “Development and application of Spalart – Allmaras one equation turbulence model to three – dimensional supersonic complex configurations” Aerospace Science and Technology 6 (2002), 171 – 183

[84] Lorin E., Ben Haj Ali A., Soulaimani A. “A positivity preserving finite element – finite volume solver for the Spalart – Allmaras turbulence model” Comput. Methods Appl. Mech. Engrg. 196 (2007) 2097 – 2116

[85] Bardina J. E., Hwang P. G., Coackley T. J. “Turbulence modelling validation”, NASA Ames Research Center, Moffett Field, California

[86] Rumsey C., Spalart P. “Turbulence Model Behavior in Low Reynolds Number Regions of Aerodybamic Flowfields” 36th AIAA Fluid Dynamics Conference and Exhibit, June 23 – 26, 2008, Seattle, WA

[87] Spalart P. “Strategies for turbulence modelling and simulations” International Journal of Heat and Fluid Flow 21 (2000) 252 – 263

[88] Nicoud F. “Conservative High – Order Finite – Difference Schemes for Low – Mach Number Flows” Journal of Computational Physics 158, 71 – 97 (2000), doi: 10.1006/jcph.1999.6408

[89] Soulaimani A., Ben Haj Ali A. “An unstructured finite elements method for solving the compressible RANS equations and the Spalart – Allmaras turbulence model” Computer Methods in Applied Mechanics and Engineering 199 (2010) 2261 – 2272

[90] Jang Y. – J. “An investigation of higher – order closures in the computation of the flow around a generic car” Journal of Mechanical Science and Technology 22 (2008)1019 – 1029

[91] Sau A., Hwang R. “Hopf bifurcations in bluff body wakes” Department of Mechanical and Aerospace Engineering, Gyeongsang National University, Gyeongnam 660 – 701, Republic of Korea

[92] Cooper K. R. “Bluff – Body Aerodynamics as Applied to Vehicles” Journal of Wind Engineering and Industrial Aerodynamics, 49 (1993) 1 – 22

[93] Cooper K. R. “The Wind – Tunnel Simulation of Surface Vehicles” Journal of Wind Engineering and Industrial Aerodynamics, 17 (1984) 167 – 198, Elsevier Science Publishers B. V., Amsterdam